2012

MULTIWALL CARBON NANOTUBE ARRAYS FOR THERMAL INTERFACE ENHANCEMENT

Darrell Keith Etheredge
University of Kentucky, Keith.Etheredge@uky.edu

STUDENT AGREEMENT:

I represent that my thesis or dissertation and abstract are my original work. Proper attribution has been given to all outside sources. I understand that I am solely responsible for obtaining any needed copyright permissions. I have obtained and attached hereto needed written permission statements(s) from the owner(s) of each third-party copyrighted matter to be included in my work, allowing electronic distribution (if such use is not permitted by the fair use doctrine).

I hereby grant to The University of Kentucky and its agents the non-exclusive license to archive and make accessible my work in whole or in part in all forms of media, now or hereafter known. I agree that the document mentioned above may be made available immediately for worldwide access unless a preapproved embargo applies.

I retain all other ownership rights to the copyright of my work. I also retain the right to use in future works (such as articles or books) all or part of my work. I understand that I am free to register the copyright to my work.

REVIEW, APPROVAL AND ACCEPTANCE

The document mentioned above has been reviewed and accepted by the student's advisor, on behalf of the advisory committee, and by the Director of Graduate Studies (DGS), on behalf of the program; we verify that this is the final, approved version of the student's dissertation including all changes required by the advisory committee. The undersigned agree to abide by the statements above.

Darrell Keith Etheredge, Student

Dr. Rodney Andrews, Major Professor

Dr. James McDonough, Director of Graduate Studies

MULTIWALL CARBON NANOTUBE ARRAYS FOR THERMAL INTERFACE ENHANCEMENT

THESIS

A thesis submitted in partial fulfillment of the requirements
for the degree of Master of Science in Mechanical Engineering
in the College of Engineering at the University of Kentucky

By
Darrell Keith Etheredge

Lexington, Kentucky

Director: Dr. Rodney Andrews, Professor of Chemical and Materials Engineering

Lexington, KY

2012

ABSTRACT OF THESIS

MULTIWALL CARBON NANOTUBES FOR THERMAL AND MECHANICAL PROPERTY ENHANCEMENT

High performance/small package electronics create difficult thermal issues for integrated circuits. Challenges exist at material interfaces due to interfacial contact resistances. Multiwall carbon nanotube (MWCNT) arrays are considered to be excellent candidates for use as thermal interface materials (TIMs) due to outstanding thermal/mechanical properties. In this work, MWCNT array TIMs are analyzed in aluminum and carbon fiber composites via flash diffusivity analysis. The effect of TIM thickness, areal/bulk density, surface cleanliness, and volumetric packing fraction; along with the effect of substrate finish and interfacial contact pressure on thermal performance are analyzed. Trends show the best TIMs possess low thickness, high bulk density and packing fraction, and clean surfaces. Pressure dramatically increases thermal performance after establishing contact, with diminishing returns from additional pressure. Diffusivities approaching 40 mm^2/s and 0.65 mm^2/s are recorded for aluminum and composite systems. Oxygen plasma etching and high temperature annealing ("Graphitizing") are investigated as methods to remove amorphous carbon from array surfaces. Graphitized TIMs report diffusivity improvements up to 53.8%. Three methods of incorporating MWCNTs into composites are attempted for thermal/mechanical property enhancement. Conductance calculations show increasing diffusivity without increasing thickness enhances thermal performance in composites. MWCNTs for mechanical property enhancement produce no change, or detrimental effects.

KEYWORDS: Carbon Nanotubes, Thermal Interface Materials, Carbon Nanotube Arrays,

Thermal Contact Resistance, Composite Thermal Interface Materials

Darrell Keith Etheredge

April 18th, 2012

MULTIWALL CARBON NANOTUBES FOR THERMAL AND MECHANICAL PROPERTY ENHANCEMENT

By

Darrell Keith Etheredge

_Dr. Rodney Andrews_____
Director of Thesis

_Dr. James McDonough_____
Director of Graduate Studies

_____April 18th 2012_____

For my parents,
Darrell and Cathy Etheredge

ACKNOWLEDGEMENTS

First I would like to thank Dr. Rodney Andrews for his support and encouragement throughout my graduate career at the University of Kentucky. His guidance and example have been invaluable to my studies, research, and growth as an engineering professional. I would also like to thank Dr. Johné Parker and Dr. Ibrahim Jawahir for their contributions to my education at the University of Kentucky, and for graciously serving on my thesis committee.

Special thanks are also well deserved by my mentor at the Center for Applied Energy Research, Dr. Matthew Weisenberger. His constant guidance on researching, writing, and life in Graduate School has propelled me forward to this point in my career. Without his selfless support and the opportunities he afforded me, I would never have learned as much as I have in such short time.

There are countless individuals who deserve my thanks at the Center for Applied Energy Research. In particular, I thank my friends and colleagues from the Carbon Materials Group: John Craddock, Terry Rantell, David Jacques, Ashley Morris, Dali Qian, Mark Taylor, Sean Tobey, and Catie Lester. These individuals have all taught me so much about research, science, and teamwork. I will always treasure the time we spent together.

I would also like to graciously acknowledge the funding and technical support of the US Army Aviation and Missile Research, Development and Engineering Center (AMRDEC). Specifically, I would like to thank Bob Evans, Keith Roberts, Taylor Owens, and my predecessor, Carissa Russell. Their support of my research as a part of the Smaller, Lighter, Cheaper project has allowed me to focus on my studies and make the most of my time in Graduate School.

Additionally, special thanks are due to Rich Foedinger, Simon Chung, and the entire staff of Materials Sciences Corporation (MSC) for their gracious funding and technical support.

Finally, I wish to express my heartfelt thanks to my family. To my wife, Joy, thank you for your unending love and support of all my endeavors. To my mother and father, thank you both for sacrificing so much for my education, and for instilling the value of hard work and dedication in me. The examples you set continue to inspire me and guide my life.

TABLE OF CONTENTS

LIST OF TABLES

LIST OF FIGURES

Chapter 1 General Introduction and Outline

1.1 Motivation

As technology continues to advance, the expectations and demands consumers place on the devices they use seems to expand without limit. This mindset demands increased portability coupled with higher performance to deliver an unparalleled level of integration with daily life. Society has progressed from desktop computers and home telephones to high powered tablets, mobile broadband internet connections and smartphones. All of these advances require more power through smaller circuits, which inevitably results in greater thermal dissipation challenges. The International Technology Roadmap for Semiconductors estimates power dissipation levels for nanoscale devices will reach 100 W/cm^2 by the year 2020[1]. The only way to achieve this is for thermal management technologies to scale with the improvements in electronics. In current electronic devices, thermal interface materials (TIMs) are used between a heat source, such as a processor or other integrated circuitry and a heat sink. These materials are designed to fill voids between the surfaces and enhance the thermal transport across the interface. Current TIM materials such as metallic greases and phase change materials are nearing their performance limits, obviating the need for higher performing TIMs to meet future thermal design challenges. Highly aligned Multiwall Carbon Nanotube (MWCNT) arrays are being explored as future TIMs due to their excellent mechanical and thermal properties.

Additionally, growing trends in mechanical design point to use of composite materials such as carbon fiber reinforced polymers (CFRPs) to replace metals in structural applications. CFRPs possess high specific strength which allows for significant weight savings in material structure, as well as real world economic benefits like increased fuel efficiencies in automobiles and air/spacecraft. However, the structural benefits of carbon fiber composites come with unprecedented anisotropic thermal design challenges. Not only will MWCNT TIMs be important in future interfaces between composite materials and traditional circuit assemblies, but carbon nanotubes in general can be used to overcome some of the thermal challenges due to inherent material anisotropy in carbon fiber composites.

1.2 Introduction

In thermal management situations, especially those concerning the efficient removal of heat from a power source or electronics package, some form of heat sink is generally required. For any heat sink to be effective the system has to have good thermal contact. The term "thermal contact" describes when two macroscopic systems are able to exchange energy (i.e. heat) with one another through particle collisions or radiation[2]. Those systems with good thermal contact can transfer heat easily across an interface, while those with poor thermal contact (i.e. insulated systems) have large interfacial contact resistances, R_c, and struggle to transfer heat to the environment.

When designing for optimal thermal contact at an interface, one must imagine the space between the surfaces they want to join. Although the surfaces may appear smooth to the touch, microscopic surface roughness features will create point contacts, and drastically influence the localized heat transfer, as shown in Figure 1-1 below [3]. The call out in the figure shows what the surface features look like on the micro scale, with lines indicating conductive heat paths. These point contacts allow less than one percent of the possible contact area to actually engage, and provide the least resistive path for heat flow across the interface [4]. This leaves gaps between the other 99% of potential contact locations to be occupied by air, which is a poor conductor of heat. These asperities insulate the interface rather than conduct heat across the boundary.

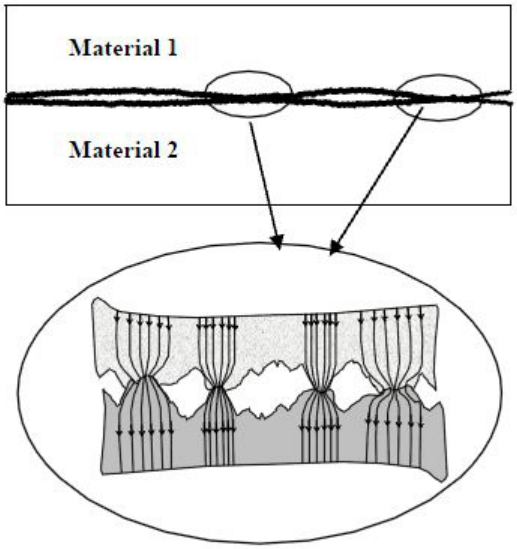

Figure 1-1 – Effect of roughness features on conductive heat transfer[1] [3]

The most common solution to problems associated with poor thermal contact is to use a thermal interface material, or TIM. At its simplest, the function of a TIM is to replace the largely non-conducting air trapped between micro asperities with a high conductivity material [5]. TIMs are made from many different materials, with the most common being thermal greases, phase change materials, filled polymer matrices and carbon based materials [3]. Table 1-1 outlining the pros and cons of common TIMs is presented below.

[1] Reprinted with permission from Electronics Systemintegration Technology Conference, 2006 1st, Farhad Sarvar, Whalley, D. C., Conway, P. P. Thermal Interface Materials – A Review of the State of the Art, Page 1292, © 2006 IEEE

Table 1-1: Summary of common TIM systems[2], adapted from [3]

TIM Type		Advantages	Disadvantages
Thermal Grease		- High thermal conductivity - Thin bond line with minimal installation pressure - No curing - Low cost - No delamination	- Thermal cycling causes pump- out, phase separation - Can be messy, especially in manufacturing - Thickness control difficult - Excess greases flow out
Phase Change Materials	Polymers	- higher stability, less pump-out - Easier to apply than greases - No curing required - Delamination not an issue - No drying out - Lower thermal resistance than greases	- Lower thermal conductivity than greases - Potentially higher surface resistance than greases - Constant pressure needed - Voids result from thermal cycling, phase changes that cannot be refilled
	Low Melting Point Alloys	- Easy to apply - All metal path – low resistance - No curing required	- Dry-out causes voids - Intermetallic growth at the interface - Oxidation/Corrosion at high temp cycling
Filled Polymers		- Not messy, easy to handle - No guessing on applied amount - Conforms to surface before cure - No pump-out - Resists harsh environments - Good dielectric properties - Low modulus material - Easily cut to size	- Curing required - Thermal conductivity lower than grease - Delamination can occur - Does not flow freely - Requires permanent clamping pressure - Higher cost than grease
Carbon Nanotube/Nanofiber based materials		- Can be used as freestanding arrays or dispersed in polymers - Accept PCM additions wicked into freestanding arrays - high thermal conductivity - Mechanically compliant	- Expensive - Difficult to handle - Properties range due to CVD growth processes.

[2] Adapted with permission from Electronics Systemintegration Technology Conference, 2006 1st, Farhad Sarvar, Whalley, D. C., Conway, P. P. Thermal Interface Materials – A Review of the State of the Art, Page 1292, © 2006 IEEE

At this point, an understanding of contact resistance is useful. Figure 1-2 will serve as reference for the following discussion.

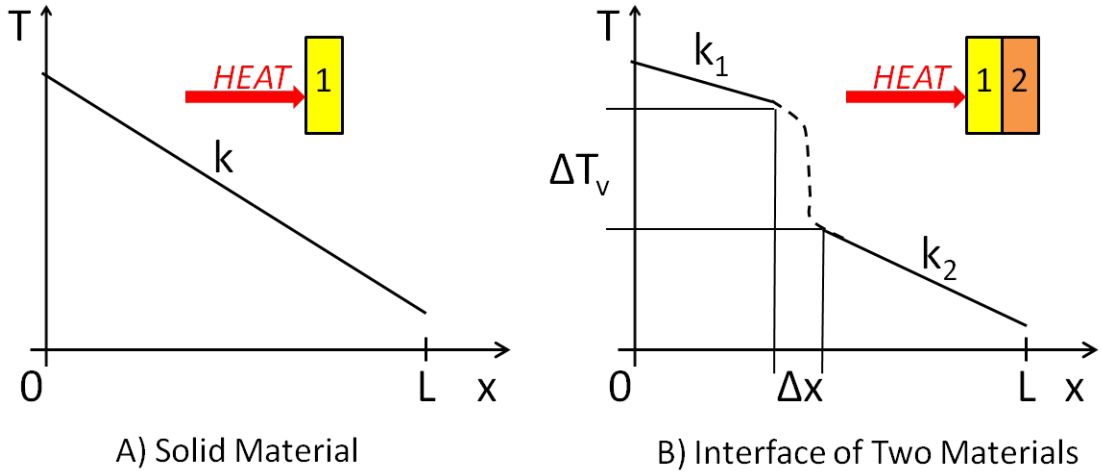

Figure 1-2 - Temperature vs. Displacement Plots, Solid and Composite Walls

Fourier's law of conduction states that the heat flux through a solid material, such as the wall depicted in Figure 1-2, part A, is defined by the ratio of change in temperature with respect to displacement, multiplied by a constant of proportionality. Mathematically, this is written in the familiar form:

$$\vec{q} = -k\frac{\Delta T}{\Delta x} \tag{1.1}$$

Where $\vec{q}$ represents the heat flux through the surface, *k* is the thermal conductivity of the material, *ΔT* corresponds to the temperature gradient in the material, and *Δx* represents the change in location between temperature measurement locations. In a solid, homogenous wall, it is possible to replace *Δx* with the total thickness of the wall, *L*, and re-arrange the equation to the following form (this will prove useful momentarily).

$$-\frac{L}{k} = \frac{\Delta T}{\vec{q}} \tag{1.2}$$

In an interfacial situation, like Figure 1-2, part B, the potential for different thermal conductivities (i.e. differing constants of proportionality) must be accounted for. Here, the idea of contact resistance is useful, and is defined by equation (1.3) below.

$$R_c = \frac{\Delta T_v}{\vec{q}} \tag{1.3}$$

In this situation, ΔT_v represents the "virtual" change in temperature seen from one side of the interface to the other (seen in the dotted line between two regions of different slope in Figure 1-2, part B). In this dotted line region, k is *not* constant. By defining the thermal contact resistance, R_c, in this way provides a substitution for the $-L/k$ term in equation (1.2), safely allowing a change in thermal conductivity across this border, without violating Fourier's conduction law for steady state situations.

The effect of interfacial contact resistance can be understood best from a first principles thermal circuit model [6, 7]. For the following discussion, a two layer thermal interface system will be modeled as resistors in series, as shown in Figure 1-3 with exaggerated TIM layer thickness.

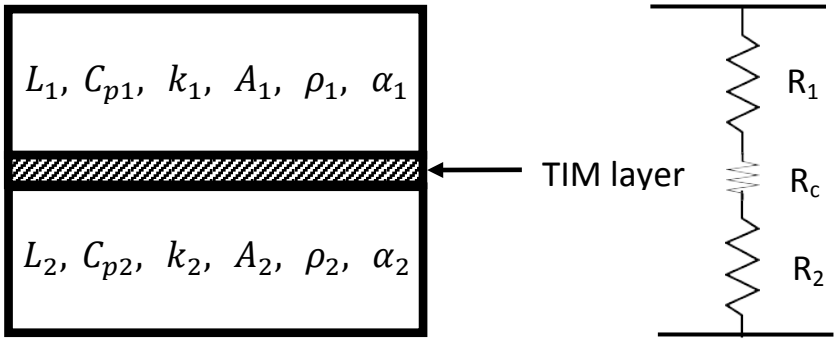

Figure 1-3 - Two layer interface system with resistive thermal circuit model

In the model, *L* represents the substrate thickness, C_p is the specific heat at constant pressure, *k* is the thermal conductivity of the substrate, *A* is the surface area at the interface, *ρ* is the mass density, and *α* is the thermal diffusivity of the substrate. The total resistance of the system can be expressed as a sum of thermal resistances (units of K/W), as in equation (1.4):

$$R_{Total} = R_2 + R_{TIM} + R_1 \tag{1.4}$$

Where thermal resistances R_2, R_{TIM}, and R_1 are defined as:

$$R_i = \frac{L_i}{k_i\, A_i} \quad (where\ i = 1,2) \tag{1.5}$$

$$R_{TIM} = \frac{R_c}{A_c} \tag{1.6}$$

In two layer thermal interface systems, additional TIM "layers" are designed to be as thin as possible. This follows from the general definition of thermal resistance, as shown for layers of non-negligible thickness in equation (1.5). However, since a TIM is designed to be as thin as possible, its thickness is negligible compared to the surrounding substrate thicknesses. This assumption makes it possible to ignore its thickness altogether, so instead its resistance is represented as an unknown contact resistance, R_c, as shown in equation (1.6).

At this point, it is critically important to understand the subtle difference between a thermal resistance and a thermal *contact* resistance, as it appears in equation (1.6). Thermal resistances are represented in units of K/W, where contact resistances are shown in units of m^2K/W. To convert a thermal *contact* resistance into a standard thermal resistance, one must normalize the contact resistance to the contact area.

Moving forward, if equation (1.4) is expanded using the definition of thermal resistance from equation (1.5), a more detailed picture of a two layer system develops, as shown in equation (1.7):

$$\frac{L_{total}}{k_{total}\, A_{total}} = \frac{L_1}{k_1\, A_1} + \frac{L_2}{k_2\, A_2} + \frac{R_c}{A_c} \tag{1.7}$$

In most electronics packaging systems, thermal interface areas are designed such that the contact area is equivalent on both sides of the interface. Thus it will be considered that all areas in equation (1.7) are equal, $A_{total} = A_1 = A_2 = A_c$. For the purposes of this study, it will also be considered that the substrate materials are identical. This allows a simplification of conductivity terms, $k_{total} = k_1 = k_2$, and thickness terms, $L_1 = L_2$ (as well as specific heat terms $C_{p,total} = C_{p1} = C_{p2}$ which will be introduced shortly). One final substitution that will be used to convert thermal conductivity, k, into more useful terms is found in equation (1.8):

$$k = \alpha C_p \rho \tag{1.8}$$

Here, thermal conductivity, k, is equivalent to the product of thermal diffusivity, α, specific heat at constant pressure, C_p, and mass density, ρ. After substituting equation (1.8) (along with the simplifications for identical substrates), the unknown contact resistance can be solved for as a function of bulk system properties and known substrate properties as shown in equation (1.9).

$$R_c = \frac{L_{total}}{\alpha_{total}\, C_{p\,total}\, \rho_{total}} - 2\left(\frac{L_1}{\alpha_1\, C_{p1}\, \rho_1}\right) \tag{1.9}$$

This expanded form of equation (1.4) allows one to solve for the contact resistance of a two layer TIM system through direct knowledge of bulk system and individual substrate thermal and physical properties. Bulk system thickness can easily be measured, and it is reasonable to assume that bulk system specific heat and density are equivalent in identical substrates. Bulk thermal diffusivity of a two layer system can be found through use of the laser flash method, which will be a major discussion point later in this thesis.

1.3 Outline

Throughout this work, several approaches to studying MWCNT arrays as either a TIM, or structural enhancement (or both) are presented. Chapter 2 presents thermal testing results of aligned MWCNT array TIMs in aluminum substrates with a focus on determining which property(or combination of properties) of the array or substrate system affects thermal performance the most. Properties of interest include array thickness, areal and bulk densities, volumetric packing fraction, and surface cleanliness. Also considered are the effects of substrate surface roughness and interfacial contact pressure.

Chapter 3 explores the thermal performance of carbon fiber composite interface systems and the potential for improvements in performance through use of aligned MWCNT array TIMs. Thermal testing considerations in the flash diffusivity method are discussed for carbon fiber composite substrates. Variables considered in Chapter 2 are revisited here, as thermal testing is conducted between two different carbon fiber composite substrate surface finishes as well as various interfacial contact pressures.

Lastly, Chapter 4 explores two potential methods of post processing for aligned MWCNT array TIMs aimed at improving the thermal performance of the materials. Radio frequency oxygen plasma etching is considered as a method of removing surface layers of amorphous carbon, as well as a potential method to optimize array thicknesses for custom interface materials. High temperature annealing, or “graphitization” of aligned MWCNT array TIMs is considered as a method of purifying arrays and repairing defects in the structure of individual carbon nanotubes. Thermal testing is performed on samples processed with both methods to determine the efficacy of these methods in improving the thermal performance of aligned MWCNT array TIMs.

1.4 Literature Review

The discovery of multiwall carbon nanotubes was first reported by Sumio Iijima in 1991 [8]. He noted the growth of "needle-like" carbon structures grown on the negative end of an electrode he was using for an arc-discharge process used to mass produce the C_{60} molecule, known as "fullerenes". Subsequent TEM images of the structures would reveal their cross section contained between 2 and 50 coaxial layers of carbon hexagons, and were between a few, to a few tens of nanometers in diameter. Examples of the MWCNTs found by Iijima can be seen in Figure 1-4 below. In the image, hollow tube structures can be seen via Transmission Electron Microscopy (TEM). Tubes a, b, and c have 5, 2, and 7 walls respectively.

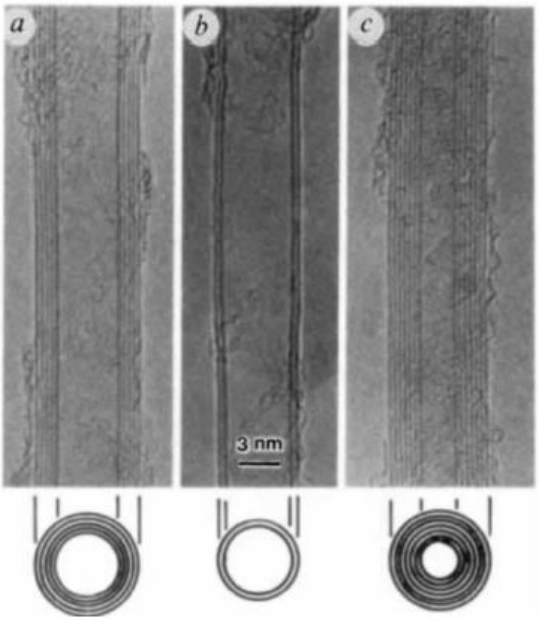

Figure 1-4 - TEM image of Iijima's MWCNTs in 1991, courtesy of Nature Publishing Group[3] [8]

Single-wall carbon nanotubes were discovered in 1993 and independently reported by both Iijima, et al. [9] and Bethune, et al. [10]. In Iijima's case, he noted that SWCNTs formed during arc-discharge processes where carbon reacted in the presence of iron, argon, and methane. Bethune discovered SWCNTs using a similar arc-discharge fullerene production process, except his process utilized cobalt. TEM from his experiment revealed carbon nanotubes with one wall

[3] Reprinted by permission from Macmillan Publishers LTD: NATURE, 354, Sumio Iijima, Helical microtubules of graphitic carbon, Page 56. Copyright 1991.

woven throughout the fullerene dense soot formed in the process. A close up view of one SWCNT from Bethune's process is given below in Figure 1-5, which details a TEM image of a single-wall carbon nanotube produced via arc-discharge process of carbon in the presence of cobalt. The small, spherical structures attached to the tube and in the bottom of the image are fullerenes (C_{60} molecules), which were the intended product of the process.

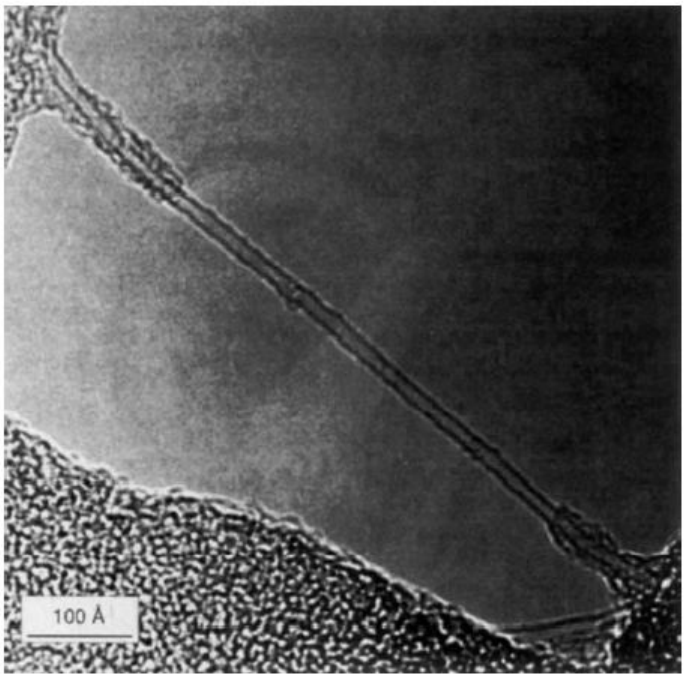

Figure 1-5 - TEM image of a SWCNT, courtesy of Nature Publishing Group[4] [10]

1.4.1 Carbon Nanotube Morphology

Carbon nanotubes are an interesting physical phenomenon for a number of reasons. One of the most important aspects of their nature is their construction. At its most basic, a carbon nanotube is a hollow structure made of sp^2 hybridized carbon atoms arranged in a hexagonal pattern [11, 12]. The excellent thermal [13], electrical [14], and mechanical [12] properties of carbon nanotubes are direct benefits of their lattice pattern and stiff sp^2 bonds . Each layer has the same structure as a single sheet of graphene that has been rolled into a cylinder (although it

[4] Reprinted with permission from Macmillan Publishers Ltd: NATURE, 363, Bethune, D. S., C. H. Klang, M. S. de Vries, G. Gorman, R. Savoy, J. Vazquez, R. Beyers, Cobalt-catalysed growth of carbon nanotubes with single-atomic-layer walls, page 606. Copyright 1993

is not possible to actually *produce* a carbon nanotube in this fashion). In a multiwall carbon nanotube, the spacing of the layers is approximately the same as the spacing of layers of turbostratic graphite [15] (approximately 3.4 angstrom [16]).

The three common classifications of carbon nanotube construction are “armchair”, “zigzag”, and “chiral” nanotubes. These designations are based on their chiral, or “roll-up” vector, $\overrightarrow{C_h}$, and the chiral angle, θ [16]. When the chiral vector is defined mathematically in equation 0 as:

$$\overrightarrow{C_h} = na_1 + ma_2 \tag{1.7}$$

Where (n,m) comprise the lattice translation index and a_1 and a_2 are the base vectors of the lattice plane. Tubes designated (n,0) are zigzags, (n,n) tubes are armchairs, and anything (n,m) where n≠m are chiral. An easy way to visualize this is to imagine bending the chiral vector (and with it, the graphene sheet) back onto itself to form a circle by connecting the vector tip to its tail. You would then have a single-wall carbon nanotube matching one of the three geometries. Figure 1-6 and Figure 1-7 below help illustrate this concept. Figure 1-6 shows dotted lines with chiral vector directions for armchair and zigzag nanotubes, while Figure 1-7 shows a model diagram of each nanotube type’s construction.

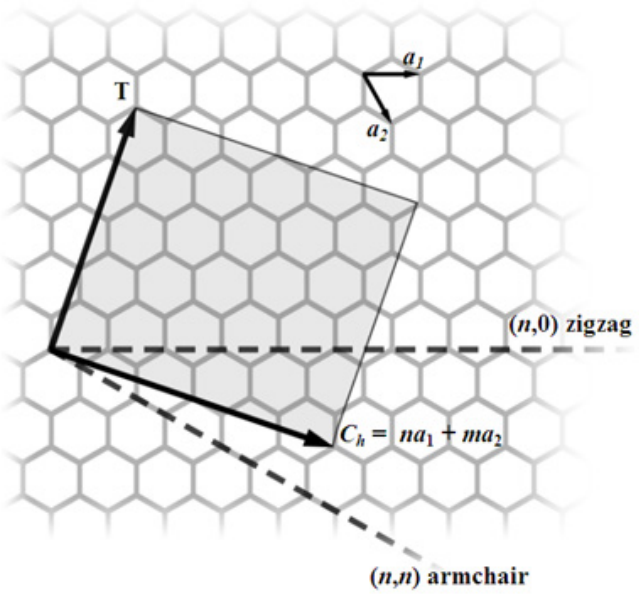

Figure 1-6 - An illustration of nanotube chiral vectors[5]

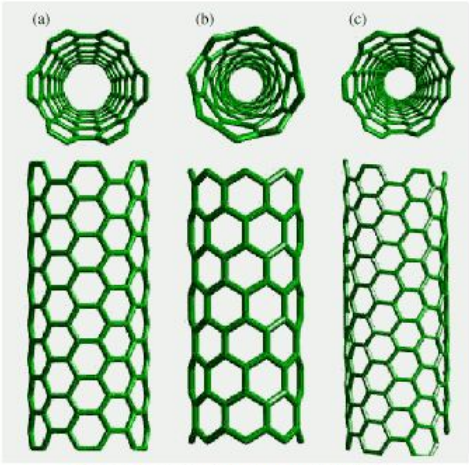

Figure 1-7 - Diagrams of nanotube constructions[6] [17]

[5] This work was released into the public domain by its author, Kebes, on the Wikimedia Commons: http://commons.wikimedia.org/wiki/File:CNTnames.png

[6] Reprinted from New Journal of Physics, 5, 126, Humberto Terrones, Mauricio Terrones, "Curved nanostructured materials" Page 126.13, Copyright 2003 IOP Publishing Ltd and Deutsche Physikalische Gesellschaft. doi:10.1088/1367-2630/5/1/126

Obviously, for single-wall carbon nanotubes, only one layer of graphene is involved. For multiwall carbon nanotubes, it has been previously discussed that tubes as large as 50 layers have been reported [8]. To illustrate these layers a bit more clearly see Figure 1-8.

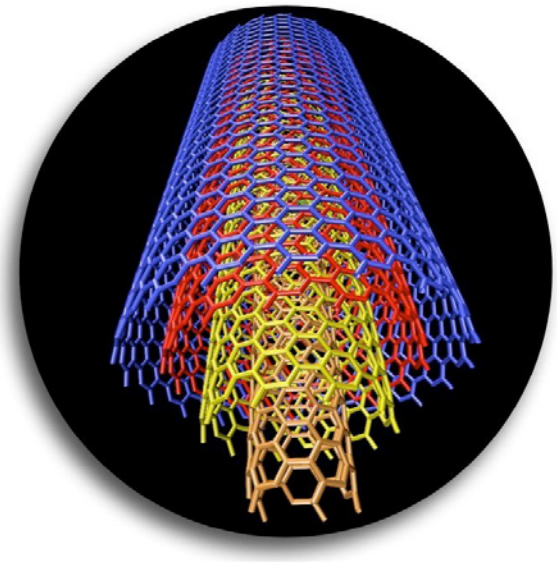

Figure 1-8 - Concentric shells of MWCNTs[7]

All the layers of the MWCNT do not align their respective lattices to each other, such that you can "see" straight through to the hollow core without interference. This is an example of turbostratic graphitic stacking, and results in a slightly larger gap between layers in MWCNTs than you would find in layers of traditional graphite. From a chemical bonding perspective, the carbon atoms comprising a single layer of any carbon nanotube are held together by strong sp^2 bonds (also known as σ-bonds). The component layers of a MWCNT are held together through weaker, out-of-plane bonds, known as π-bonds [12]. This is illustrated in Figure 1-9 below, which diagrams the basic hexagonal bonding structure for a single graphite layer. For spatial understanding, imagine the hexagon as being tilted backward into the page along its horizontal axis. The carbon atoms are the black circles at the hexagon vertices. The strong σ-bonds connect the carbon atoms to each other in the plane of the hexagon, while the weaker π-bonds keep sheets of graphene connected to the top and bottom of the hexagonal plane.

---

[7] Copyright A. Rochefort, nano@polyMTL.ca, http://nanostructures.phys.polymtl.ca/en/Home.html

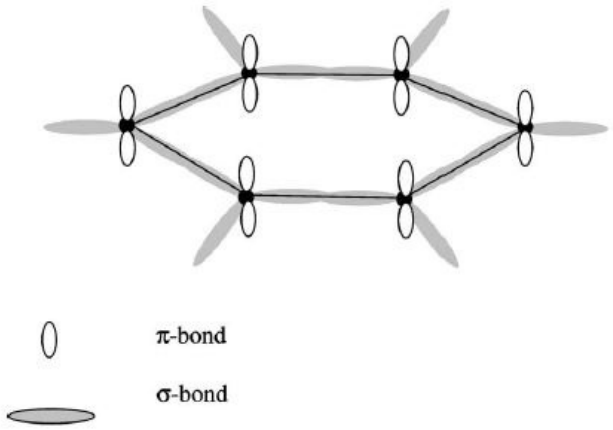

Figure 1-9 - Hexagonal bonding structure for a single graphite layer[8] [12].

When carbon nanotubes are formed, they possess perfect, hexagonal crystalline structure. In armchair nanotubes under tensile stress, a condition known as the "Stone Wales rotation", or "5-7-7-5" defect can occur [18-21]. This defect describes a reversible break in the periodic hexagonal pattern of the carbon nanotube where two carbon atoms rotate 90 degrees about their bond axis. This shift changes the local lattice structure to produce two pentagons and two heptagons, hence "5-7-7-5". This is actually a useful mechanism which increases the elasticity of a nanotube, as well as provides a release for excess strain energy in the tube when strained beyond 5% [21]. Figure 1-10 (Left) shows a Stone Wales defect in an armchair nanotube. The C-C bond in the center of the formation rotates 90° to produce two heptagons (left and right) and two pentagons (top and bottom). Figure 1-10 (Right) shows a carbon nanotube experiencing necking facilitated by Stone Wales rotation defects. The carbon nanotube has constricted as a method of releasing excess strain energy under tension.

[8] Reprinted from Comptes Rendus Physique, 4, Rodney S. Ruoff, Dong Qian, Wing Kam Liu, Mechanical properties of carbon nanotubes: theoretical predictions and experimental measurements, Page 994, Copyright 2003, with permission from Elsevier

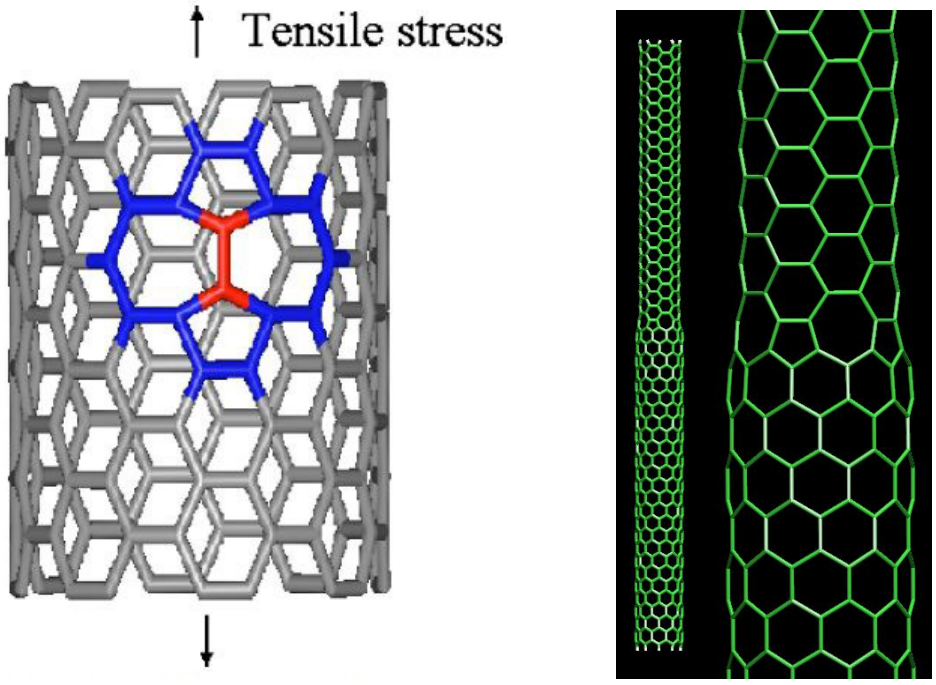

Figure 1-10 – (Left) Stone Wales rotation defect[9] [22], (Right) CNT Necking due to Stone Wales[10]

1.4.2 Phonons as Thermal Transport Mechanism

Carbon nanotubes of any variety are mechanically resilient, and are excellent conduits of heat and electricity [12, 23, 24]. The crystalline lattice structure of a carbon nanotube is responsible for its excellent thermal conductivity. The regular arrangement of stiff sp^2 hybridized bonds acts as a confining channel for energy distributing phonons[25].

A phonon can be described as a quantized sound wave, or as a collective vibrational mode of a solid or liquid [26]. These modes naturally exist in structures, and have been divided into two categories based on their behaviors, known as coherent and incoherent phonons. Incoherent phonons correspond to the random oscillations of atoms within a system. When left undisturbed, the atoms oscillate in random phase with respect to each other. When an impulse is applied to the system, each atom moves in phase with its neighbor, exhibiting a coherent

[9] Reprinted figure with permission from Wei, Chenyu; Kyeongjae Cho, Deepak Srivastava, PHYSICAL REVIEW B, 67, 115407, page 1, 2003, Copyright 2003 by the American Physical Society

[10] Copyright A. Rochefort, nano@polyMTL.ca, http://nanostructures.phys.polymtl.ca/en/Home.html

phonon. In an engineering sense, coherent phonons can be thought of as similar to a transverse wave, where all atoms transmit energy to their neighbors in the same direction.

Phonons are responsible for transporting thermal energy in nonmetallic systems, with the bulk of the heat being carried by phonons possessing a mean free path (λ_{mfp}) of 1 – 100 nm [27]. The mean free path is defined as the average distance travelled by a phonon (or an electron in the case of metallic conductors) before it collides with either an imperfection in the material or with another phonon. In all cases, a higher phonon mean free path equates to higher thermal conductivity [28]. Phonons move through materials at the average speed of sound through the medium, and are related to the thermal conductivity through equation (1.8):

$$k = \frac{1}{3} C\ \bar{c}\ \lambda_{mfp} \tag{1.8}$$

where *C* represents the phonon specific heat, $\bar{c}$, represents the average speed of sound through the medium, and λ_{mfp} is the mean free path of the phonon [28].

The idea that phonons can be thought of as vibrational modes and quantized sound waves can be extended to conductive transmission of energy at an interface. From a crystallographic point of view, Cahill, et al. writes that an "interface" can be thought of as an interruption in a regular crystalline lattice, which phonons propagate through [27]. At an interface of two different materials, like a TIM and its substrates, an acoustic impedance mismatch occurs due to the different densities and speeds of sound in the interface materials. This mismatch results in a transmission loss due to phonon scattering at the boundary. In the case of a TIM system, boundary scattering results in decreased thermal conductivity or increased thermal resistance at the interface and a general decrease in TIM efficiency.

1.4.3 Thermal Properties of MWCNT Arrays and Attempted Modifications

Modern carbon nanotubes are grown by several methods, including arc-discharge, chemical vapor deposition, and laser ablation of graphite targets [12]. What makes these nanotube arrays attractive as a viable TIM is their outstanding thermal, mechanical and electrical properties [12, 20, 23]. Their natural tendency to grow in vertically aligned "arrays" allows for immediate harnessing of their full potential [6]. An SEM image detailing the aligned natural growth patterns of MWCNTs used in the experimental section of this thesis is presented below in Figure 1-11.

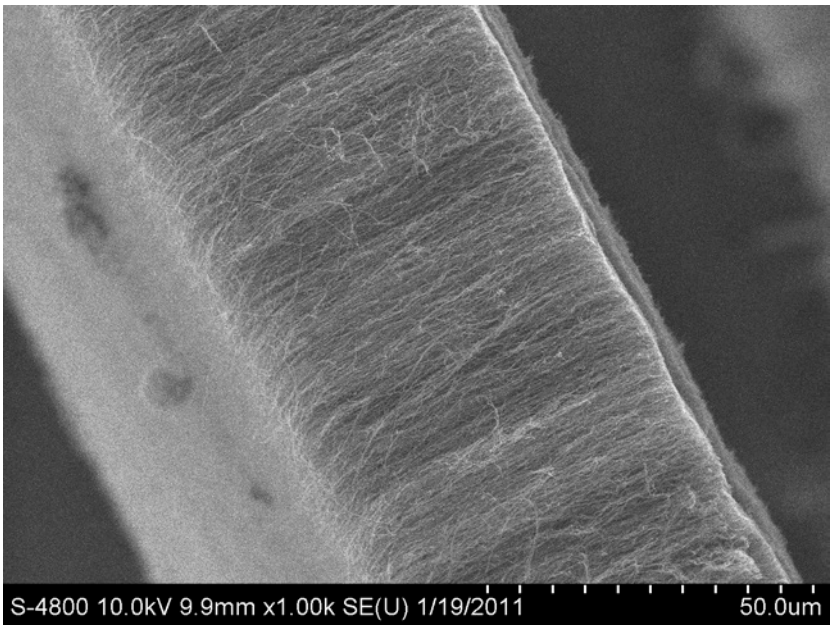

Figure 1-11 - SEM image of highly aligned MWCNT array

The thermal conductivity of individual MWCNTs has been measured as >3000 W/mK [29]. Others have conducted molecular dynamics (MD) simulations and experiments on individual SWCNTs, reporting values ranging from 6600 W/mK at room temperature to 37,000 W/mK at 100 K (-173 °C) [13]. However, the majority of published experiments focus on a more realistic, bulk property approach. Reported thermal conductivity values for bulk MWCNT arrays indicate some disagreement over the true potential of these systems. Shaikh et al. reported 8.3 W/mK from a laser flash diffusivity method [6], Ivanov et al. reported 15.3 ± 1.8 W/mK from a xenon flash diffusivity method [30], while Yi et al. reported 20 W/mK for "bulk" mat MWCNTs from a 3ω-method [31].

There have also been published reports of MWCNTs as the foundation of experimental TIM assemblies with measurable success. One such device was constructed from graphite, epoxy infused MWCNTs, gold and palladium CNT tip coatings and indium metal by Sihn, et al. They reported that the conductivity of their prototype interface device jumped from 0.79 W/mK to 250.4 W/mK when MWCNTs were included (although they admit this value is not attainable when using composite materials like carbon fiber for substrates) [32]. Another customized interface was reported by Ganguli, et al. using gold, indium, and RF oxygen plasma etching to optimize CNT array-substrate contact. They reported system improvement from 1 W/mK conductivity to 262 W/mK upon inclusion and optimization of an aligned MWCNT array [33].

There have been some attempts to explain the disparity in reported conductivity values for carbon nanotubes. Kim, et al. have suggested that differences between mesoscopic and bulk scale measurements are due to nanotube interactions leading to high resistance thermal junctions between the tubes [29]. Yi, et al. attribute disparities in measurement values to high defect densities in synthesized nanotube arrays [31]. This is corroborated by Ruoff, et al. and Chang, et al. Ruoff states that the distribution and type of defects in a carbon nanotube affect tube mechanics, including potentially its electrical and thermal transport properties [12], while Chang notes that damage done to layers of a multiwall carbon nanotube will dramatically decrease thermal conductivity through the tube [25].

1.4.4 Mechanical Properties of MWCNT Arrays

Multiwall carbon nanotubes are incredibly strong materials. The measured specific tensile strength of one layer of a MWCNT can be as high as 100 times that of steel [12]. As previously noted, MWCNT arrays are composed of countless numbers of individual MWCNTs. These arrays are bound together by weak van der Waals forces and tube entanglements. Each tube possesses an extraordinarily large aspect ratio due to their nanometer scale diameters and micrometer scale lengths. However, this high aspect ratio also means that carbon nanotubes are susceptible to structural instabilities [12], such as buckling or kinking under axial compression [24].

The stiff, covalent bonds which compose the nanotubes' graphene-like structure, provide a framework capable of withstanding extreme stresses. Several groups have conducted studies on stress-strain relations of multiwall carbon nanotubes. Treacy, et al. was among the first to measure the Young's modulus of individual MWCNTs. They measured thermally induced vibrational modes in a TEM assuming that nanotubes vibrate like a homogeneous, hollow cylindrical cantilever. They tested eleven tubes of random length, and random inner/outer diameters, reporting values ranging from 0.4 to 4.15 TPa (overall average modulus of 1.8 TPa) [34]. An example of these types of vibrational measurements can be seen in Figure 1-12.

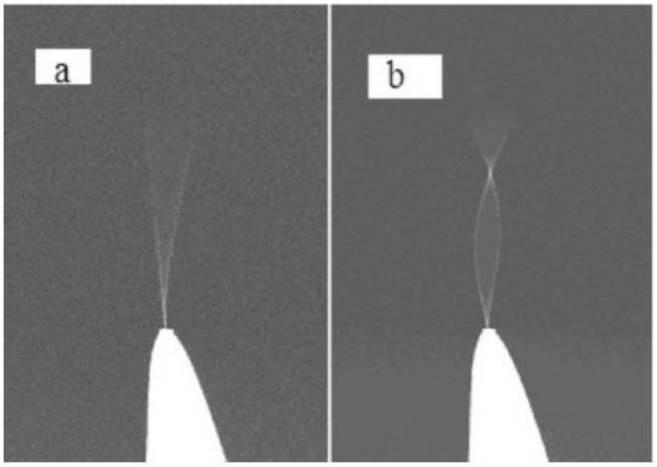

Figure 1-12 – Vibrating MWCNT at 1st, 2nd natural frequencies ("a" and "b", respectively)[11] [12]

Wong, et al. used a cantilever beam model to fit measured static response of an individual MWCNT subjected to deformation by an atomic force microscope tip. They obtained an average Young's modulus of 1.28 ± 0.59 TPa for six diameters of tubes ranging from 26 to 76 nm [35]. Lourie and Wagner used micro-Raman spectroscopy to estimate Young's modulus of MWCNTs that were embedded in epoxy by measuring D-band shift in compressed samples from 122 K to 264 K. Their results ranged from 1.7 to 2.4 TPa [36].

The tensile strength of multiwall carbon nanotubes has also been investigated by different groups. Yu and Ruoff, et al. measured 19 individual MWCNTs and found that the tensile strength of the outermost layer ranged from 11 – 63 GPa. They also reported Young's modulus values of the outermost layer varying from 270 – 950 GPa from their tensile data [37]. Pan, et al. fabricated a stress-strain measurement device to apply axial tensile load to 2 mm long "ropes" of aligned MWCNTs. They reported average Young's modulus and tensile strength values of 0.45 ± 0.23 TPa and 1.72 ± 0.64 GPa, respectively [38]. While these values represent individualized data points for individualized MWCNTs, it is important to realize that property values for bulk materials will undoubtedly be lower due to increasing numbers of defects [12].

[11] Reprinted from Comptes Rendus Physique, 4, Rodney S. Ruoff, Dong Qian, Wing Kam Liu, Mechanical properties of carbon nanotubes: theoretical predictions and experimental measurements, Page 998, Copyright 2003, with permission from Elsevier

Common failure methods for multiwall carbon nanotubes have been studied experimentally and through molecular dynamics simulations. Under tensile strain, multiwall carbon nanotubes can experience either brittle fracture of the outer layer (dubbed a “sword-in-sheath” failure by Yu, et al. [37]) or a localized plastic deformation, as predicted by MD simulations and witnessed by High Resolution Transmission Electron Microscopy (HRTEM) performed by Marques et al. [39]. Yu et al. suggest the brittle “sword-in-sheath” failure indicates that the majority of the tensile load is carried by the outermost layer of the MWCNT, while the inner layers contribute little to load bearing through inter-layer van der Waals forces, resisting the tendency to shear with respect to each other. This effect has also been noted by Thostenson and Chou for MWCNTs embedded in epoxy matrix systems [15].

The plastic deformations witnessed by Marques were initiated by disrupting the carbon bond structure under strain using an electron beam in the TEM. These interruptions in the graphitic lattice of an MWCNT’s layers are repaired by carbon atoms restructuring themselves, in order to return to a more orderly lattice arrangement. This is accomplished by cannibalizing inner layers, and slowly stretching the nanotube into a chain of carbon atoms until only one layer remains. The final layer finally breaks and is capped by a fullerene structure [39]. This process is detailed in a sequence of TEM images shown in Figure 1-13 below. Image a shows the initial image of the nanotube where all layers are in an ordered state. Image b is the beginning of nanotube disruption formation, away from the narrow segment of the tube. Image c shows total disruption of all nanotube layers. In image d, the nanotube reorganizes itself into a new ordered state with smaller diameter. The sequence of a-d occurs several times before state e is reached. In image e, only a single-wall carbon nanotube remains from this thinning process. Lastly, in image f, the SWCNT breaks and the open ends cap themselves.

Others, such as Wei, et al. and Andrews and Weisenberger, note the necking effect seen by Marques, et al. begins with structural defects like the Stone-Wales defect [19, 40]

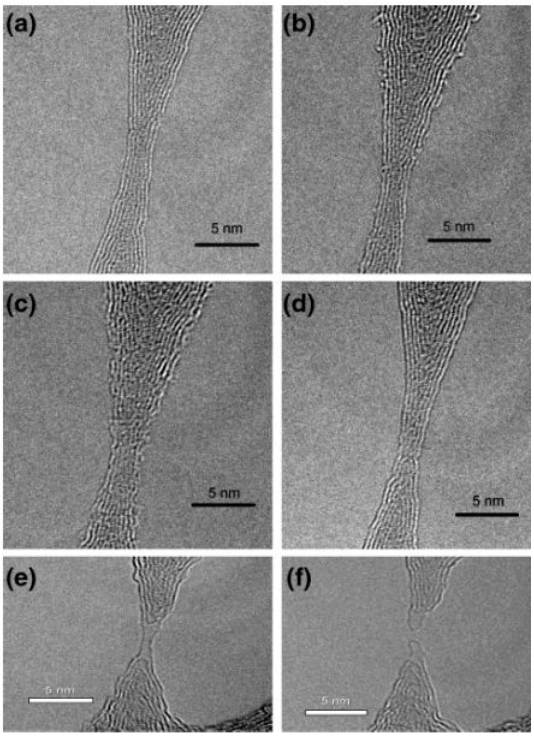

Figure 1-13 - TEM images of MWCNT reconstructive properties under tensile strain[12] [39]

Mechanical failure stemming from compression tends to be a bit more forgiving in carbon nanotubes than the full destruction of the tube geometry experienced in tensile failure. Chang, et al. report carbon nanotubes can be bent at an angle larger than 140° without exhibiting any mechanical failures or loss in phonon transport[25]. SEM Images from this study showing nanotube bend radius's effect on thermal conductivity are reproduced from [25], and presented in Figure 1-14 below. This combined SEM/chart shows how two carbon nanotubes and one boron nitride nanotube are subjected to sharp bend radii before any damage is noted and any relevant change in normalized thermal conductivity is recorded. The images were taken at different points of a bending cycle.

[12] Reprinted with permission from Nano Letters, Vol. 4 No. 5, M. A. L. Marques, H. E. Troiani, M. Miki-Yoshida, M. Jose-Yacaman, A. Rubio, "On the Breaking of Carbon Nanotubes Under Tension", Page 812, Copyright 2004 American Chemical Society

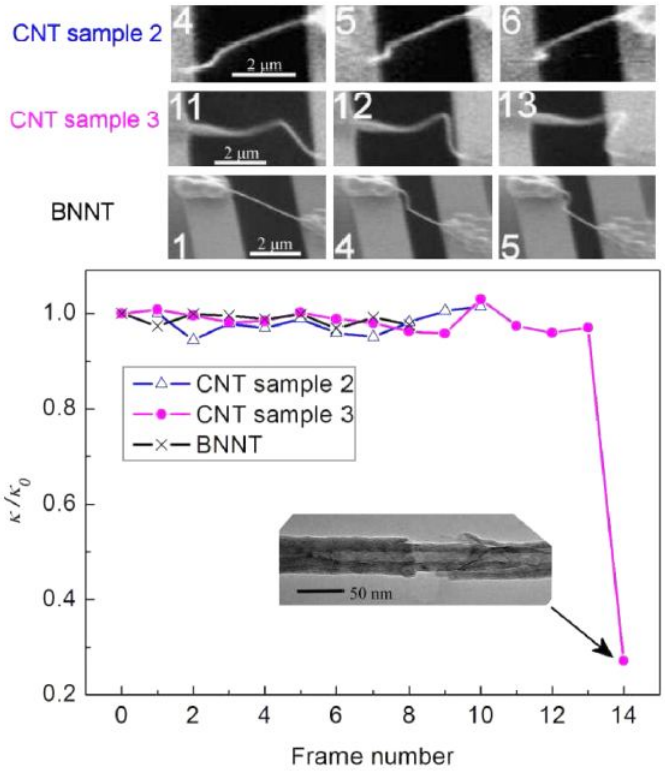

Figure 1-14 – Effect of nanotube bend radius on thermal conductivity[13] [25]

The natural resilience of nanotubes as presented above is one of the most useful traits they possess for TIM applications. The ability to flex, conform, and contact surfaces under load is critical for good thermal transfer through an interface. Nanotubes retain this resilience and flexible nature when applied in bulk forms like freestanding arrays, as shown in Figure 1-15 below. The SEM image on the left shows buckling of MWCNTs observed under compressive force. The MWCNT array shows a distinct line where tubes begin to buckle and compress when sandwiched between two aluminum substrates. The SEM image on the right shows MWCNT tips bent over to conform to aluminum Substrate under compressive force.

[13] Reprinted with the Author's permission from Physical Review Letters, Vol. 99, 045901, C. W. Chang, D. Okawa, H. Garcia, A. Majumdar, A. Zettl, "Nanotube Phonon Waveguide", Page 3, Copyright 2007 by American Physical Society

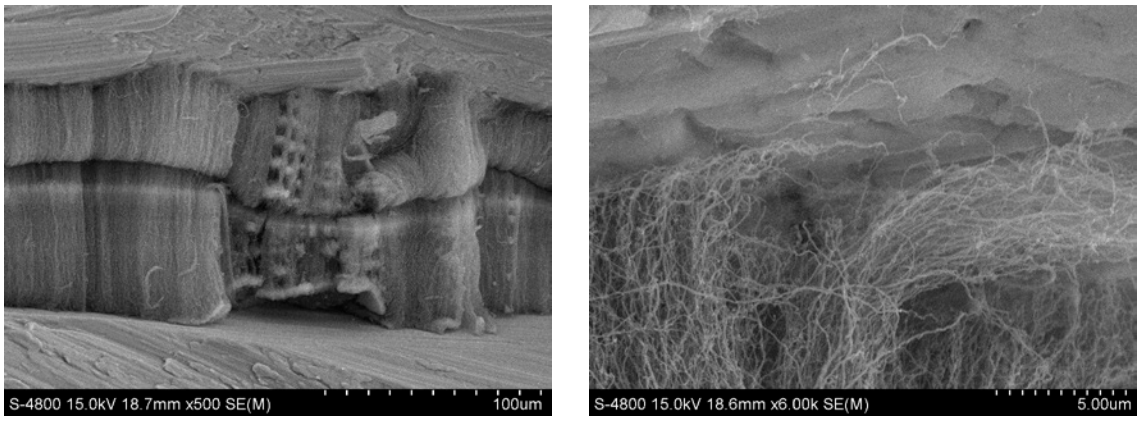

Figure 1-15 – Buckling and Conforming of MWCNT arrays under compressive force

Suhr et al. reported on the fatigue resistance of carbon nanotube arrays subjected to cyclic compression. They found vertically aligned carbon nanotube arrays exhibit preconditioning behaviors, viscoelasticity-induced hysteresis, non-linear elasticity and stress-relaxation, as well as the ability to withstand large deformations [24].

Suhr's report of preconditioning indicates his nanotube arrays settle into a relatively constant modulus of 0.58 MPa after 60 cycles, where the arrays initially reported a modulus value of 0.73 MPa. Once preconditioned, the nanotubes were cycled to fatigue. Compressive strains of up to 15% caused no fatigue damage up to a half million cycles. Above 15% strain, the nanotubes showed degradation through decreased recovered thickness value as early as 75,000 cycles.

The viscoelastic hysteresis behavior shows the arrays are slower to recover when a load is removed; much like a memory foam pillow slowly expands after compression. With increased cycle count, the arrays tend toward a less extreme hysteresis difference, as the nanotubes become preconditioned and lose some compressive capacity. This viscoelasticity is also evident when holding a sample at a fixed compression, as the reported stress slowly decreases over time.

The nonlinear elasticity measurements show two distinct regions of stiffness. First a modulus of 0.75 MPa up to a critical strain of nearly 57% strain is seen. Above this value, the second and stiffer regime takes over, as the modulus slope increases dramatically toward values greater than 2 MPa [24]. This serves as another indicator that the nanotubes have reached a compressive limit, and have little room left to reorganize themselves to accommodate more stress.

Lastly throughout all of Suhr et al.'s tests, it was noted that the nanotubes were capable of withstanding large deflections. Tubes would recover their alignment and orientation while releasing the energy stored by compression as heat. Any kinks or defects gained during deflection are not lost when the tubes recover their original position. Charts detailing the viscoelastic hysteresis/preconditioning behaviors (left) and non-linear elasticity regimes (right) are reproduced from [24] in Figure 1-16 below.

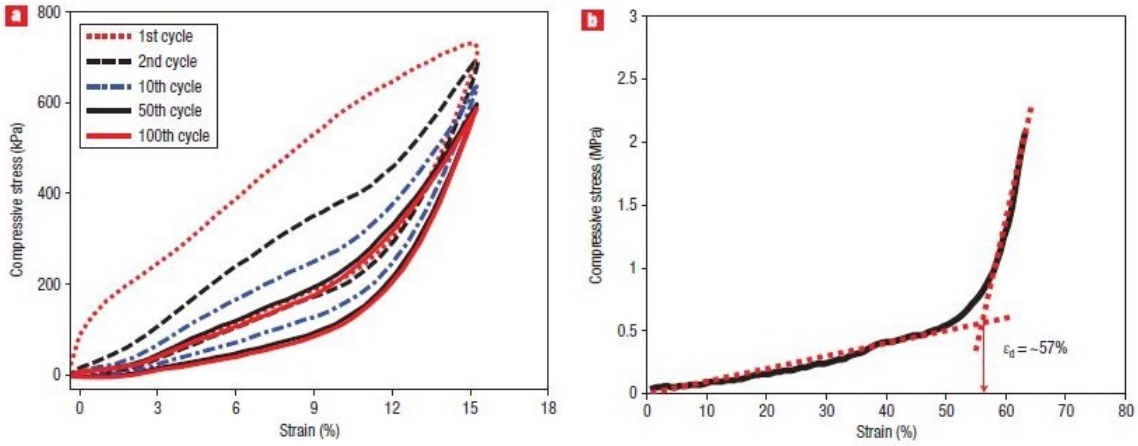

Figure 1-16 – Viscoelastic Hysteresis and Non-linear elasticity of MWCNT arrays, courtesy of Nature Publishing Group[14] [24]

Carbon nanotubes that do fail in compression will often buckle or kink, resulting in a somewhat flattened cross section. When placed in close proximity to another carbon nanotube (such as in a free standing array situation), Ruoff et al. found that an individual carbon nanotube will no longer maintain a perfectly cylindrical cross section due to the van der Waals interactions between it and its neighbor[41]. This natural interaction places many carbon nanotubes one step closer to a buckling or kinking failure mode. Should the tube collapse completely, its interlayer interactions take on a characteristic like layers of stacked graphene sheets[12].

[14] Adapted by permission from Macmillan Publishers Ltd: NATURE NANOTECHNOLOGY, Suhr, J., P. Victor, et al. "Fatigue resistance of aligned carbon nanotube arrays under cyclic compression", copyright 2007

1.4.5 Dry Carbon Nanotube Adhesion

For years, scientists have studied the natural climbing ability of geckos. As early as 1913, descriptions were published of microscopic bristles on the undersides of gecko feet being associated with this climbing ability [45]. It was discovered that a gecko's foot is covered by nearly half a million keratinous hairs of micrometer scale, with each hair projecting hundreds of spatula shaped structures less than 1 micron [46]. Carbon nanotubes possess a natural adhesive quality similar to the foot of a gecko, due to the cumulative effect of van der Waals forces experienced when the sidewalls of nanotubes make contact with a substrate [47-49].

Research groups have studied the adhesion forces created by nanotubes in contact with substrate surfaces. In 2006, Zhao et al. measured the normal and shear adhesion strengths of MWCNT arrays as functions of attachment cycles and attachment area. They found maximum normal and shear adhesion strengths of 11.7 N/cm^2 and 7.8 N/cm^2 (respectively), as well as an inverse relationship between apparent contact area and adhesion strength [48]. They attached and removed array samples up to eight times, noticing that the reported adhesion strength values would gradually degrade for the first few cycles. After about 3 cycles, the strength values would reach a lower steady-state value. They also noted that shorter arrays (around 5 – 10 micron) displayed larger adhesive strengths, whereas longer arrays (around 100 micron) displayed weak adhesive strength on the order of 2 mN/cm^2.

Zhao et al.'s nanotubes were synthesized via CVD, and they point out their arrays had a top "canopy" layer which consisted of randomly oriented, tangled nanotube tips. They considered this a significant difference between nanotube arrays and gecko feet, since the canopy would block some of the nanotubes from contacting the substrate. They proved this top layer was problematic by plasma etching this surface away from an array of more than 50 micron thickness which previously showed negligible adhesion strength. Testing post plasma etch showed an improvement in the adhesion up to a few N/cm^2 of adhesion strength [48].

Two years later, Qu et al. studied the normal and shear adhesion strengths of MWCNTs and found vastly different results. Qu's group recorded the adhesion force for different samples of nanotubes with thicknesses ranging from near 10 micron to 150 micron. Instead of finding normal adhesion strength to be dominant, they measured average normal and shear adhesion

strengths near 20 N/cm^2 and 100 N/cm^2 (respectively) for arrays near 150 micron length [47]. This result is exactly opposite of those published by Zhao et al. two years earlier.

Qu's group credits the same tangled-on-top, straight-through-the-middle nanotube array construction for the incredible shear adhesion strength that Zhao's group claims inhibits contact for adhesion. They also used plasma etching to compare adhesive strengths of nanotube layers with and without the tangled top nanotube layer, finding a significant increase in adhesion strength when this layer was left intact. SEM images show that after shear loading is applied, this tangled layer actually aligns itself and provides increased sidewall nanotube-to-substrate contact (and hence, higher shear adhesion force)[47].

To demonstrate the incredible shear adhesion capability of carbon nanotubes, they glued a wire to the back side of a silicon nanotube growth substrate with a 4mm x 4mm x 150 micron nanotube array sample on the other side. They stuck the nanotubes to a vertical glass slide and suspended a 1480 gram textbook from it. A 2 kg preload was applied in the normal direction to initially adhere the nanotube/substrate hanger to the glass slide (Image A, below). Images B and C show the aligned MWCNT array used. This feat is presented in Figure 1-17 below.

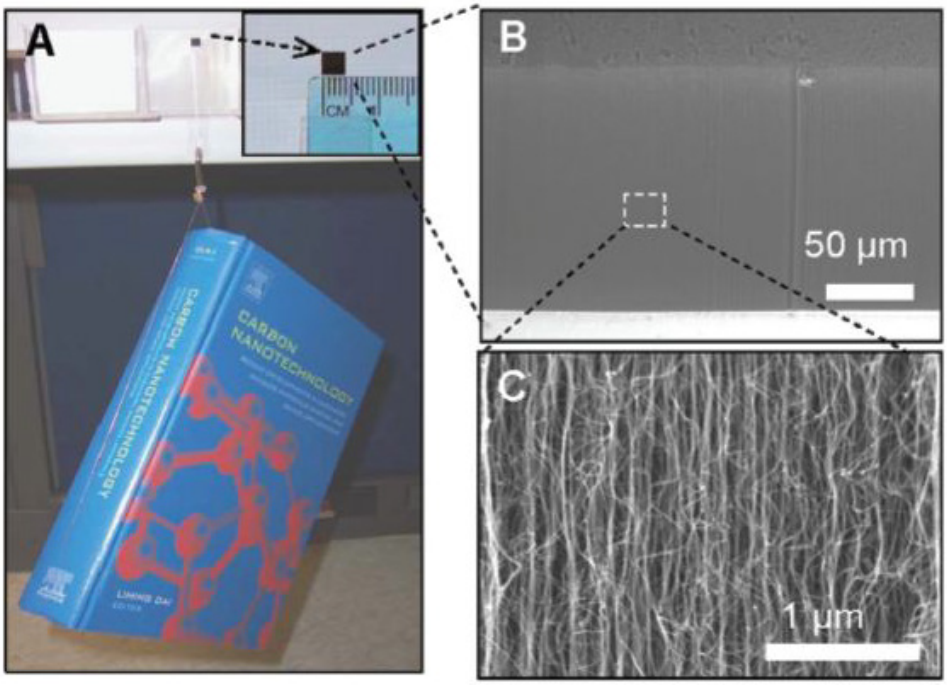

Figure 1-17 - Suspending a textbook from carbon nanotubes[15] [47]

1.5 Conclusion

Since their discovery in 1991, multiwall carbon nanotubes have been the focus of numerous research efforts and attempts to capitalize on the outstanding thermal and mechanical properties they possess. Their natural tendency to grow in highly aligned arrays makes them ideal candidates for use as thermal interface materials. Their vertically aligned, highly graphitic and largely defect free nature allows for a large phonon mean free path, and leads to excellent heat conduction dominated by phonon transport through their structure.

MWCNTs have been shown to be a truly unique material with outstanding thermal and mechanical properties. Individually, they possess incredibly high thermal conductivity and mechanical resiliency. In a bulk format such as aligned array TIMs, outstanding mechanical properties allow them to conform to substrate surfaces easily and allow for repeated assembly

[15] From Science, 322, 5899 Liangti Qu, Liming Dai, et al. "Carbon Nanotube Arrays with Strong Shear Binding-On and Easy Normal Lifting-Off", Copyright 2008. Reprinted with permission from AAAS.

of an interface system. Thermally, bulk arrays show conductivity values that are not quite as extreme as their constituents, but they still perform admirably as TIM materials.

Successful attempts have been made to impart the excellent thermal and mechanical properties of MWCNTs to composites by including them in the layup of the material itself. Examples of this include using aligned MWCNT arrays between plies of unidirectional composite for increased fracture toughness, as well as direct synthesis of MWCNTs on 2D woven carbon fiber fabric, producing a 3D composite with improved thermal and mechanical properties.

Finally, incredible shear adhesion capabilities of carbon nanotubes are shown to be a function of the van der Waals forces between the millions of nanotube sidewalls and the surfaces they touch. This allows arrays to support tremendous shear forces, as well as become a reusable thermal interface material by preferentially sticking to one side of an interface.

Chapter 2 Multiwall Carbon Nanotube Arrays as a TIM in All-Aluminum Systems

2.1 Introduction

The inherent vertical alignment of MWCNT arrays grown through CVD synthesis creates a thin bulk material with a large mean free path for phonon-based heat conduction. Additionally, the deflection capability of individual nanotubes within the array allows a higher percentage of the total array to make contact with irregular substrate surfaces. Within this chapter, the physical properties of synthesized MWCNT arrays which affect their performance as a TIM in two layer, "sandwich" stack aluminum systems will be studied. Such properties include array thickness, areal and bulk densities, array cleanliness, and volumetric packing fraction. It is hypothesized the best performing array TIMs will be thin, possess high bulk and/or areal densities, have high volumetric packing fractions, and be free from amorphous carbon deposits.

2.2 Experimental

Thermal analysis of an aligned MWCNT array's performance as a TIM is carried out through the laser flash method for measuring diffusivity. This method has been well researched and has been implemented with several models for heat diffusion, including corrections for laser pulse effects and radial heat losses, as well as models for multiple layer diffusivity measurements[50-57]. Analysis was conducted using an LFA 427 Laser Flash Analysis (LFA) system produced by Netzsch.

2.2.1 Carbon Nanotube Synthesis

The vertically aligned MWCNTs used in this study were synthesized in-house through a CVD process described in detail in patents and publications by Jacques et al. and Andrews et al. [58, 59]. During a typical nanotube synthesis, a metal catalyst is dissolved in a liquid hydrocarbon to form a feed mixture. The preferred mixture used at CAER consists of ferrocene metal catalyst and xylene hydrocarbon solution. Ferrocene is used because it is an excellent source of iron catalyst particles (which helps seed nanotube growth) while xylene is the source of carbon used in nanotube growth. This mixture is prepared at approximately 0.75 atomic % Fe to C ratio, and is preheated to 175 °C as it feeds through a capillary. This temperature is above the boiling point of xylene (138.5 °C [60]), yet below the decomposition point of ferrocene (190 °C [59]).

Upon exiting the capillary tube, the mixture is instantaneously volatilized due to the elevated temperature and is brought into the reaction furnace by an inert carrier gas. Usually, a preferred combination of 10 vol % hydrogen with either nitrogen or argon is used as the carrier. Quartz slide substrates are fed through a gas curtain entrance (to maintain furnace atmosphere) and into the reaction zone on a conveyor belt at a rate allowing residence times between 10 and 120 minutes. This allows nanotubes to form from iron catalyst particles which have deposited on the slides from the atomized feed mixture. The reaction occurs at a temperature between 650 °C and 850 °C, with attention given to deliver feed solution at an ideal rate. This rate maintains a partial pressure of carbon between 48 and 150 millibar to avoid triggering co-generation of amorphous carbon deposits within and on top of synthesized arrays.

Amorphous carbon lacks the ordered structure of a carbon nanotube, and does nothing to aid thermal transport. Instead, it insulates surfaces it contacts from heat transfer. Clearly, it is preferred to produce an array with a minimum amount of amorphous carbon deposits, and methods of cleaning or purifying arrays burdened by these deposits will be discussed in a later chapter of this work.

2.2.2 Dry Array Sample Construction with Aluminum Substrates

In order to characterize the effect of varying nanotube physical properties on overall performance as a thermal interface material, aluminum substrates were chosen as a well known baseline material. Disc shaped substrates for LFA testing were machined out of aluminum plate to 14 mm outer diameters on a CNC mill. A multipurpose 6061-T6511 aluminum alloy with both mill and mirror finish sides was selected to represent a standard engineering material. Surface roughness measurements of each finish were taken with a TR100 Portable Surface Roughness Tester (shown in Figure 2-1 below). Aluminum surface roughness values were averaged from 22 measurements across each side of the plate, where R_A = 0.13 µm for mill finish and 0.01 µm for mirror finish.

Figure 2-1 - TR100 Surface Roughness Tester

Two layer LFA samples were assembled in a special sample holder produced by Netzsch for use with the LFA 427 Laser Flash Analyzer instrument. It consists of a steel alloy cylinder with an internally threaded sample well of 15 mm diameter, with an internal shoulder for substrates to rest on. A fine thread hollow-lock set screw lubricated with dry graphite spray is tightened on top of the substrates with a supplied torque driver to allow precise and repeatable application of pressure loads to substrates. The entire assembly is made of steel alloy, which will not flex under moderate torque loading. This material possesses a low thermal conductivity which will not provide an alternate conduction path. This avoids biasing thermal results by affecting heat flow in the sample. Figure 2-2 below contains a diagram and picture of the sample holder.

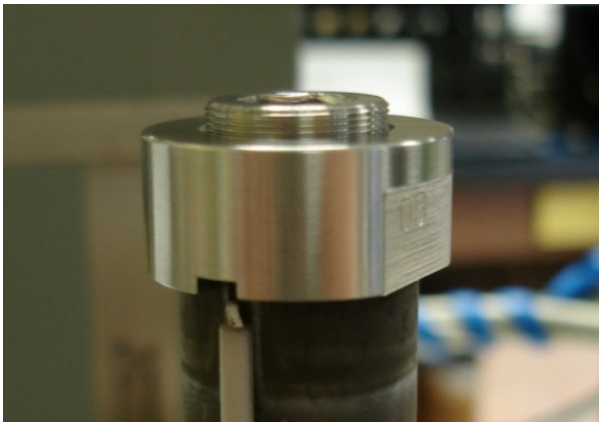

Figure 2-2 - Compression Sample Holder loaded on the LFA's sample tower

After the sample has been constructed, the exposed bottom and top substrate surfaces are coated with a thin layer of spray graphite, as recommended by Netzsch [61]. For the "front" substrate face, this produces a highly conductive surface with low reflectivity, eliminating possible laser reflections and promoting total energy absorption from the laser flash. A graphite coating on the "back" substrate face increases the total emissivity value of the surface. This allows the LFA software to accurately measure sample temperature rise using an Infrared (IR) detector on the back face. More details about the LFA instrument will be discussed in the following section.

2.2.3 Thermal Testing

For thermal measurements in this work, a Netzsch LFA 427 Laser Flash Analyzer was used. A diagram of the measurement components can be seen in Figure 2-3, below.

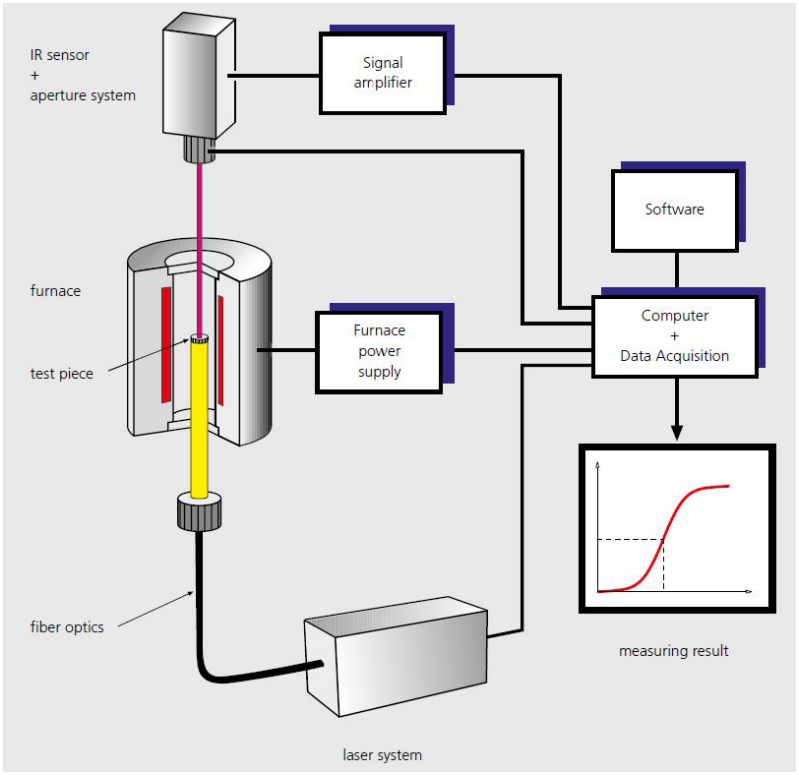

Figure 2-3 -LFA 427 Testing System Diagram[16]

[16] Image reprinted with permission of Netzsch Instruments, http://www.netzsch-thermal-analysis.com/download/LFA427_E_0311_25.pdf

In the most simplistic terms, the LFA instrument consists of a highly accurate clock and a thermometer. When a sample is tested, a laser pulse flashes energy onto the front side of the sample. Just before the pulse, the clock starts counting and the temperature history starts recording. The minimum and maximum temperatures are noted, and a normalized temperature rise curve is generated. A quantity known as the "half-rise time," is read off the curve. This value is used in thermal models like those of Parker et al. [50], Cape and Lehman [51], and Cowan [52] to determine the thermal diffusivity of the sample. When combined with the specific heat and bulk density of the sample, the thermal conductivity can be directly calculated. At this point, a discussion of the thermal models used in measuring thermal diffusivity is required.

2.2.3.1 Parker Model for Thermal Diffusivity

The flash method for determining thermal diffusivity, heat capacity, and thermal conductivity published by Parker et al. in 1963 is the basis for thermal measurements made in the Netzsch LFA 427. It was developed as a way to reliably measure thermal properties of materials while avoiding problems related to contact resistances in contact –based measurements. It was also designed to be faster than contemporary methods, and was capable of measurements at higher temperatures than allowed by other methods. Parker et al.'s model of thermal diffusivity results in this well known relation, where α is thermal diffusivity, L is sample thickness, and $t_{1/2}$ is the sample "half max time."

$$\alpha = \frac{1.38L^2}{\pi^2 t_{1/2}} \tag{2.1}$$

The derivation of this equation is as follows from Parker, and rests on these assumptions and boundary conditions:

- Heat flow is one-dimensional
- The pulse width of the incident laser flash is negligible compared with the time necessary for the heat flux to propagate through the sample (heat pulse is instantaneous)
- Penetration depth of the laser is small
- Material properties are ideally temperature independent, or at the least, not *strongly* temperature dependent
- Heat losses from sample surfaces are negligible

To begin the derivation, it is assumed an initial temperature distribution of *T(x,0)* in a thermally insulated solid of uniform thickness, *L*, exists. If this is the case, the temperature distribution at any later time *t,* as given by Carslaw and Jaeger (and used in Parker et al.[50]) is:

$$T(x,t) = \frac{1}{L}\int_0^L T(x,0)dx + \frac{2}{L}\sum_{n=1}^{\infty} exp\left(\frac{-n^2\pi^2\alpha t}{L^2}\right) * \cos\frac{n\pi x}{L}\int_0^L T(x,0)\cos\frac{n\pi x}{L}dx \tag{2.2}$$

Also, an initial condition is assumed where a pulse of radiant energy, *Q (i.e. laser light)*, is instantaneously and uniformly absorbed in a small depth *g*, at the front flashed surface of the sample (x=0). In a thermally insulated solid of uniform thickness*,* the temperature distribution at that instant is given by

$$T(x,0) = \frac{Q}{DCg} \quad for\ 0 < x < g \tag{2.3}$$

and

$$T(x,0) = 0 \quad for\ g < x < L \tag{2.4}$$

Where *D* represents density and *C* represents heat capacity.

Using these initial conditions, equation (2.2) can be rewritten as

$$T(x,t) = \frac{Q}{DCL}\left[1 + 2\sum_{n=1}^{\infty}\cos\frac{n\pi x}{L} * \left(\frac{\sin(n\pi g/L)}{(n\pi g/L)}\right) * exp\left(\frac{-n^2\pi^2}{L^2}\alpha t\right)\right] \tag{2.5}$$

where only a few terms of the summation will be needed. Because the assumed incident laser pulse only penetrates a very small distance into the sample face *g*, it is known that $n\pi g/L$ will be a very small value. Using the small angle approximation for sine functions, one can safely assume $\sin(n\pi g/L) \approx\ n\pi g/L$. The temperature history on the rear face can now be expressed as

$$T(L,t) = \frac{Q}{DCL}\left[1 + 2\sum_{n=1}^{\infty}(-1)^{\mathrm{n}} * exp\left(\frac{-n^2\pi^2}{L^2}\alpha t\right)\right] \tag{2.6}$$

Next, two dimensionless parameters, *V* and *ω*, are defined as

$$V(L,t) = T(L,t)/T_M \tag{2.7}$$

and

$$\omega = \pi^2\alpha t/L^2 \tag{2.8}$$

where T_M represents the maximum temperature of the rear surface.

Upon combining the rear face temperature equation (2.6), with the dimensionless parameters in equations (2.7), and (2.8), a simplified relation for the normalized rear surface temperature *V* is found.

$$V = 1 + 2\sum_{n=1}^{\infty}(-1)^n \exp\left(-n^2\omega\right) \tag{2.9}$$

From a plot of equation (2.9), the half time "$t_{1/2}$" can be read where *V*=0.5. At this point, the parameter ω = 1.38, which allows algebraic manipulation of equation (2.8). Upon replacing *t* with $t_{1/2}$ in equation (2.8) and solving for the thermal diffusivity parameter α, equation (2.1) is found, as shown above. This graphical identification process is illustrated in Figure 2-4 below. Here, nondimensional parameters V and ω are plotted, and the half time "$t_{1/2}$" can be read off the plot where V=0.5.

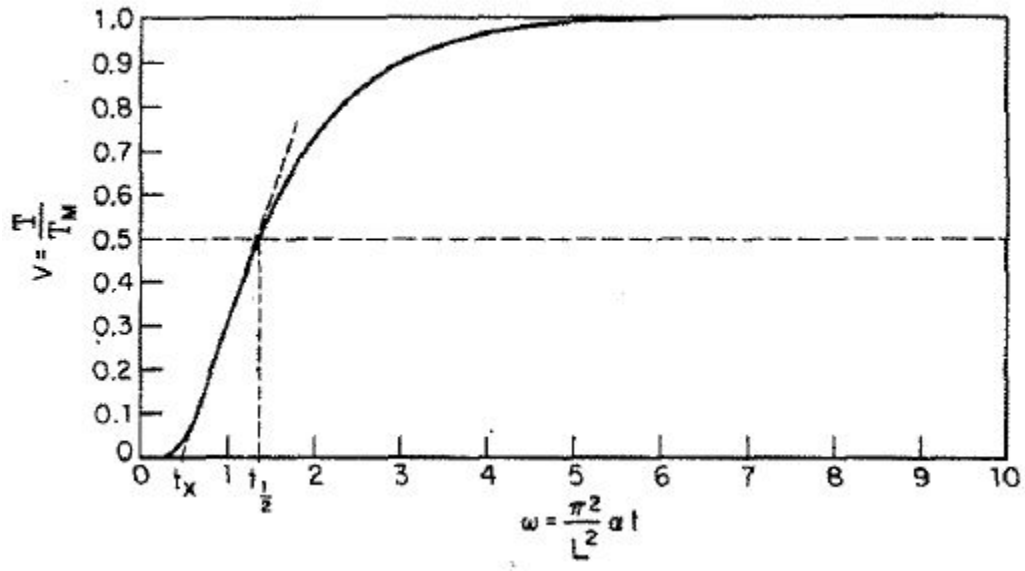

Figure 2-4 - Rear surface temperature history from flash diffusivity measurements[17] [50]

[17] Reprinted with permission from Parker, W.J., et al., *Flash Method of Determining Thermal Diffusivity, Heat Capacity, and Thermal Conductivity.* Journal of Applied Physics, 1963. **32**(9): p. 1679 – 1684. Copyright 1961, American Institute of Physics.

2.2.3.2 Cape-Lehman Model for Thermal Diffusivity, Including Pulse Correction

The model of thermal diffusivity proposed by Parker et al. operates in an adiabatic system, due to the assumption of negligible heat loss from the sample to the surroundings. This is not always an accurate representation of a thermal system, especially at elevated temperature[51, 53]. Cape and Lehman introduce two extensions of the basic Parker framework for the heat conduction problem. One extension is a finite pulse width correction, which is needed when the characteristic thermal transit time of a thin sample material t_c, is on the same order as the duration of the heat pulse. This situation causes the heat rise to appear later than it should, and overestimates the appropriate half max time, and thereby, the appropriate diffusivity. The second extension accounts for radiative heat losses which occur when measuring thicker samples at high temperature.

Cape and Lehman considered the same cylindrical sample geometry used in the Netzsch LFA 427. They derived their solutions as shown in [51], the highlights of which are as follows:

Considering a cylindrical sample flashed by a pulsed heat source with front face at x=0, back face at x=a, and with radius r_0, the heat flow in such a sample is governed by equation (2.10) when thermal diffusivity is independent of temperature.

$$-\nabla^2\delta(x,r,t)+\frac{\delta(x,r,t)}{\alpha}=\frac{q(x,r,t)}{k} \tag{2.10}$$

During the flash diffusivity experiment, the sample temperature rises only a little over the ambient temperature, T_0. The boundary conditions for this equation are derived from the Stefan-Boltzmann radiation law, and are:

$$\frac{d\delta(0,r,t)}{dx}=\nu_x\delta(0,r,t) \tag{2.11}$$

$$\frac{d\delta(a,r,t)}{dx}=-\nu_x\delta(a,r,t) \tag{2.12}$$

and

$$\frac{d\delta(x,r_0,t)}{dr}=-\nu_r\delta(x,r_0,t) \tag{2.13}$$

Where

$$\nu_{x,r}=4\sigma\epsilon_{x,r}\frac{{T_0}^3}{k} \tag{2.13}$$

2.3 Results

Prior to testing thermal diffusivity and thermal contact resistance properties of MWCNT arrays in stacked aluminum systems, three samples of the aluminum material were measured for baseline thermal diffusivity and specific heat values. Two test procedures were conducted for each sample, including a “one layer” test for effective thermal diffusivity of the sample stack and a “two layer” test to measure interfacial thermal contact resistance. Initially, each MWCNT array was tested as a TIM in a high pressure aluminum system. After completing tests at high pressures, it was decided to test at lower pressures to determine the onset of thermal property enhancement, as well as array property effects at lower pressures.

High pressure tests were conducted with mill and mirror finish surfaces at the interface to determine the effect of substrate roughness. All tests were conducted at 25 °C, under increasing torque settings. The torque settings were dictated by available range of the tool, a Tohnichi RTD260CN Torque Driver (shown in Figure 2-5 below).

Figure 2-5 - Tohnichi RTD260CN Torque Driver

This tool was supplied by Netzsch with their compression sample holder and equipped with a 5 mm hex-bit. The total torque range of the tool is 60 – 260 cNm of torque. The three settings used during testing were 60 cNm, 100 cNm, and 140 cNm. These equate to approximately 134 psi, 290 psi, and 447 psi (converted from Netzsch’s pressure vs. torque curve supplied with the compression sample holder, see Figure 2-7). Each sample was tested with both one and two layer methods before increasing the interfacial pressure. All samples were tested at all three pressures, in increasing order.

To summarize the conditions of the high pressure diffusivity/contact resistance studies:

- Two tests per sample (1 Layer test for diffusivity, 2 layer test for contact resistance)
- One temperature setting for all tests (25 °C)
- Two surface finishes used at the interface (mill (R_A=0.13 µm) and mirror (R_A=0.01 µm))
- Three pressures/torques (134 psi / 60 cNm, 290 psi / 100 cNm, 447psi / 140 cNm)

Low pressure tests were conducted at 0, 1, 2, 3, and 4 in-lb of torque, using a Stanley PROTO torque wrench, as pictured in Figure 2-6 below.

Figure 2-6 - Stanley PROTO Torque Driver

The pressures related to 3 and 4 in-lb of torque can be backed out from the compression curve supplied by Netzsch, and correspond to approximately 31 psi and 75 psi, respectively. Torques between 0 in-lb and 2 in-lb correspond to pressures between 0 psi and 31 psi, but exact values cannot currently be reported due to the reported range of Netzsch's curve. Figure 2-7 below shows how attempting to extrapolate this curve into the low torque domain below 3 in-lb results in negative pressure values, which are clearly unrealistic.

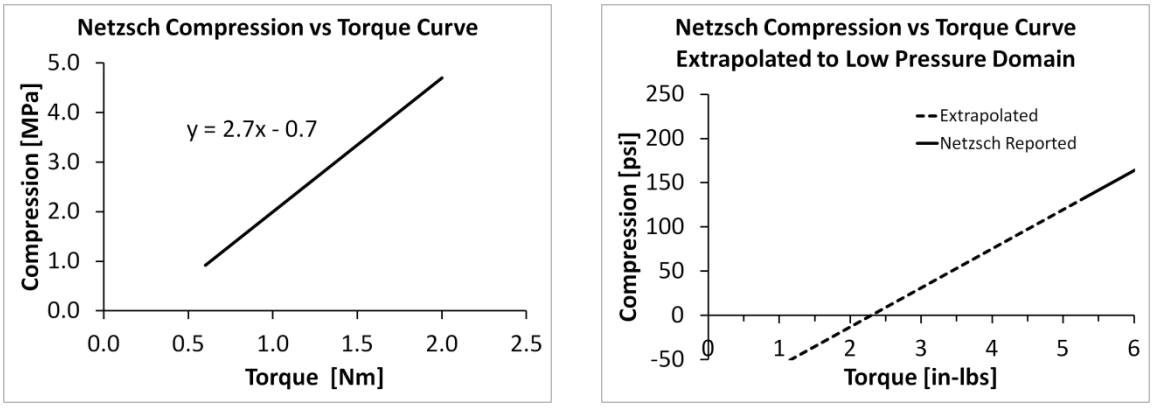

Figure 2-7 - Extension of Netzsch Compression curves into Low Pressure Domain

For the low pressure tests, aluminum substrates sanded to a 60 grit finish were the only interface roughness considered. Measurements of this surface reveal an average roughness of R_A = 1.25 µm, which is nearly 10 times rougher than the mill interface and 125 times rougher

than the mirror. The 60 grit surface treatment was chosen to illustrate the benefit of a TIM over a bare interface with relatively large surface roughness features, as there would be more space for a TIM to fill when making thermal contact. Other test parameters, including use of one and two layer tests, and a consistent testing temperature of 25 °C remained the same during these additional tests.

2.3.1 High Pressure LFA Results

To establish an overview of the results based purely on thermal performance, the relationship between thermal diffusivity and thermal contact resistance at each pressure and interface style will be considered. At this time only selected charts will be discussed for brevity's sake. All of the charts presenting these results have naming labels above the TIM data points indicating which material produced those results. TIM physical properties, as well as a complete listing of data used in the charts from this section, can be seen in Appendix A, at the end of this work.

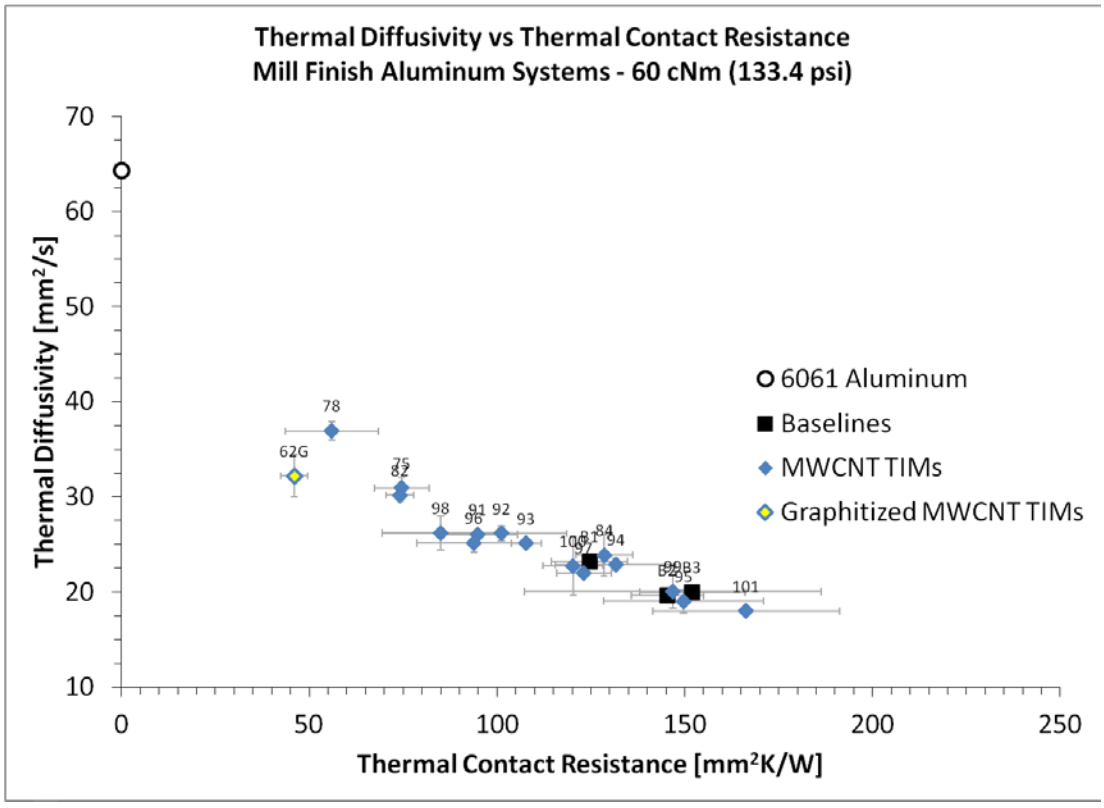

Figure 2-8 - Diffusivity vs. Contact Resistance - Mill Finish Al at 133.4 psi

From Figure 2-8, a general trend can be seen when comparing thermal diffusivity and thermal contact resistance of an LFA sample system. As the thermal diffusivity increases, thermal contact resistance decreases. As contact pressure increases, a general shift in the data spread toward regions of lower contact resistance and higher thermal diffusivity is seen.

From this chart, as well as the others across both surface finishes and all pressures listed in the appendix, it is apparent that the baseline data points do exhibit some spread. A total of three baseline systems were tested for both mill and mirror surface finishes establishing a region of baseline performance. For the mill finish systems, the baseline locations indicate that aligned MWCNT array TIMs can provide significant benefits in these systems. These benefits are not seen in all array TIMs tested, which indicates there should be some distinct features about the best performers which are lacking in the others.

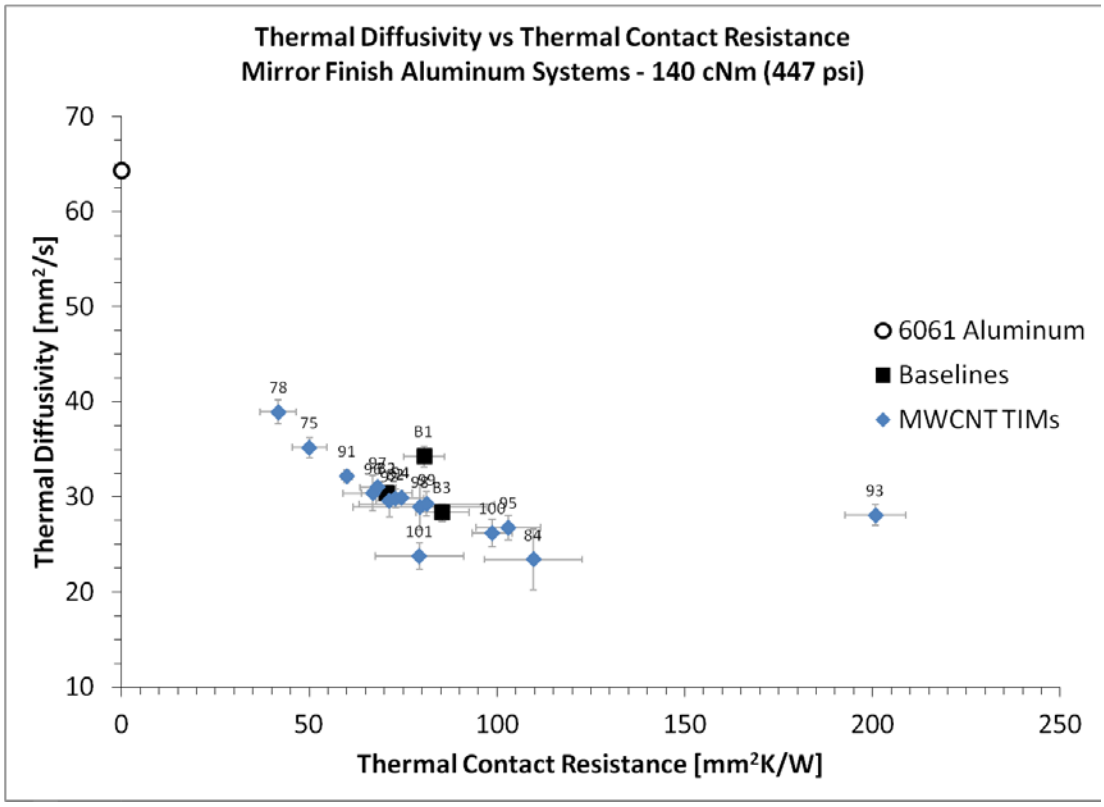

Figure 2-9 - Diffusivity vs. Contact Resistance - Mirror Finish Al at 447 psi

Examining Figure 2-9, baseline data from the mirror finish systems under extreme contact pressures indicate that most aligned MWNCT TIM materials provide less benefit here than benefits seen in mill finish systems. This is likely due to the fine surface finish of the mirror

aluminum. With fewer point contact locations than its mill finish counterpart, the mirror finish interface systems do a respectable job creating thermal contact on their own. This sets a high standard for any TIM aiming to improve upon an otherwise functional interface.

2.3.1.1 Effect of MWCNT Thickness on Thermal Performance

At this time, the spread issues with the baseline measurements will be disregarded to examine the effect of various array parameters on the thermal performance of the systems. The effect of MWCNT array thickness on the thermal diffusivity of the systems will be examined first. Figure 2-10 is representative of the influence of MWCNT array thickness on stack thermal diffusivity across all the systems.

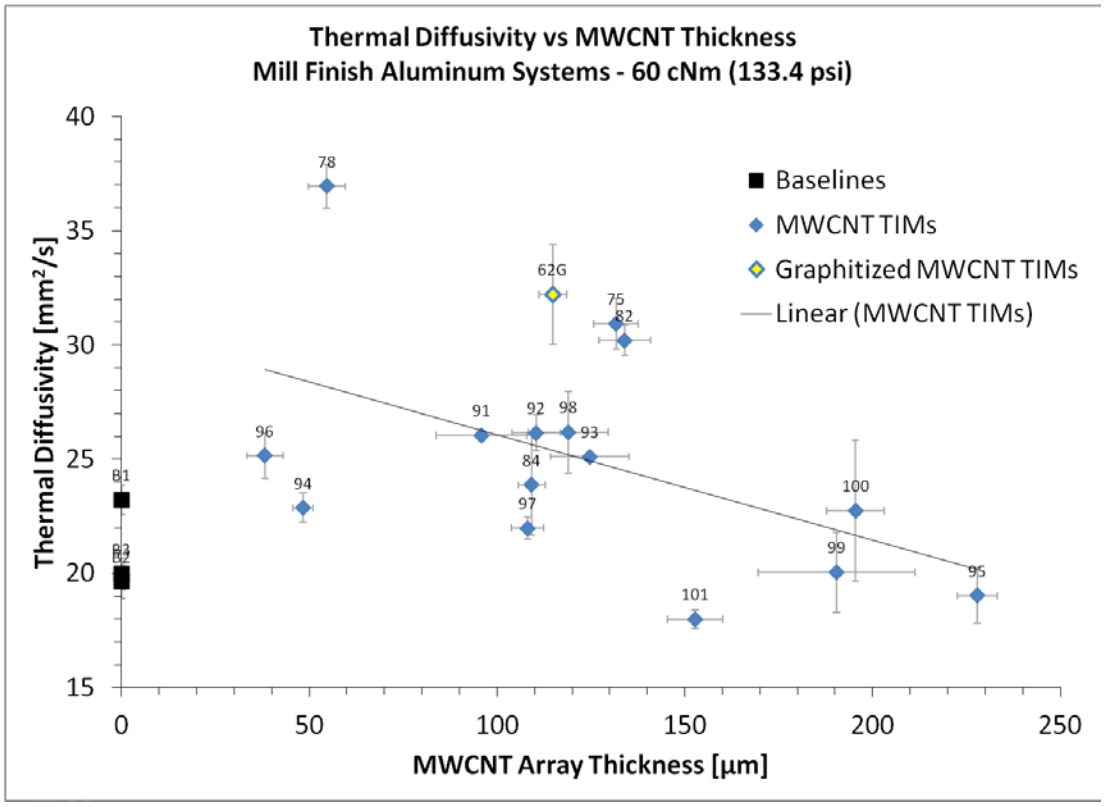

Figure 2-10 - Thermal Diffusivity vs. MWCNT Thickness - Mill Finish Al at 133.4 psi

There is a negative correlation between thermal diffusivity and array thickness such that as array thickness increases, thermal diffusivity through the stack decreases. This follows from equation (1.2), where contact resistance is a function of length and conductivity in a system with equivalent contact areas. The most important lesson from this chart is lower array thickness means potential for higher diffusivity.

2.3.1.2 *Effect of Packing Fraction on Thermal Performance*

The volumetric packing fraction, or simply "packing fraction," is an estimation of the amount of space within the aligned MWCNT array which is occupied by MWCNTs as opposed to air or other materials. In general, a higher packing fraction is a desirable trait in a MWCNT array TIM, as this indicates more conductive nanotubes are present and able to conduct heat across the interface.

Packing fraction is estimated by assuming a closely packed, hexagonal arrangement of MWCNTs within the array structure, as illustrated by Figure 2-11. Equation (2.14) is used to determine the area of the smallest hexagon which will contain three nanotubes (outlined in red dashed lines) where *h* is the assumed outer diameter of the MWCNTs to ensure maximum packing.

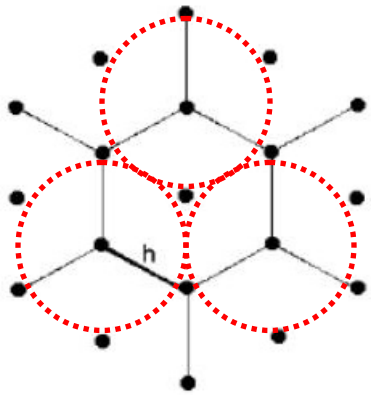

Figure 2-11 - Diagram of Assumed Close-Packed Hexagonal MWCNT Array Arrangement

$$A_{hex} = \frac{3h^2\sqrt{3}}{2} \tag{2.14}$$

The estimated number of nanotubes *actually on the slide* per unit area is calculated from the array areal density and assumed inner/outer diameters of the nanotubes. This is compared to the assumed *maximum possible number of nanotubes* per unit area (equal three times the maximum possible number of hexagons per unit area) to arrive at the ratio of nanotubes to max possible nanotubes to get packing fraction. More succinctly put:

$$Packing\ Fraction = \frac{Actual\ Nanotubes\ Per\ Area}{Max\ Possible\ Nanotubes\ Per\ Area} \tag{2.15}$$

Figure 2-12 below shows the relationship between packing fraction and thermal contact resistance in mill finish aluminum LFA systems. It is representative of the trends seen in mirror finish systems, as well as other contact pressures, which can be seen in Appendix A.

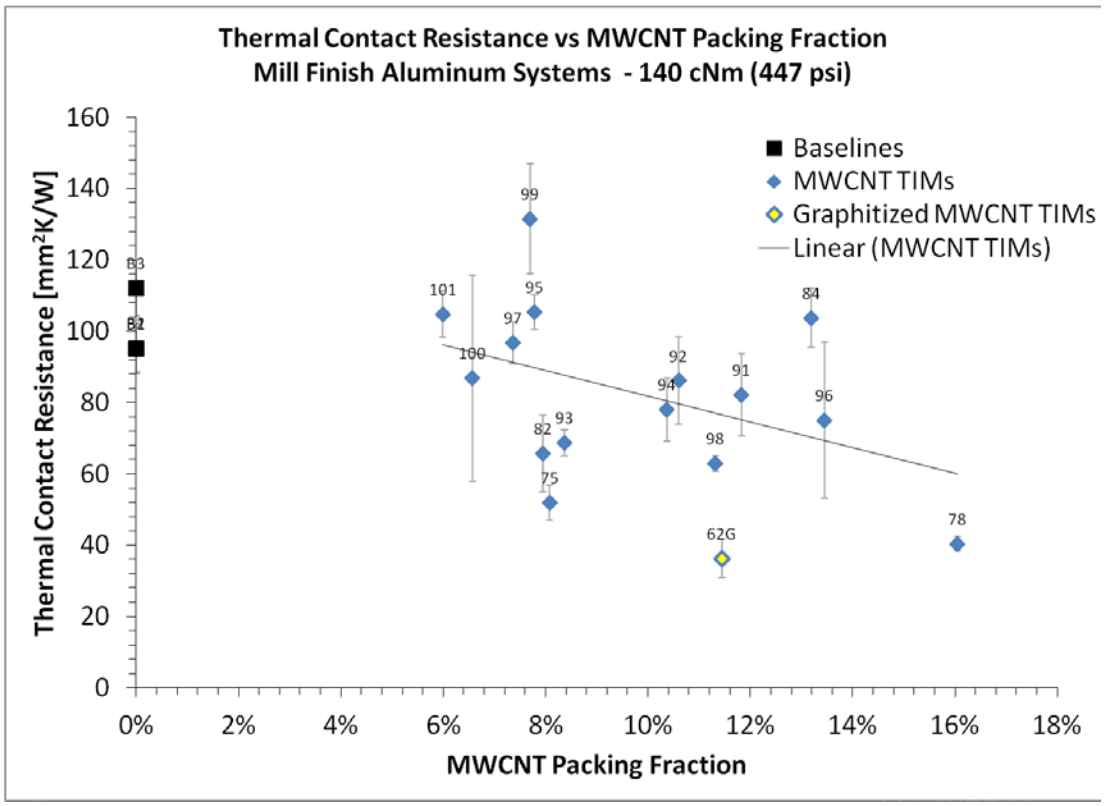

Figure 2-12 - Contact Resistance vs. MWCNT Packing Fraction - Mill Finish Al at 447 psi

From Figure 2-12 a definite negative correlation between MWCNT packing fraction and thermal contact resistance can be seen. This indicates that having a higher percentage of nanotubes occupying TIM volume (closely packed arrays) creates a higher chance of improved thermal contact and lowers thermal contact resistances across substrate surfaces.

The mill finish systems have data for a graphitized array, as well as their “as-produced” siblings. From this data, it can be seen that a high packing fraction is not the only path to lower thermal contact resistance. The graphitization process purifies MWCNT arrays by providing energy to repair damaged tubes and remove entrained iron catalyst particles[62]. The purified carbon nanotubes are much more graphitic in nature (and thereby more conductive) than their predecessors.

2.3.1.3 Effect of Areal Density on Thermal Performance

Areal density is defined as mass per unit area. The distinction of normalizing to area instead of volume separates it from its more common counterpart, bulk density (mass per unit volume). Areal density of a nanotube array is the first calculated value recorded from an array. The mass of the substrate slides is measured before and after their time in the nanotube synthesis furnace, allowing subtraction of the mass of the slide and direct measurement of the mass of the nanotube array. All slides are of known dimension, so finding areal density is a simple matter once nanotube array masses are known.

Areal density is the only array property that can be characterized prior to harvesting. This makes it the only potential candidate for deciding which array will perform best before further effort and expense is incurred to characterize it. Figure 2-13 below details representative results attempting to link areal density of aligned MWCNT array TIMs with thermal contact resistance.

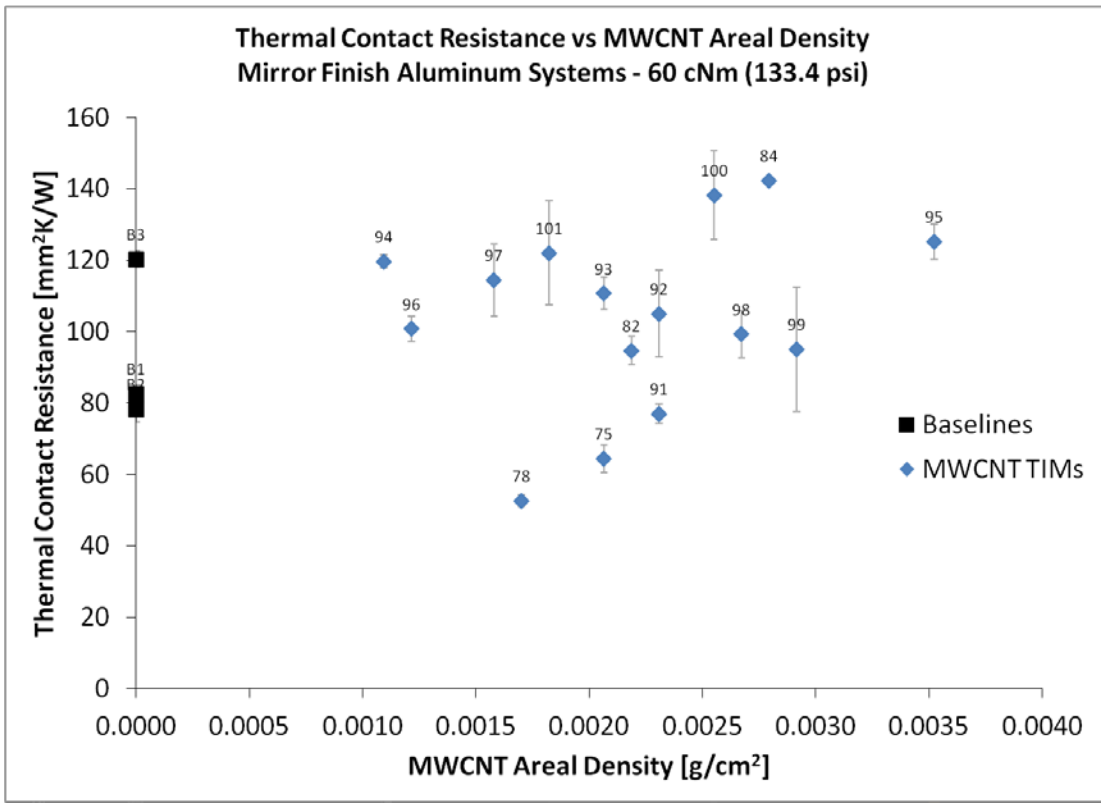

Figure 2-13 - Contact Resistance vs. Areal Density - Mirror Finish Al at 60 cNm (133.4 psi)

There is no clear pattern linking areal density of MWCNT arrays to thermal performance at high pressures.

2.3.1.4 *Effect of Bulk Density on Thermal Performance*

Bulk density is defined as mass per unit volume, and is the proper name for what most consider "density." In order to quantify this value for a nanotube array, SEM imaging must be conducted to determine the thickness of the array. Once this value is determined, areal density can be normalized to this thickness to yield bulk density. Figure 2-14 shows a loose relationship between bulk density and thermal contact resistance.

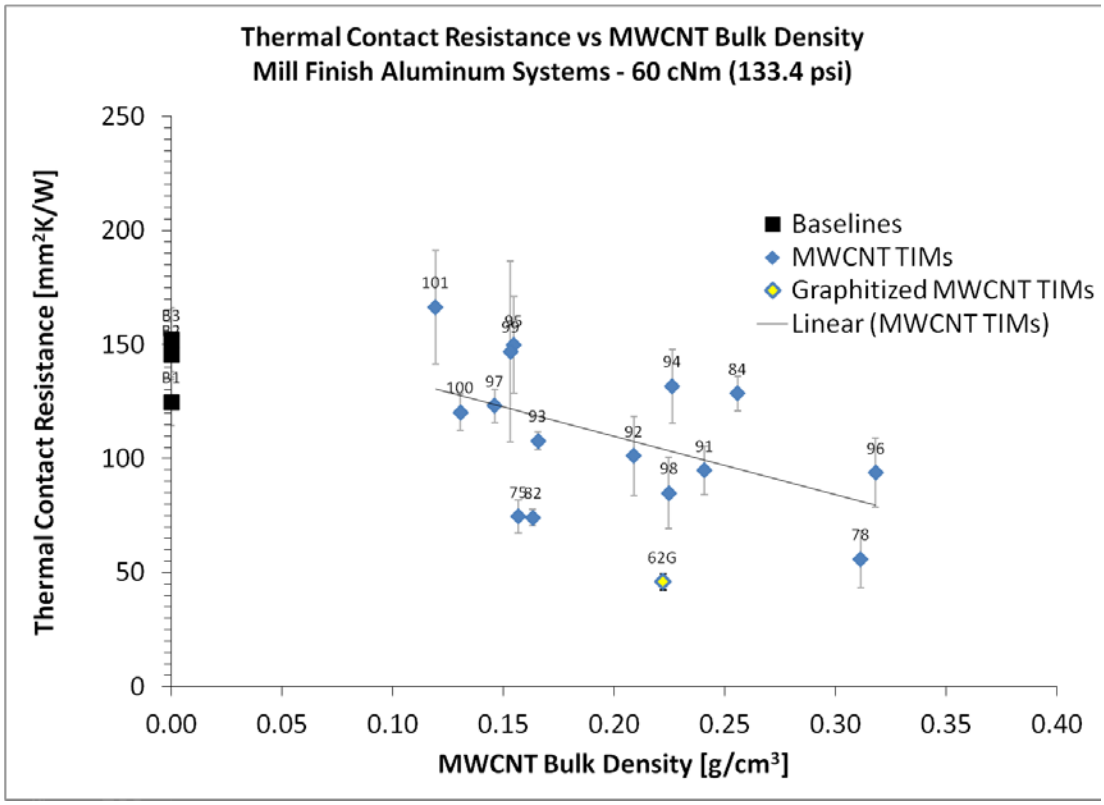

Figure 2-14 - Contact Resistance vs. Bulk Density - Mill Finish Al at 60 cNm (133.4 psi)

A rough trend exists between bulk density and thermal performance. Lower bulk density tends toward higher thermal contact resistance. This is intuitive, as lower density means less mass in the same volume, indicating fewer aligned MWCNTs occupying the interface.

2.3.1.5 *Effect of Array Cleanliness on Thermal Performance*

Array cleanliness refers to the surface conditions of the arrays themselves. The array harvesting method used results in each array having two distinct surfaces. The "bottom" surface, which was originally attached to the substrate, and the "top" surface which corresponds to the top of the produced nanotube array. The bottom surface always has a clean look to it, devoid of

amorphous carbon and packed with conductive nanotube tips. The top surface cleanliness is variable, often depending on the furnace settings, residence time, and even orientation in the furnace during synthesis. The majority of amorphous carbon that hinders array thermal performance exists on the top surface.

Attempting to quantify this cleanliness is a difficult task. Initial efforts involved measuring the change in weight after cleaning each array surface with a bagless canister vacuum, as described in Figure 2-15. Through this process, some of the amorphous carbon deposits are removed from the top surface of the array *(note: It is assumed that only mass attributed to amorphous carbon is removed during this process, not mass belonging to MWCNTs)*. A set of acrylic supports keep the vacuum cleaner tool from touching the array surface, while still remaining close enough to remove carbon deposits. An extra pair of hands is also required to hold the edges of the quartz substrate down. This ensures the combined substrate and array aren't ruined by being vacuumed up and off the table and crashing into the cleaning tool.

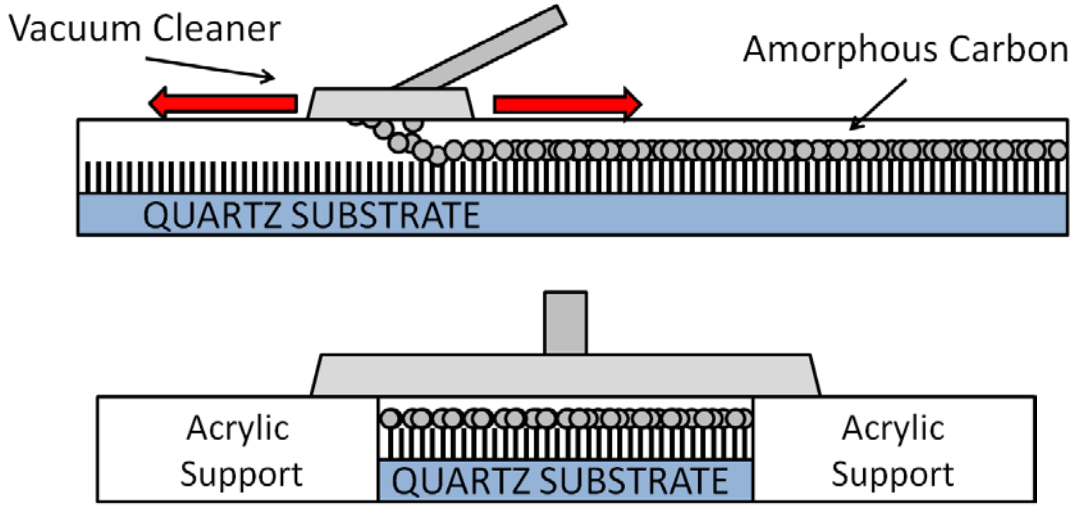

Figure 2-15 - Array Vacuum Cleaning Diagram

Beyond this cleaning method, there are very few methods developed to quantify surface cleanliness of a nanotube array. Because of this, SEM images of array surfaces become the de facto standard for qualitative surface cleanliness comparison. Figure 2-16 shows examples of these cleanliness comparisons. The image on the left is of array #37, which is one of the thinnest and cleanest arrays produced to date. It has remarkably clean surfaces on top and bottom. The image on the right is array # 97, which is an example of an array with a dirty top. The layer of amorphous carbon can be seen on the right side of the array as a brighter white line with

spherical carbon mounds resting on top of it. Below these images,

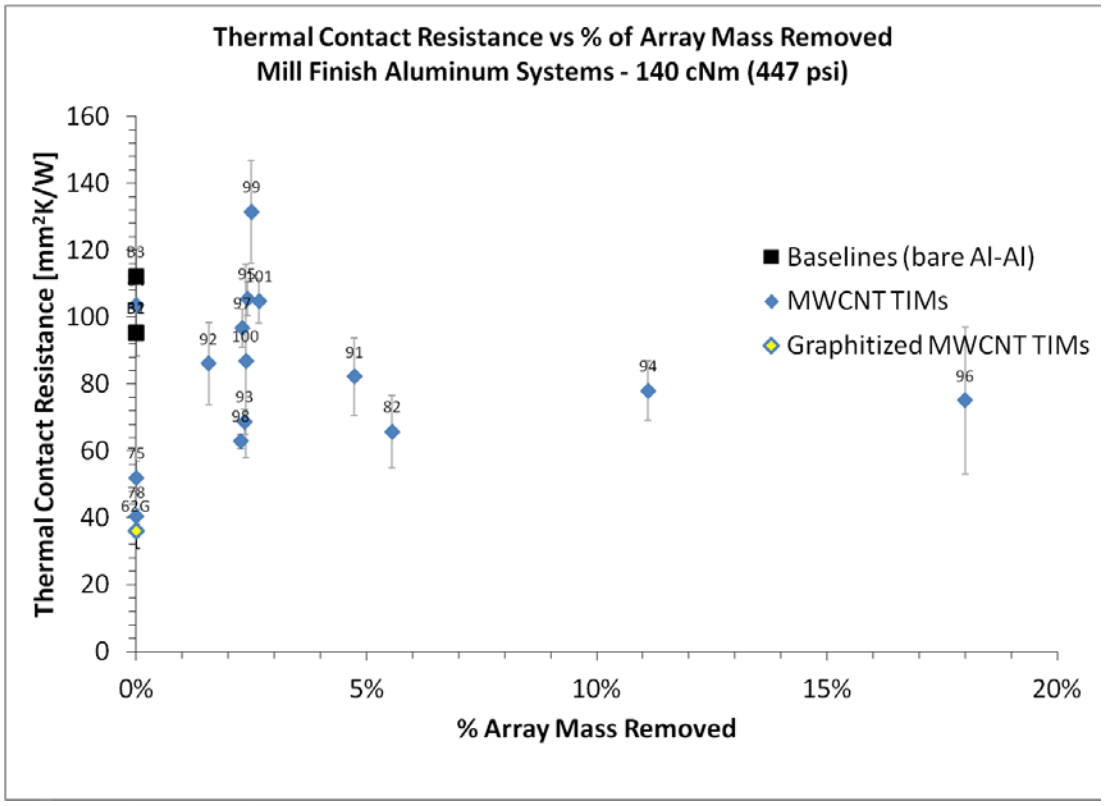

Figure 2-17 shows percentage of measured array mass removed by vacuum cleaning vs. thermal performance.

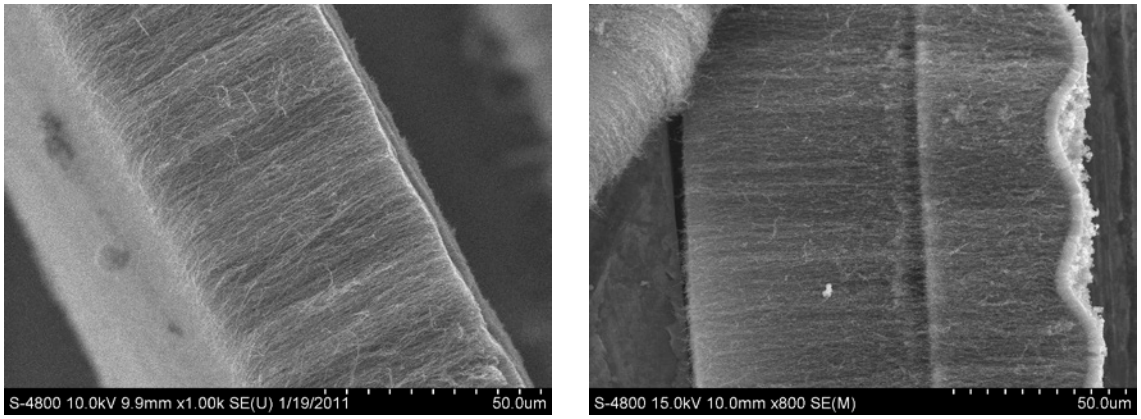

Figure 2-16 - Examples of Surface Cleanliness Examined via SEM

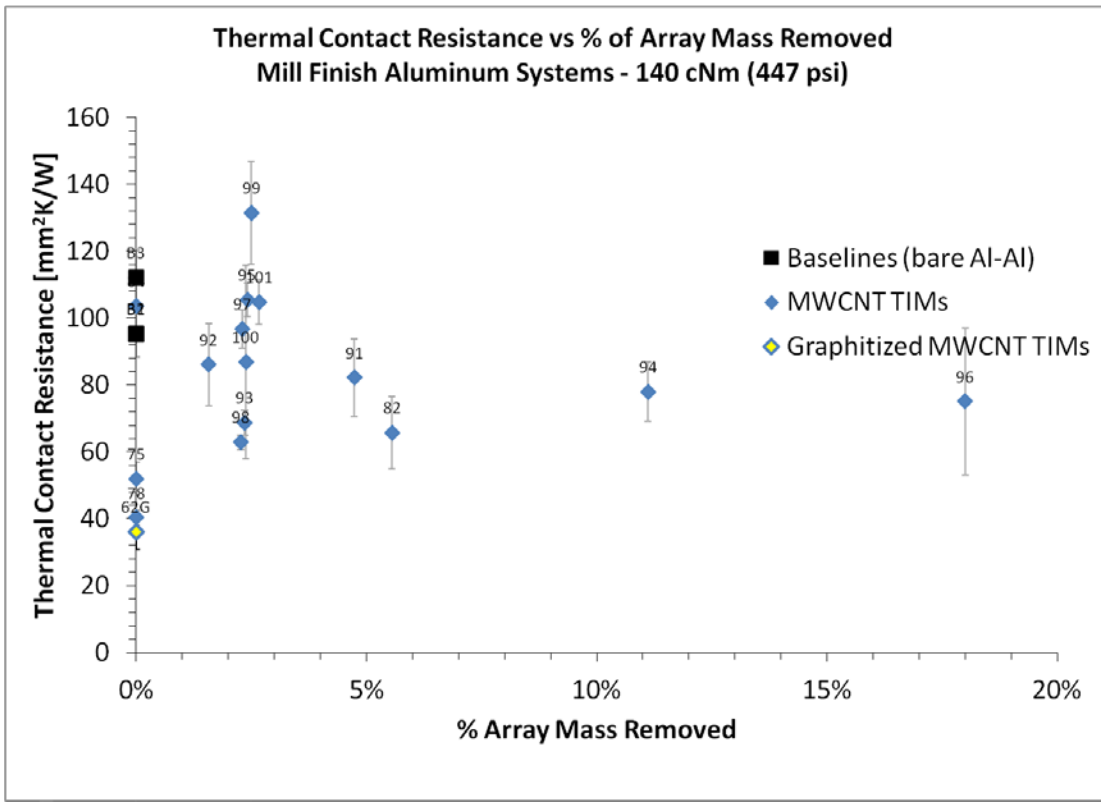

Figure 2-17 - Contact Resistance vs. % Array Mass Removed - Mill Finish Al, 140 cNm (447 psi)

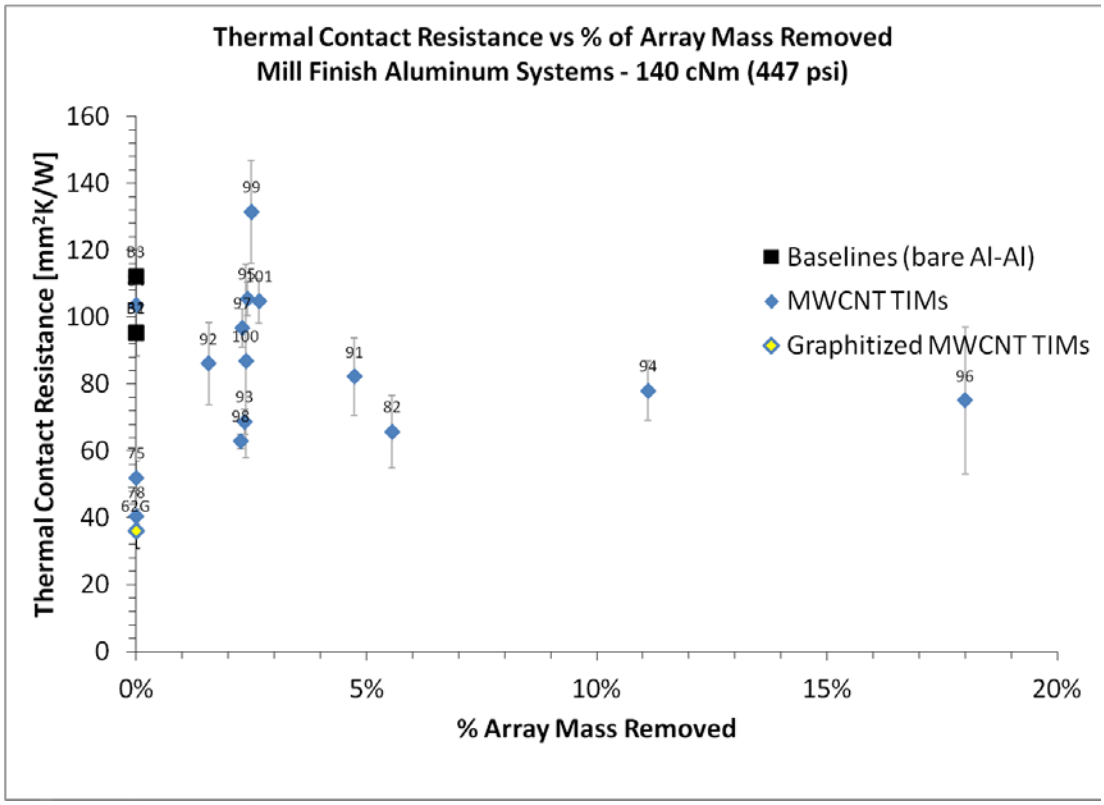

Figure 2-17 shows there is no readily apparent trend between the percent of array mass

removed and improved thermal performance. It is assumed any removed mass belonged to amorphous carbon. There can be several explanations for this with extremes ranging from arrays that did not have a significant layer of amorphous carbon to remove, to arrays that did have layers of amorphous carbon to remove, but it was too entrained in the array to be effectively vacuumed away. The latter is true of array #96, which is actually one of the thinnest arrays tested at 38.2 micron thick. It has a layer of amorphous carbon extending nearly 20% of the total array thickness, as shown in Figure 2-18 below.

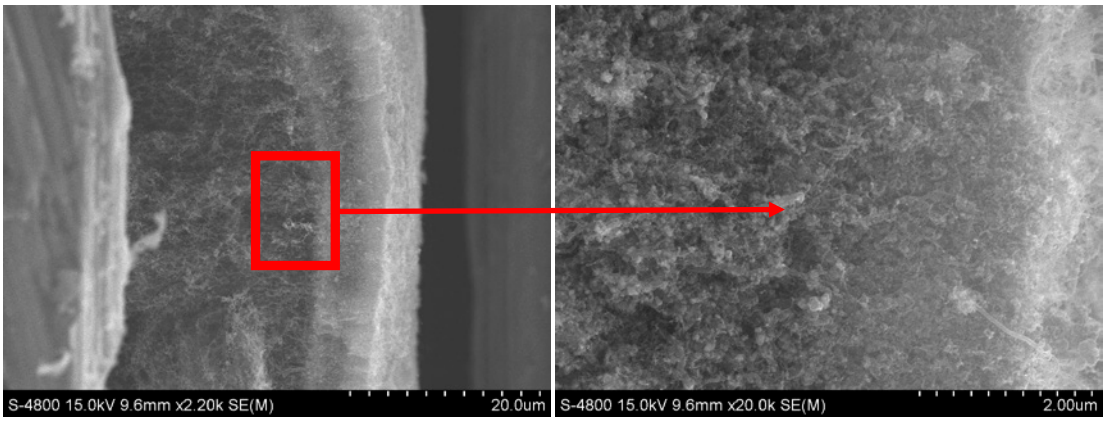

Figure 2-18 – SEM images showing amorphous carbon layer of Array 96

2.3.1.6 High Contact Pressure LFA Results Conclusion

The preceding sections discussed the physical properties of aligned MWCNT arrays which influence their performance as a TIM. Based on the spread of baseline points in the data, any conclusions which could be drawn about thermal performance gains from aligned MWCNT array TIMs would be dubious at best. There is simply not enough contrast between the baseline and MWCNT array TIM data in high contact pressure aluminum systems to prove that carbon nanotube arrays provide a clear and consistent improvement over the baseline systems.

Ignoring the baseline data points for a moment and focusing on the differences in performance between each array has yielded a glimpse into the world of an aligned MWCNT array TIM. Rough trends point toward high performing arrays possessing low thickness, high bulk density and packing fraction, and clean surfaces. Next, focus will shift to a follow-up study involving low pressure/high roughness systems. The goal of this study has been to see if a clear contrast between baseline and experimental data can be found at lower assembly pressures. The hypothesis for this study is similar to the high pressure systems in that it is expected that high

density/packing fraction arrays with low thickness and clean surfaces will perform well. Additionally, it is expected that a system with high roughness will yield more substantive results.

2.3.2 Low Contact Pressure LFA Results

Low contact pressure tests were conducted at contact pressures ranging from 0 psi to 75 psi, as incremented from 0 in-lb (sample sitting in holder without compression) to 4 in-lb of torque by a Stanley PROTO torque driver. All tests were conducted with Aluminum substrates with the same nominal 14 mm outer diameter and 3.125mm thickness as the high pressure tests. Substrates were sanded to a 60-grit finish (R_A=1.25 μm) in order to introduce surface roughness. As with the high contact pressure systems, the physical properties of arrays tested in low contact pressure systems and their thermal performance is included in Appendix B. Some representative charts will be discussed in the upcoming sections for brevity. Figure 2-19 below shows all data for measured thermal diffusivity as a function of torque applied to the Netzsch high compression LFA sample holder. The chart legend shows baseline aluminum with bare 60 grit surface finish interfaces, as well as selected top performers from the array set. This chart also shows some array TIM and baseline data points which extend into the high pressure regime. Based on this chart it would appear that a point of total saturation has not yet been reached, if it does exist. However, common sense dictates that the incremental gains in thermal diffusivity should diminish as the parent material diffusivity value is approached.

The most important lesson from this chart is that TIMs greatly improve thermal performance at torques as light as 1 in-lb. The exact pressure values corresponding to 1 and 2 in-lb of torque are unknown, but are assumed to be less than the pressure associated with 3 in-lb of torque (33 psi) based on low pressure extrapolation of Netzsch's compression curve discussed previously. Torques beyond 1 in-lb continue to provide increased thermal contact and better TIM performance, but the applied pressure quickly elevates beyond maximum design tolerances of many commercial interface systems (usually less than 100 psi [63]) after 4 in-lb of torque (approximately 75 psi).

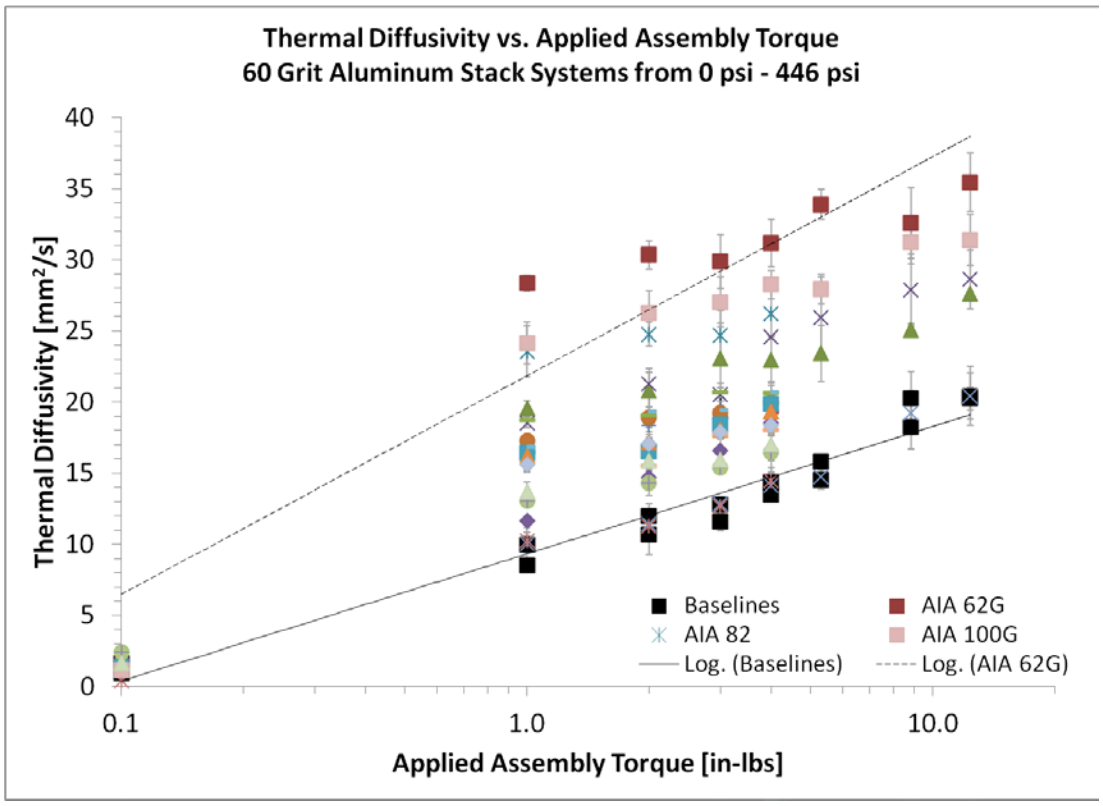

Figure 2-19 - Diffusivity vs. Increasing Contact Pressure

To examine the relationship between Thermal Diffusivity and Thermal Contact Resistance in low contact pressure systems, Figure 2-20 below shows data from tests conducted at 2 in-lb of torque. The same relation found in high contact pressure systems where decreased thermal contact resistance results in higher thermal diffusivity values can be seen here. Thermal diffusivity values approaching 30 mm^2/s are achieved by two of the three graphitized arrays tested in this series, with as-produced arrays trailing not too far behind them. This indicates that the aligned MWCNT array TIMs are able to bridge the gaps between the 60 grit aluminum surfaces more completely than bare interfaces alone.

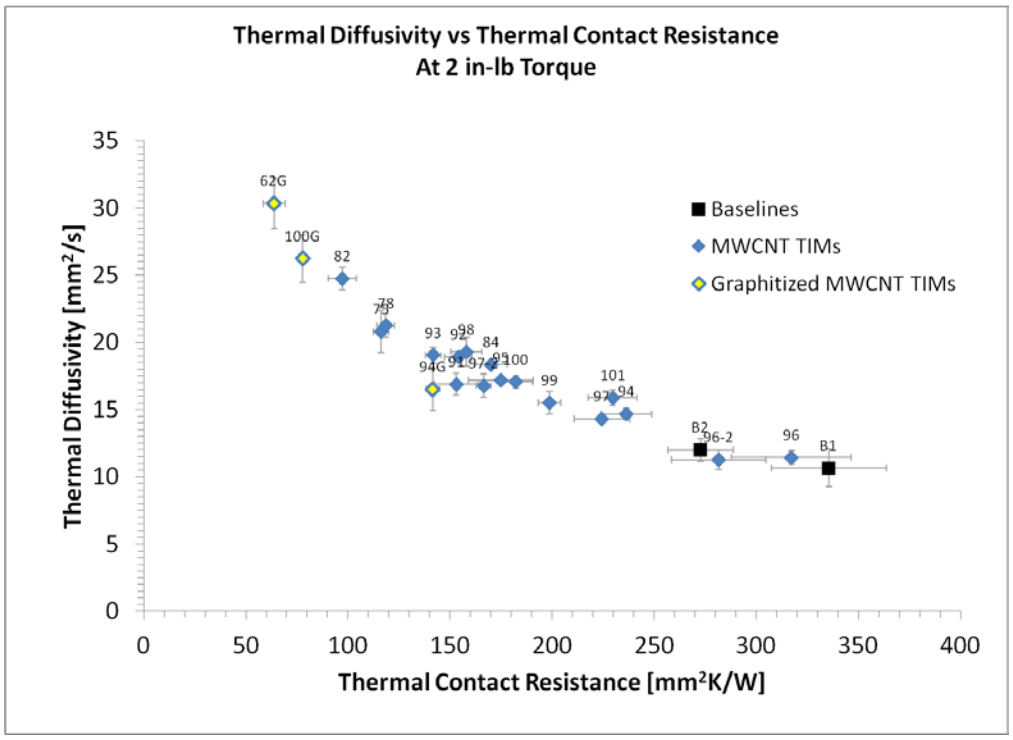

Figure 2-20 - Diffusivity vs. Contact Resistance of 60 Grit Aluminum at 2 in-lb Torque

2.3.2.1 Effect of MWCNT Thickness on Thermal Performance at Low Contact Pressures

Figure 2-21 below shows thermal contact resistance vs. MWCNT Thickness in 60 grit aluminum systems at 2 in-lb of torque. If this chart were accepted at face value, one could mistakenly believe that increased array length leads to lower thermal contact resistance. This is exactly opposite of what should happen in a good TIM system.

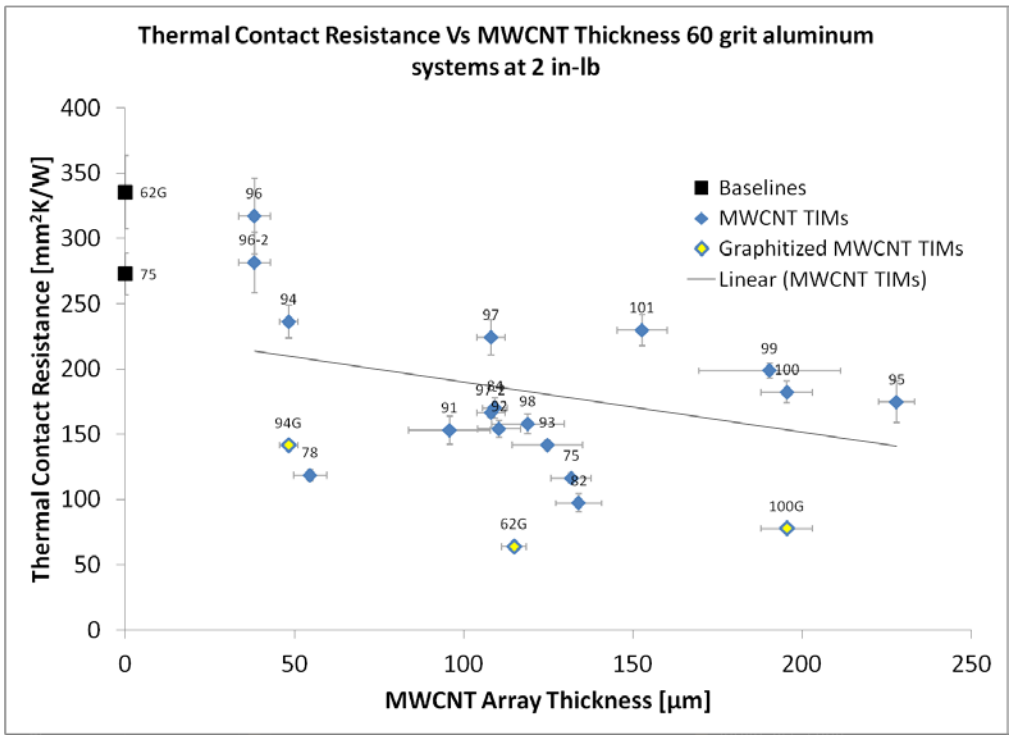

Figure 2-21 - Contact Resistance vs. Array Thickness in 60 Grit Aluminum at 2 in-lb Torque

Accepting samples 96, 96-2, and 94 as outliers allows the rough trend to fall into line with accepted fact. This is illustrated by Figure 2-23 below. These three samples were chosen as outliers even though they represent the two thinnest arrays that have been tested. This decision was based on post-testing imaging of samples in the cases of array 96 and 96-2, and SEM imaging in the case of array 94. Figure 2-22 below contains these images.

Figure 2-22 - Array 96, 96-2, and 94 (from Left to Right)

Both samples of array 96 had large damaged portions from the rough aluminum surface. This led to poor thermal contact and performance, despite low thickness. Also, as shown earlier in Figure 2-18, array 96 has an extensive amorphous carbon layer throughout 20% of its total

thickness. In the case of array 94, this array exhibited very patchy characteristics on one side (left in image), leading to large portions of the array never making complete contact.

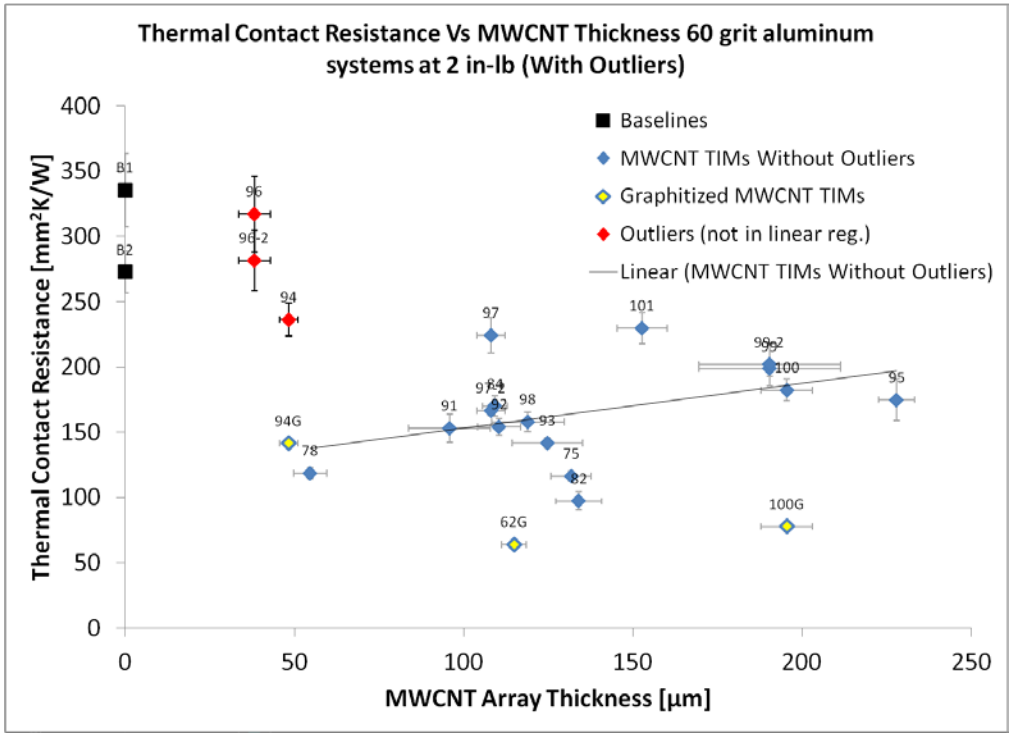

Figure 2-23 - Contact Resistance vs. Array Thickness, 60 Grit Al, 2 in-lb Torque (With Outliers)

2.3.2.2 Effect of Packing Fraction on Thermal Performance at Low Contact Pressures

Examining volumetric packing fraction at low pressures reveals the same trend that was seen in high contact pressure systems. Namely, as packing fraction increases, thermal performance will increase. This is shown in Figure 2-25 below as a decrease in thermal contact resistance corresponding to increased packing.

Here again, samples of array 96 are showing up as outliers due to the large amount of array which is destroyed during assembly by the 60 grit aluminum surfaces. Array samples 75 and 82 are two of the better performing "as-produced" MWCNT array TIMs, and appear to be "desireable outliers" in this case. They are performing better than many arrays in the lower packing fraction range, which can be attributed to their relative surface cleanliness as seen in Figure 2-24 below.

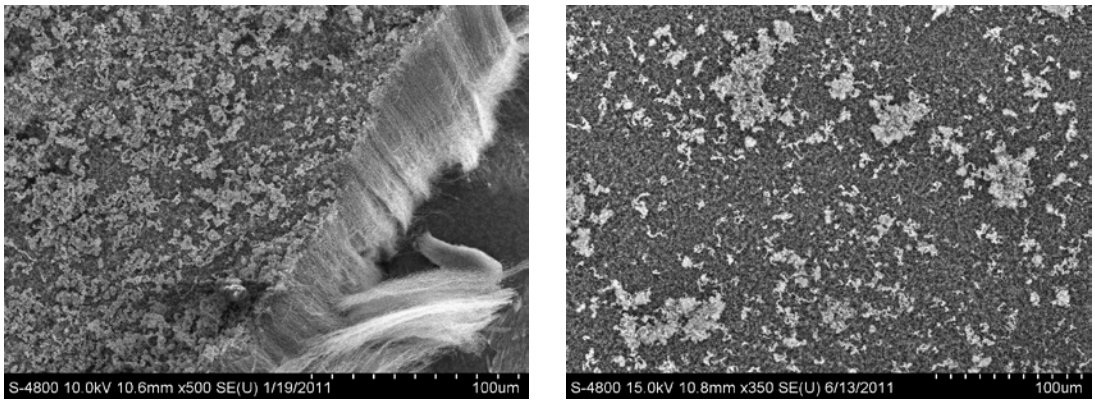

Figure 2-24 - Surface Cleanliness of Array 75 (left) and Array 82 (right)

Array 75 and 82 both lack a large, entrained, amorphous carbon layer. Instead, they possess a small amount just on the surface alone. It is much easier for nanotubes to work around a small layer of the insulating and highly resistive amorphous carbon like those shown here, instead of the thick layers present in array 96.

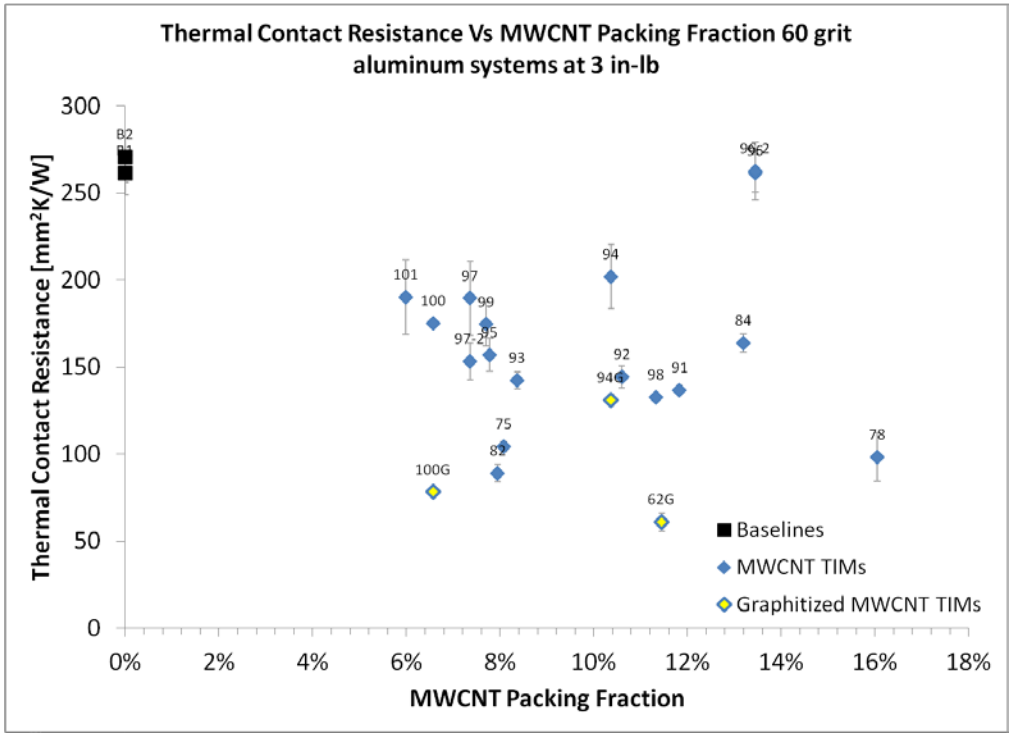

Figure 2-25 - Contact Resistance vs. Packing Fraction in 60 Grit Al at 3 in-lb Torque

2.3.2.3 Effect of Areal Density on Thermal Performance at Low Contact Pressures

The effect of areal density on thermal performance of aligned MWCNT array TIMs is slightly more defined at lower contact pressures than it was at high contact pressure. As shown in Figure 2-26 below, measured data suggests that increased areal density (i.e. more nanotube mass on the substrate slide) leads to decreased thermal contact resistances.

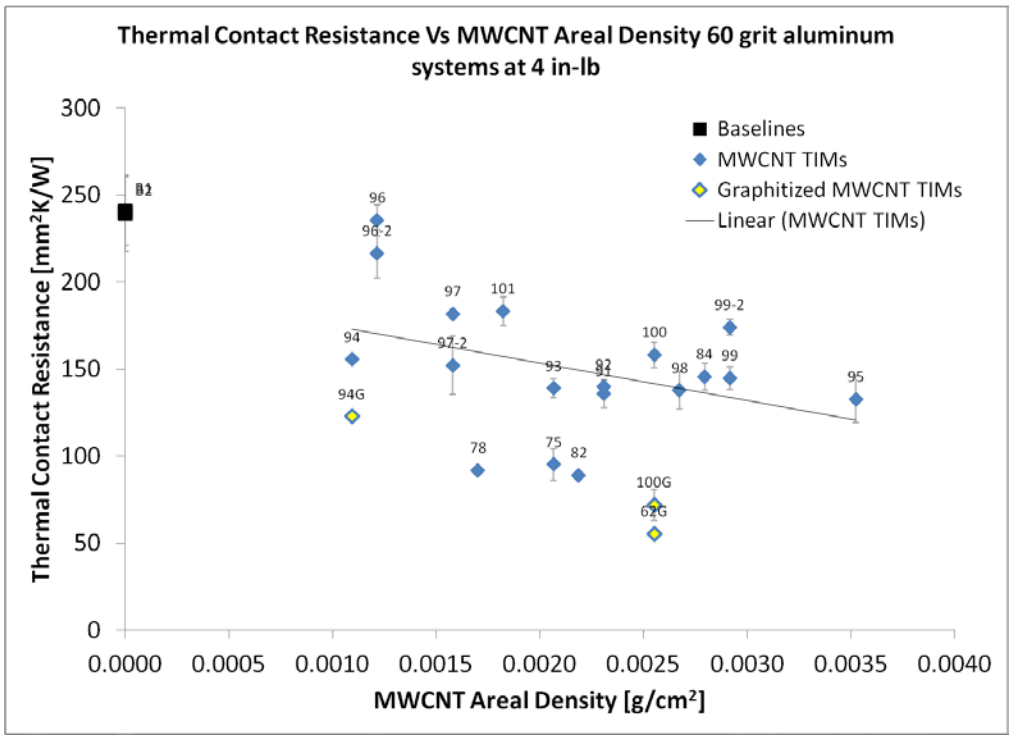

Figure 2-26 - Contact Resistance vs. Areal Density - 60 Grit Al at 4 in-lb Torque

Initially, this loose trend seems to make sense. However, it is difficult to make solid conclusions about the effects of areal density in the case of materials such as carbon nanotube arrays. This is because it is difficult to tell whether the increased mass is due to an increase in the packing factor (e.g. more short tubes, packed closer together) or an increase in thickness (potentially less tubes, occupying less space). Once the remaining factors have discussed, deconvoluting these two factors will be attempted.

2.3.2.4 Effect of Bulk Density on Thermal Performance at Low Contact Pressures

Considering the relationship between array bulk density at low contact pressures and thermal performance yields a very tight group of points. Again, both samples of array 96 are significant outliers due to their large amorphous carbon layer and their tendency to be destroyed by the

rough substrates. Based on the data, a clear trend exists here indicating that increased bulk density leads to lower thermal contact resistances; and results in higher overall thermal performance. The data, labeling samples from array 96 as outliers, is presented in Figure 2-27 below with a linear trend line illustrating the observed trend. Additionally, as with the areal density results, these results must also be carefully considered due to the interplay between bulk density, thickness, and packing factor, which will be addressed shortly.

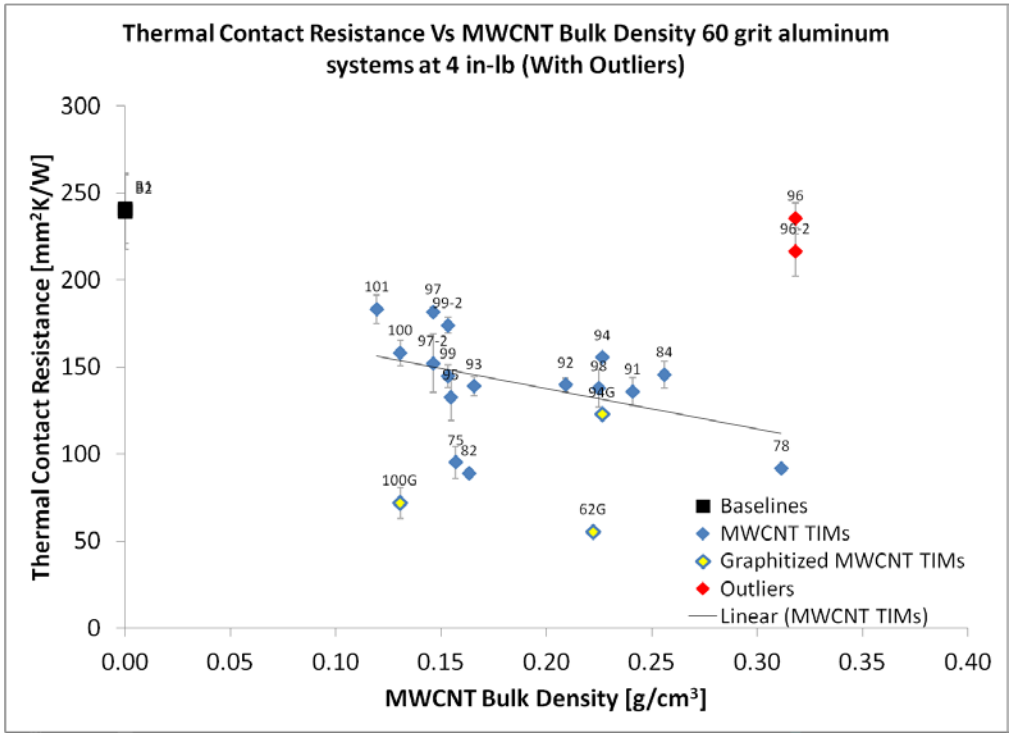

Figure 2-27 - Contact Resistance vs. Bulk Density - 60 Grit Al at 4 in-lb Torque

2.3.2.5 Effect of Array Cleanliness on Thermal Performance at Low Contact Pressures

The idea of array cleanliness is difficult to measure quantitatively. No real trend was seen from the high contact pressure measurements, and that result persists in the low contact pressure regime as well. When studying array cleanliness as amorphous carbon mass removed by vacuum cleaning, array 96's low thermal performance gives the false impression of a trend. This false trend seems to indicate that less mass removed from an array indicates cleaner surfaces prior to vacuuming and better thermal performance. While that idea in itself is logical, one must assume that amorphous carbon exists only on the surfaces of arrays. SEM images of Array 96 presented earlier clearly show this is not a valid assumption, which invalidate the trend.

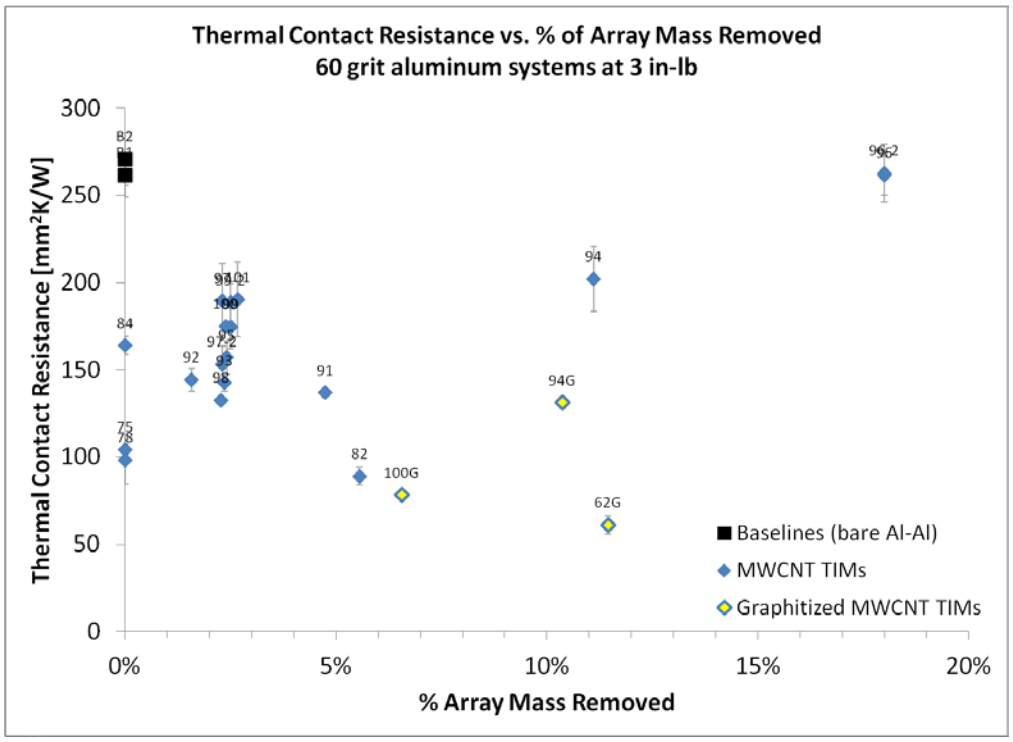

Figure 2-28 - Contact Resistance vs. % Array Mass Removed - 60 Grit Al at 3 in-lb Torque.

2.3.2.6 Low Contact Pressure LFA Results Conclusion

As discussed in the preceding sections, similar trends were seen in both the high contact pressure and low contact pressure aluminum studies. The strongest trends were seen relating thermal performance to bulk density, packing fraction, and MWCNT array thickness. In these systems, the introduction of a 60-grit surface finish substrate helped provide greater contrast between baseline and MWCNT TIM results at low contact pressures. This data provides more confidence in the observed trends. Furthermore, it proves MWCNT array TIM performance over a range of contact pressures more in conformance with commercially and technically realistic assembly pressures.

2.4 Discussion

When examining the thermal response of stacked aluminum systems with aligned MWCNT array TIMs, the most prominent thermal performance trends appeared when examining bulk density, packing fraction, and array thickness. These three features are interconnected in a material such as a carbon nanotube array, as shown in Figure 2-29 below.

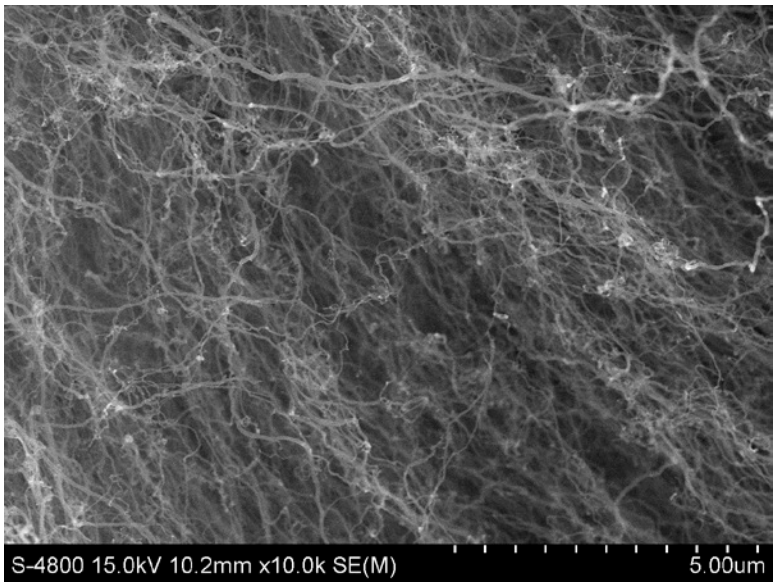

Figure 2-29 - SEM Image of Array 78's Side Profile

The majority of volume inside of a carbon nanotube array is filled by air. The implications of this are counterintuitive for those unfamiliar with these materials. Generally, an aligned MWCNT array is comprised of more than 80% air. This means increases in an array's length must lead to a decrease in the overall packing fraction of the material with increased volume, and thus *decreases* its overall bulk density. This conflicts with macro-scale understandings of density, where increasing the volume of a solid generally incurs a corresponding increase in mass and renders no change in the bulk density.

To better understand this, consider a grass analogy for carbon nanotube arrays. At the roots of the grass, all the plants (carbon nanotubes) are closely packed and highly aligned. As each plant becomes taller, it loses some of its aligned nature, and the top of the patch spreads out from an initial aligned state, leading to decreased packing fraction with increased height.

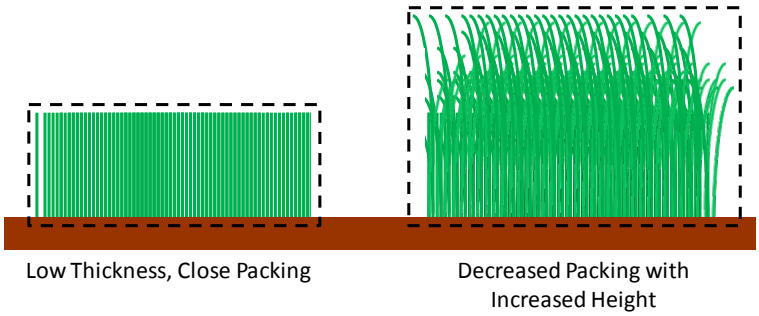

Figure 2-30 - Grass analogy for aligned carbon nanotube arrays

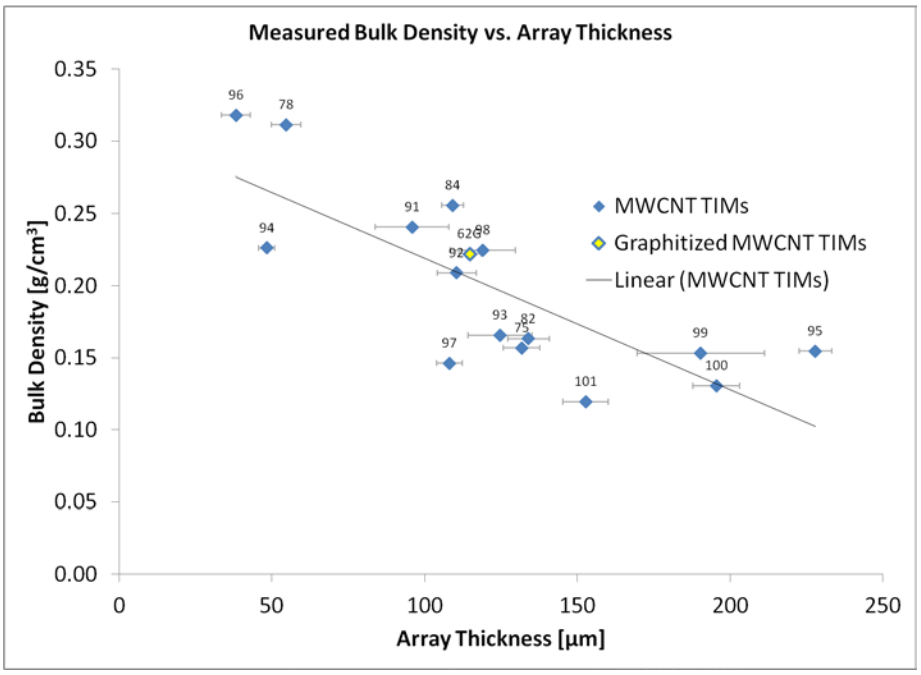

Figure 2-31 - Measured MWCNT Bulk Density vs. Array Thickness

Figure 2-31 shows that decreased array thickness correlates with increased bulk density.

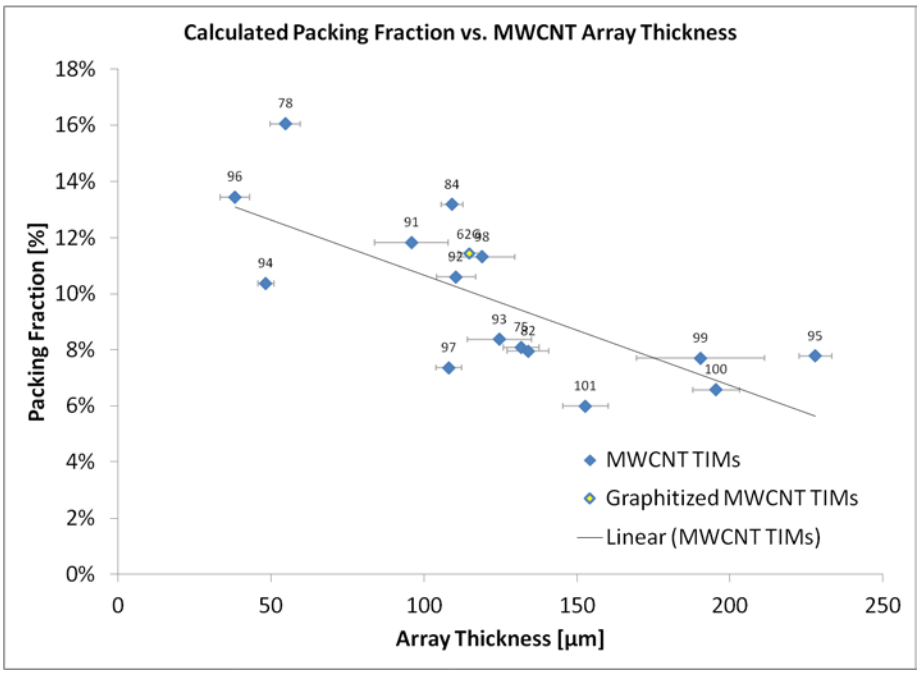

Figure 2-32 - MWCNT Packing Fraction vs. Array Thickness

Again, the same type of trend can be seen correlating packing fraction and array thickness. As thickness decreases, the overall packing fraction increases. Now two trends exist which indicate thinner arrays should be denser and more tightly packed. Assuming perfect arrays with little amorphous carbon content are tested, a denser/tightly packed array means more nanotube tips per area, which should exhibit better thermal performance as an array TIM.

Areal density is the only array property which can be measured prior to harvesting and committing materials and time to their processing. A relationship between areal density and array thickness is presented below in Figure 2-33.

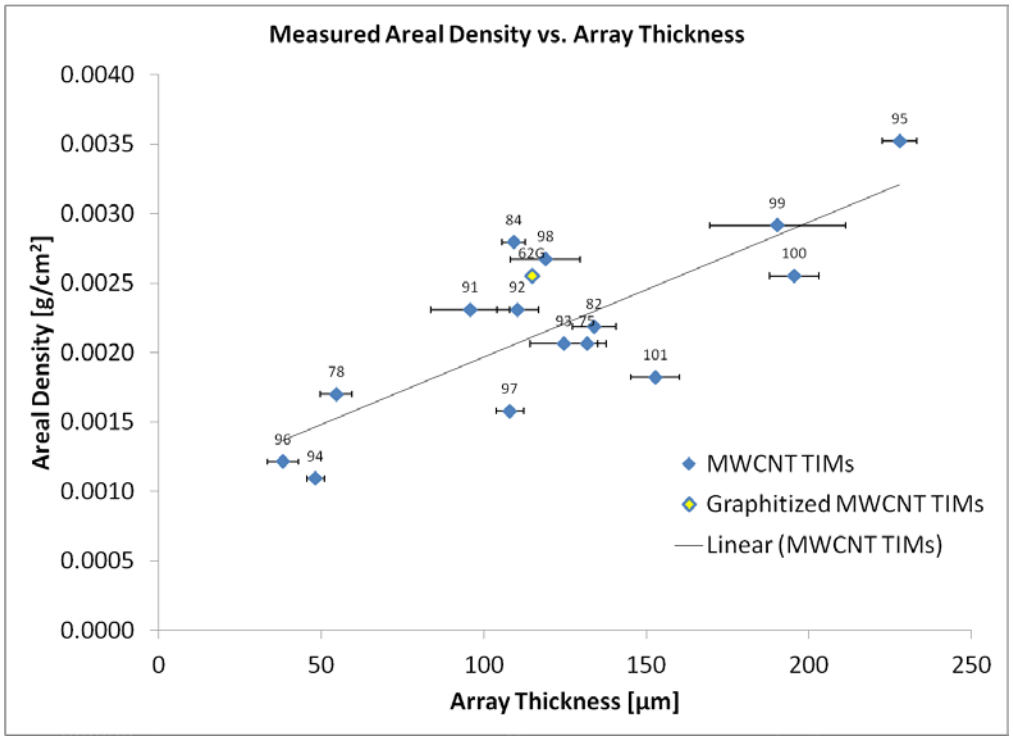

Figure 2-33 - Calculated MWCNT Areal Density vs. Array Thickness

A logical correlation exists between areal density and array thickness. As thickness decreases, there is less overall nanotube mass on the slide and hence, lower areal density. An important correlation also exists between the measured array mass on the slide and thermal diffusivity. This correlation is presented as mass on the slide vs. thermal diffusivity in Figure 2-34 and as the more general areal density vs. thermal diffusivity in Figure 2-35.

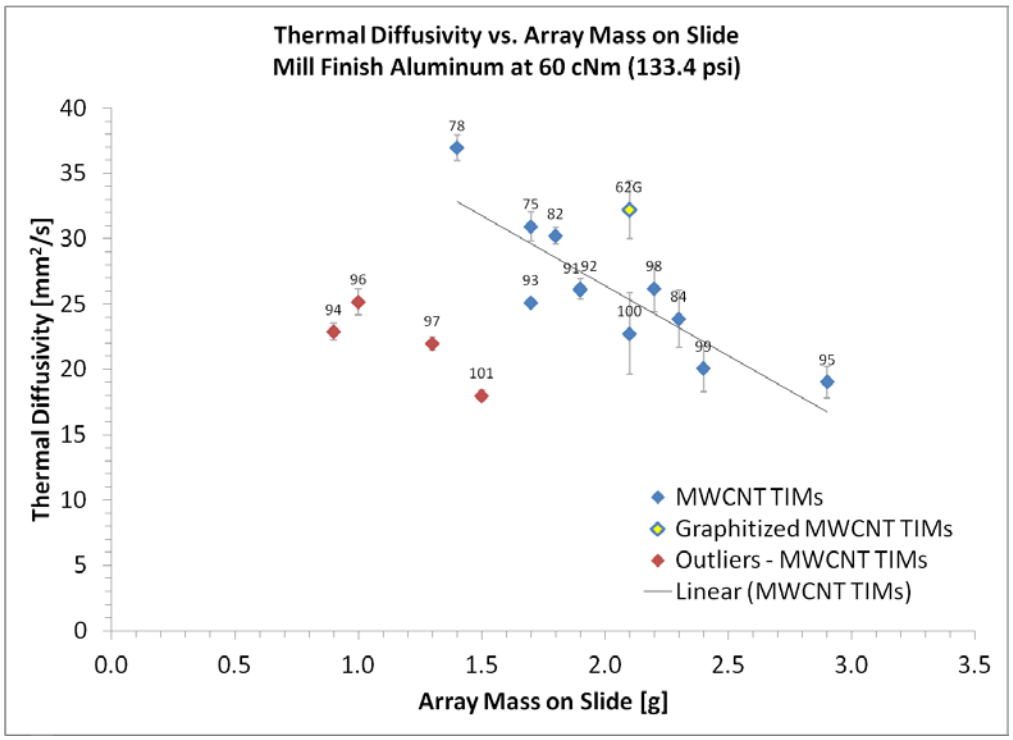

Figure 2-34 – Thermal Diffusivity vs. MWCNT Mass on Slide – Mill Aluminum at 133.4 psi

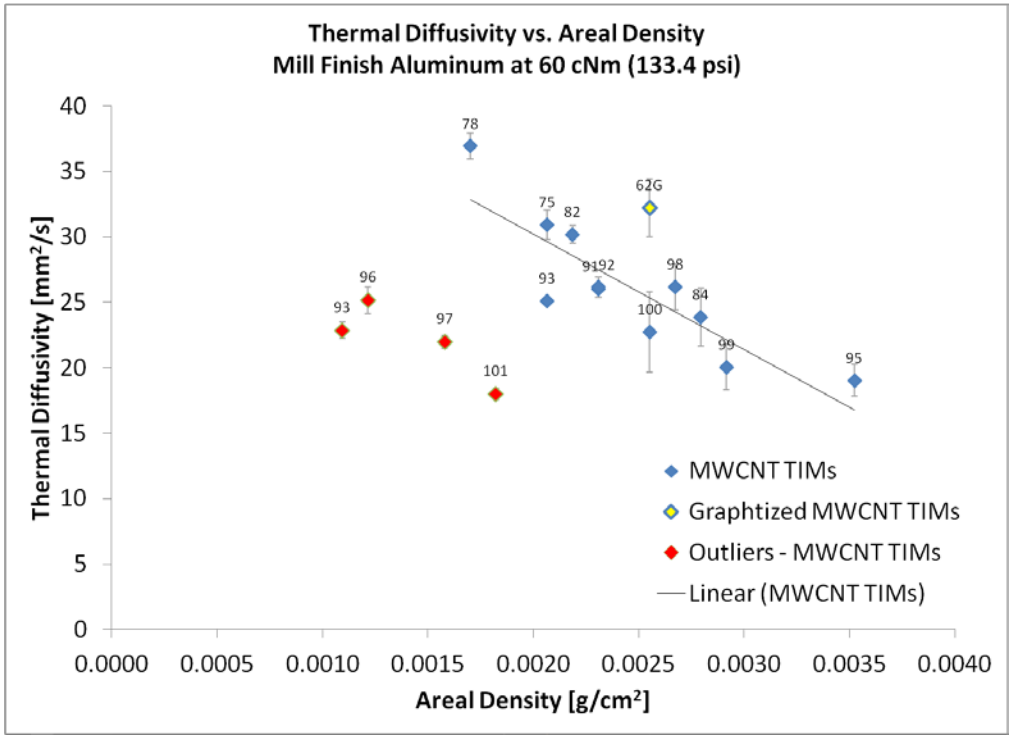

Figure 2-35 - Thermal Diffusivity vs. MWCNT Areal Density - Mill Aluminum at 133.4 psi

Excluding the four outliers, (arrays 94, 96, 97, and 101), reveals a strong and important trend correlating less mass on the slide to increased thermal diffusivity. This trend indicates which MWCNT arrays may be best suited for TIM use before any work is done to characterize them.

It is appropriate to discount the four arrays marked as outliers for differing reasons. Arrays 96 and 94 are the two thinnest arrays of those tested, but array 96 possesses an extensive layer of entrained amorphous carbon, which chokes its thermal performance as seen in Figure 2-18. Array 94 also possesses an extensive layer of amorphous carbon, but has the additional disadvantage of being patchy, where some nanotube tips do not extend across the interface, as shown in Figure 2-22. Array 97 was of medium thickness, but was choked by a layer of cracking amorphous carbon on its surface, seen in Figure 2-36 below. Despite some array curling, array 101 possesses the aligned nature of a top performer as seen in Figure 2-37 below, but is much thicker at 152 micron. It yielded the lowest packing fraction of all arrays tested at 5.99% and has the lowest bulk density to match at 0.119 g/cm^3. These indicate a large amount of air is trapped in this array, and a much lower ratio of conductive carbon nanotube paths is present.

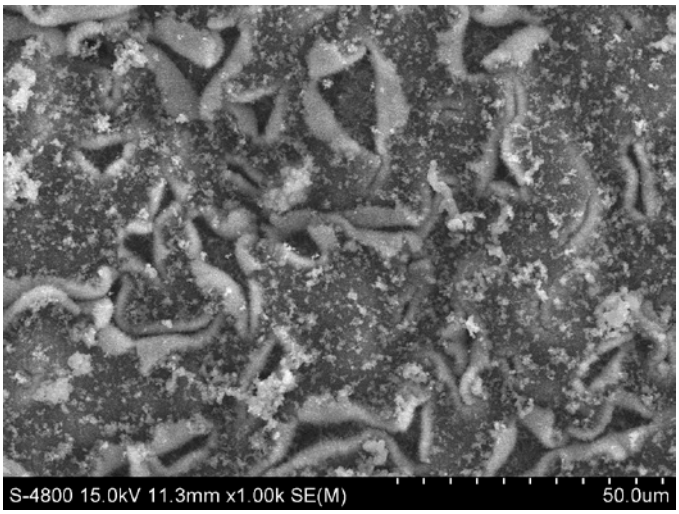

Figure 2-36 - Cracked Amorphous Carbon Layer on Array 97 Surface

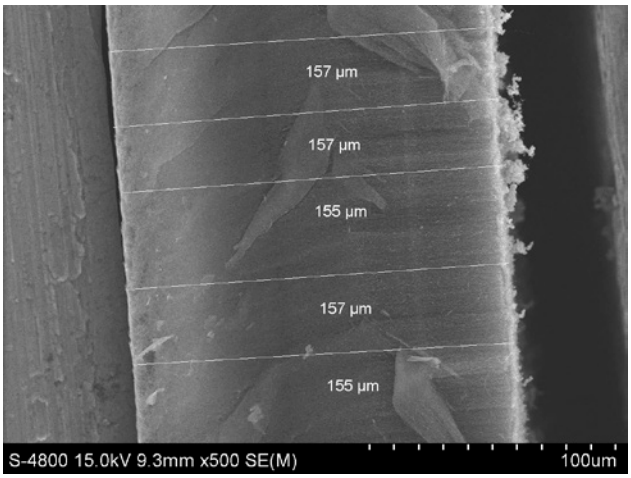

Figure 2-37 - Thickness Profile of Array 101

The top performing array, array 78, is an excellent example of what is desired in a TIM-grade array. It is relatively thin at 54.6 micron, has the highest packing fraction and second highest bulk density of all tested arrays at 16.05% and 0.311 g/cm^3 (respectively), and is relatively clean as shown in the SEM image in Figure 2-38 below.

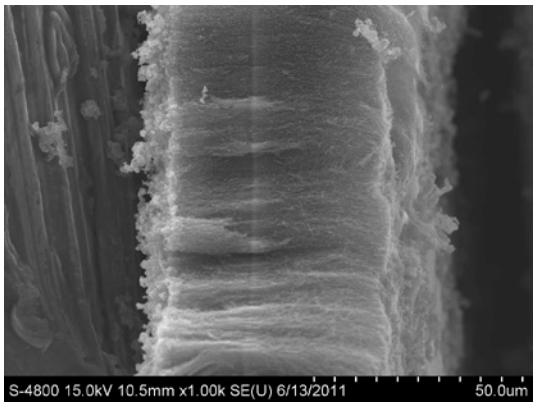

Figure 2-38 - SEM Image, Side Profile of Array 78

While there is a thin layer of amorphous carbon visible on the surface of array 78, it is more important to notice that there is no layer of amorphous carbon embedded in the array's thickness. This allows the array to maintain close packing and a high degree of nanotube alignment.

2.5 Conclusion

At the beginning of this chapter, the stated hypothesis asserted the best performing array TIMs were expected to be thin, to possess high bulk and/or areal densities, to have high volumetric packing fractions, and to be free from amorphous carbon deposits. Based on the work presented in this chapter, it is concluded that the aligned MWCNT arrays best suited for duty as a thermal interface material do possess low thicknesses, high bulk densities and volumetric packing fractions, low masses on the slide, and low levels of amorphous carbon. It is difficult to discern which arrays actually possess these traits based on simple mass measurement. However, data suggests that clean arrays with low areal densities should perform better as a thermal interface material. Additionally, lower bound limits to the trends of low thickness/low areal density providing increased thermal performance must exist, as TIMs must be thick enough to effectively bridge the gaps of a stacked interfacial system. This result can be used in future work to decide which arrays stand the best chance of being exceptional TIM materials.

Chapter 3 Multiwall Carbon Nanotube Arrays as a TIM in Carbon Fiber Composite Systems

3.1 Introduction

In the following work, the effectiveness of aligned MWCNT array TIMs in stacked two layer carbon fiber LFA systems is investigated. The use of carbon fiber in engineered products continues to rise, and with this rise comes the increased chance of a thermal interface having at least one carbon fiber substrate. The focus of this chapter is to examine the effects of contact pressure and array properties on their performance as TIMs in an all carbon fiber composite interface. Based on the results found in Chapter 2, it is hypothesized that aligned MWCNT array TIMs with clean surfaces, high bulk density, high packing fraction, and low thickness will provide the best improvements in thermal performance in carbon fiber interfacial systems.

3.2 Experimental

The LFA substrates used in this chapter are carbon fiber reinforced composite materials, produced in-house with contemporary vacuum bagging and autoclave curing techniques. They are unidirectional (0°) composites, made to 6-ply thickness from aerospace grade carbon fiber prepreg. The composite material was hand laid according to the standard layup diagram used at CAER, shown in Figure 3-1 below.

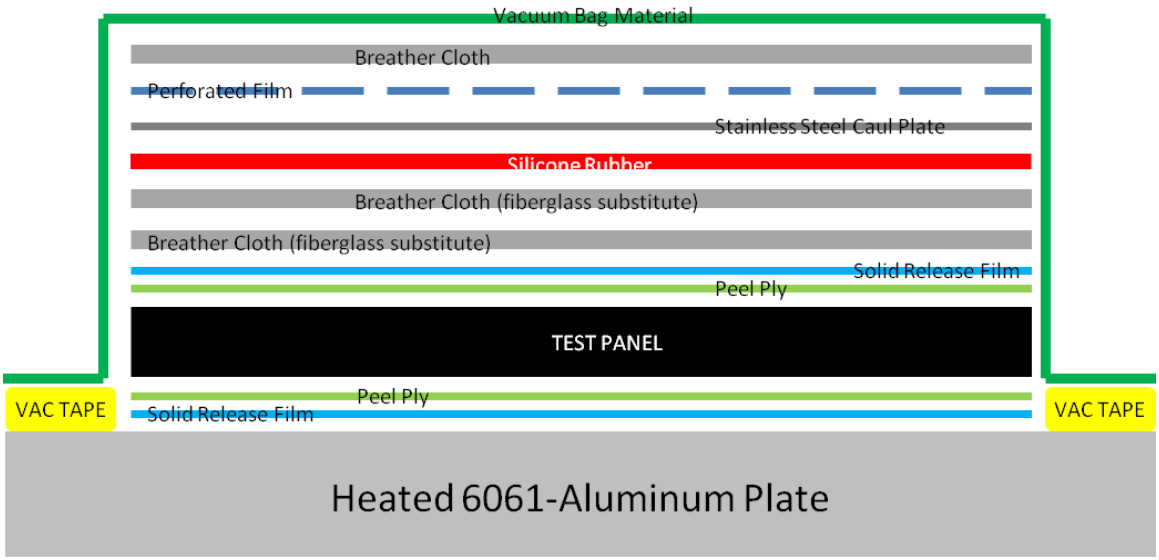

Figure 3-1 – Standard Vacuum Bagging Schematic used at CAER

While all the layers of material used in the vacuum bagging process are important and serve vital roles, the layers of “peel ply” material surrounding the carbon fiber test panel have the most dramatic impact on thermal interfaces. This material is a woven fabric placed on the top and bottom of the composite panel to soak up excess epoxy which is pressed out of the panel under autoclave pressures. As a side effect, the material imparts a uniform surface finish when the fabric is pressed into the top and bottom layer of the prepreg tape. Once the fabric is soaked with epoxy, it appears to bond with the panel, requiring it to be peeled off (hence, the name).

On the macro scale, the imparted surface finish is matte with a smooth texture. Issues appear on the micro scale, as demonstrated by the optical microscopy image in Figure 3-2 below.

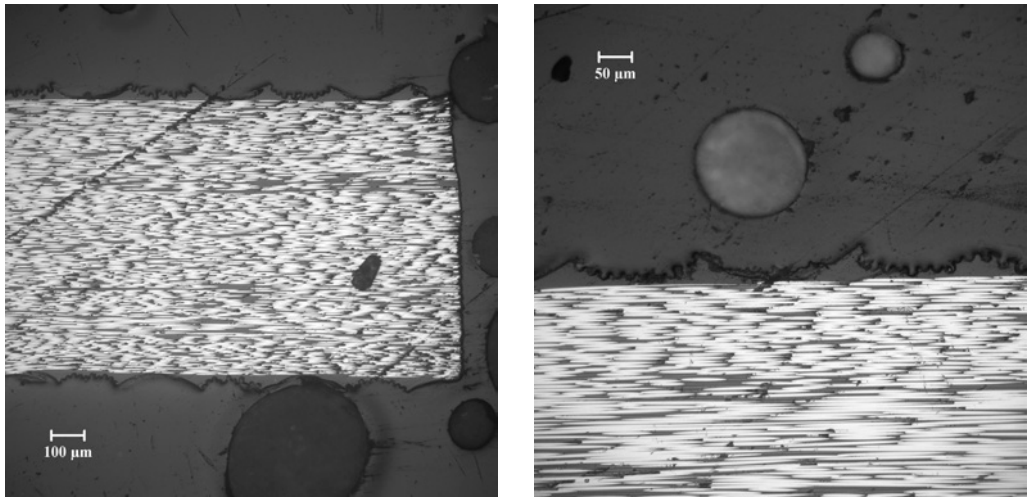

Figure 3-2 - 10x, 20x (Left, Right) Images of 6-ply Composites with Peel Ply Finish

The peel ply fabric leaves a pattern on the top and bottom surfaces of the composite. Not only does a large pattern like a serrated edge appear, but individual fibers from the larger woven bundle leave their own small serrated edge patterns in the valleys between the larger peaks. To complete the description of this surface pattern, it must be recalled that the peel ply fabric is a two dimensional weave. This means that this serrated edge pattern is really a sequence of peaks and valleys in two directions. A surface pattern such as this could potentially have many more “point contact” locations than a machined surface with a regular tool mark pattern. As a consequence of these challenging surface features, an array TIM may actually need to be thicker than desired in order to effectively bridge the gaps created by these peaks.

In addition to physical challenges presented by the peel ply surfaces, more challenges arise when testing these materials with the Netzsch LFA 427 and its programmed modeling software. Recalling the boundary conditions of the LFA method from section 2.2.3, heat flow is assumed to be one dimensional. In order to meet the requirements of this assumption, sample thickness should be sufficiently low and anisotropy must be considered. By definition, a composite material is made of two or more different materials, and therefore has the potential to be significantly anisotropic.

To establish an idea of how anisotropy affects thermal properties in carbon fiber composites, consider the following from ASM Handbook Volume 21: Composites. An IM7/epoxy composite with (±30/0) construction has 5 W/mK, 1.2 W/mK, and 0.6 W/mK conductivities in the longitudinal, transverse, and through-thickness directions (respectively) [64]. This indicates that the composite is predominantly conducting heat along the fiber axes, and that heat is avoiding the highly resistive conduction paths through the epoxy matrix. This is visually explained in Figure 3-3 below, where the yellow represents epoxy matrix, the black represents carbon fibers, and red vectors indicate heat flow propensity (larger arrows mean more heat flow).

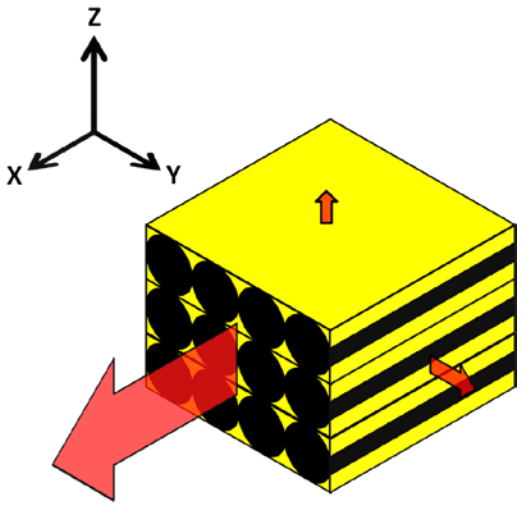

Figure 3-3 - Diagram of Heat Conduction Preferences in Carbon Fiber Composites

With these challenges in mind, testing was conducted in a similar fashion to the aluminum LFA systems of Chapter 2. Initially, it was assumed that having peel ply surfaces stacked together at the sample interface would present problems during LFA testing, so a sanded interface system was created as a potential countermeasure. This interface was constructed by wet sanding one

side of each "as-produced" carbon fiber piece from the LFA substrate set with 500 grit SiC paper. This also set a similar testing stage to the mill and mirror finish stacked aluminum pieces from the previous chapter. High contact pressure testing was conducted for peel ply and sanded sandwich interfaces at assembly torques of 60 cNm, 100 cNm, and 140 cNm (133.4 psi, 290 psi, and 447 psi, respectively). This was followed by low contact pressure testing for both stacked interface styles at assembly torques of 0 in-lb, 1 in-lb, 2 in-lb, 3 in-lb, and 4 in-lb to monitor TIM effectiveness at interface pressures similar to those used in the electronics industry[63]. Initial plans were to conduct “one layer” stack testing for effective thermal diffusivity and “two layer” stack testing for thermal contact resistance across the interface.

Upon analyzing the first few two layer tests, it was found that no reliable measurements could be established for thermal contact resistance. The exact cause of the problem remains unclear, although it is suspected that violations of the underlying model assumptions are the culprit. To remedy this situation, an excel-based iterative calculation method similar to the automated calculations of the LFA software has been developed. Reverse-engineering revealed the algorithm was designed to calculate thermal contact resistance when given substrate properties and an effective one layer diffusivity, and was based on the data reduction methods of J.N. Sweet [56]. This was later confirmed by the original programmer from the software vendor.

This method still relies on the one dimensional heat flow assumption which is likely violated by the carbon fiber material, but it at least returned realistic values for thermal contact resistance. As an accuracy check, over 100 thermal contact resistance values for aluminum systems were calculated and compared to the original thermal contact resistance values calculated by the LFA software. The excel-based calculation overestimated the thermal contact resistance values, averaging 15% error, which is acceptable for a purely mathematical approximation. The values of thermal contact resistance listed in this chapter have been calculated from this excel sheet (unless otherwise noted) and are presented as a method of inter-sample comparison, not as scientific certainty.

3.2.1 High Contact Pressure LFA Results

High contact pressure LFA testing was conducted in the same Netzsch sample holder as the aluminum tests of Chapter 2. TIM physical properties and a complete listing of data used in the charts from this section can be seen in Appendix C, at the end of this work.

Figure 3-4 below shows the general range of diffusivities encountered in carbon fiber composite systems, even under high compression. It is important to note that the diffusivity of the carbon fiber material itself is barely above 0.65 mm^2/s. This indicates just how resistant this material is to through-thickness thermal transport.

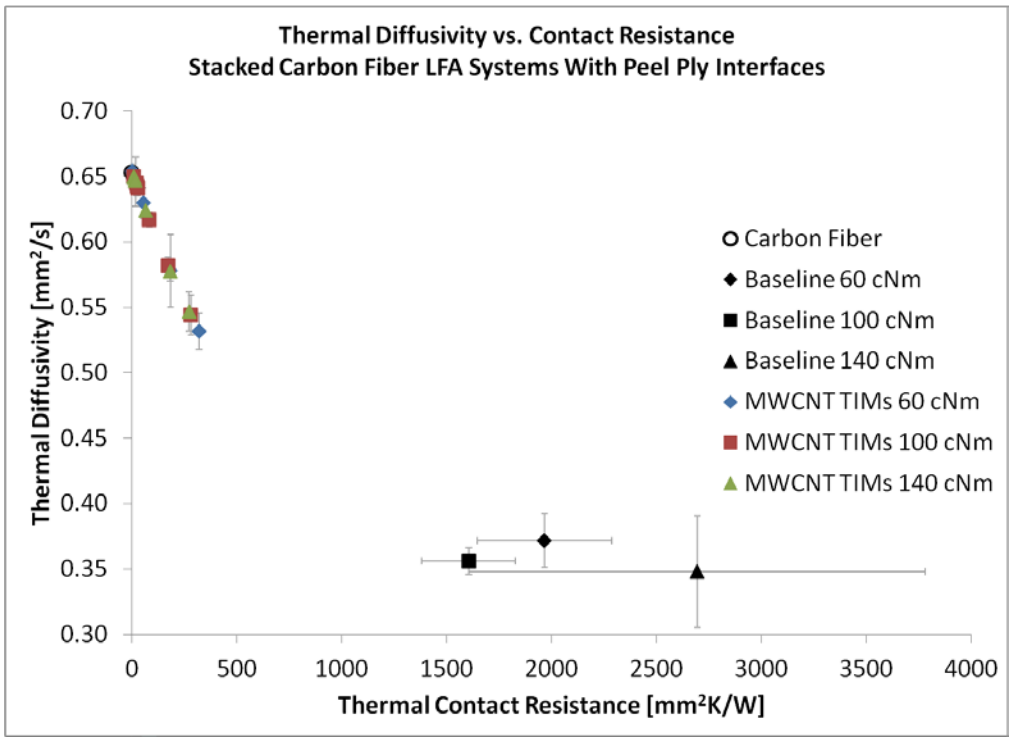

Figure 3-4 - Diffusivity vs. Contact Resistance of Peel Ply Systems at High Pressures

The baseline contact resistance data in Figure 3-4 was calculated by the Netzsch software, and is presented with appropriate standard deviations, as reported by the program. This plot illustrates some of the difficulties encountered when trying to measure contact resistance with any degree of reliability. Neglecting the baseline data for a moment reveals an important feature of the carbon fiber systems, as shown in Figure 3-5 below.

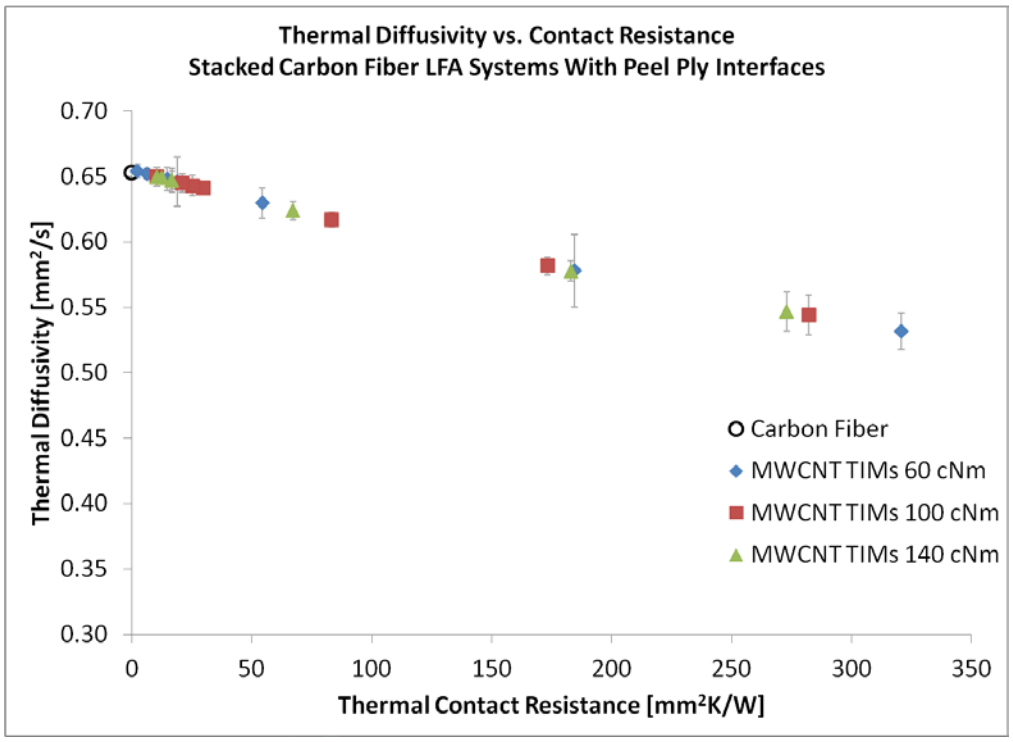

Figure 3-5 - Diffusivity vs. Contact Resistance of Peel Ply Carbon Fiber without Baseline Data

The range of effective diffusivities that can be seen from this graph is very small, from approximately 0.5 mm^2/s to 0.65 mm^2/s. The thermal performance of arrays in carbon fiber systems is independent of contact pressure, as evidenced by the mixing of series throughout the range of diffusivities. The highly linear nature of each series is an artifact of the iterative calculation method used to estimate contact resistances for this material set. This idea of pressure independent thermal performance will be checked for consistency in a later segment of this chapter.

Examining the general thermal performance seen in sanded interface systems reveals even more troublesome findings. Take for example, the thermal performance of array TIMs in sanded interface systems at extreme pressures as shown in figure below.

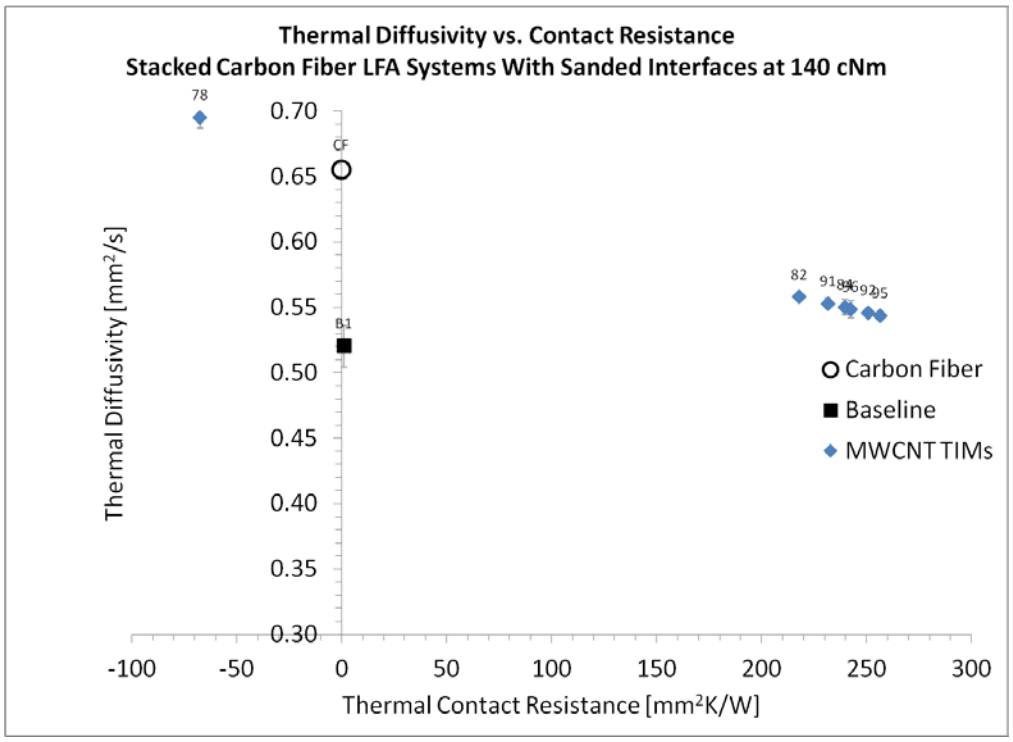

Figure 3-6 - Diffusivity vs. Contact Resistance of Sanded Interface Systems at 140 cNm

There are several noteworthy elements in the figure above. First, it should not be possible for a thermal interface material to improve the effective diffusivity of two identical, stacked materials beyond that of a single material piece. However, this is what has been reported by the LFA 427 with the Cape-Lehman diffusivity model. Secondly, the baseline material reports incredibly low contact resistance values, yet all array TIMs show improved thermal diffusivity with higher contact resistances. Within the array TIM data set (separate from the baseline data) the trend of increased diffusivity with decreased contact resistance is maintained. This could potentially be explained by the smooth surface finish from the sanding allowing a large amount of the constituent carbon fibers to make direct contact across the interface. This would facilitate an even larger longitudinal conductivity at the interface, which would result in extreme radial heat losses and force a smaller measured diffusivity to be reported. A comparison of heat rise curves for the sanded interface baseline system confirms difficulties in accurately measuring contact resistance, as shown in Figure 3-7 below.

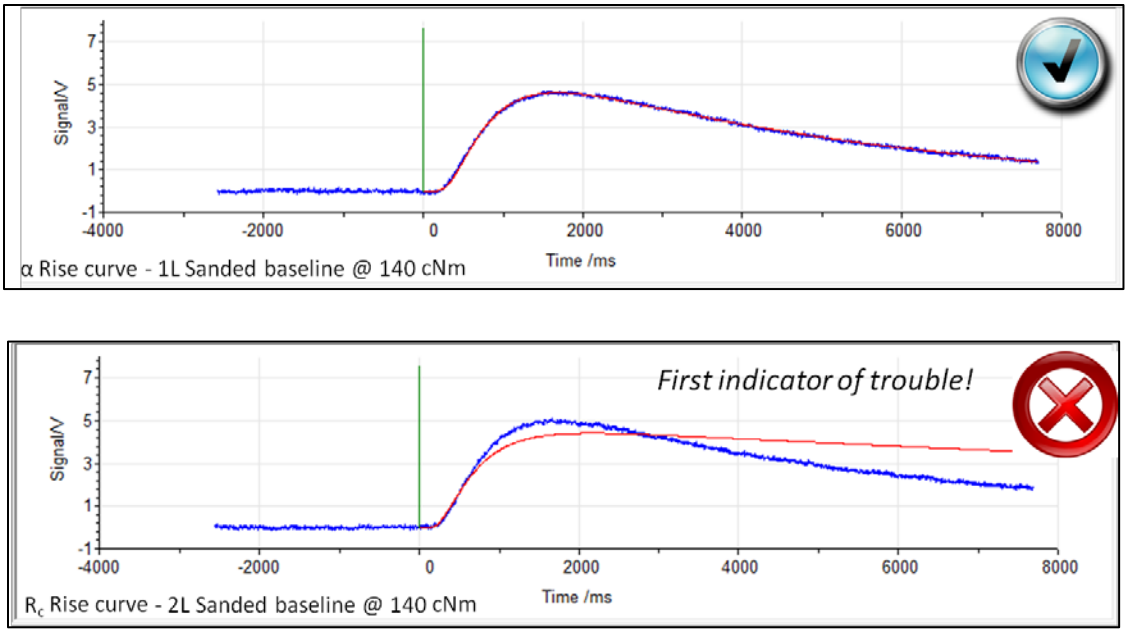

Figure 3-7 - Heat Rise Curves from LFA 427 for Sanded Interface Baseline Measurements

The measured heat rise curve (blue line) for the one layer sanded interface baseline matches the red model curve perfectly. This indicates good agreement with the thermal diffusivity model being applied. The bottom image shows the result of running a two layer test on a sanded interface system. The discrepancy between the blue measurement curve and the red model curve shows that no correction for radial heat losses could be made, and that the calculated value will not match the underlying theory.

Because of the difficulties encountered measuring accurate values from sanded interface systems, the data discussed from this point forward will tend to focus on the more realistic peel ply interface. Unlike the sanded interface system, this interface consistently followed the model curve for its one layer and two layer tests, although it still reported unacceptable standard deviations in thermal contact resistance.

3.2.1.1 Effect of MWCNT Thickness on Thermal Performance

Through calculating contact resistance values, a range of potential thermal performance has been established for peel ply carbon fiber interfaces. It is clear this material is highly resistant to thermal transport through its thickness before any extra interfacial resistance is considered. A reasonable assumption is that array thickness could play an important role in achieving the best possible thermal performance. This idea is investigated in Figure 3-8 below.

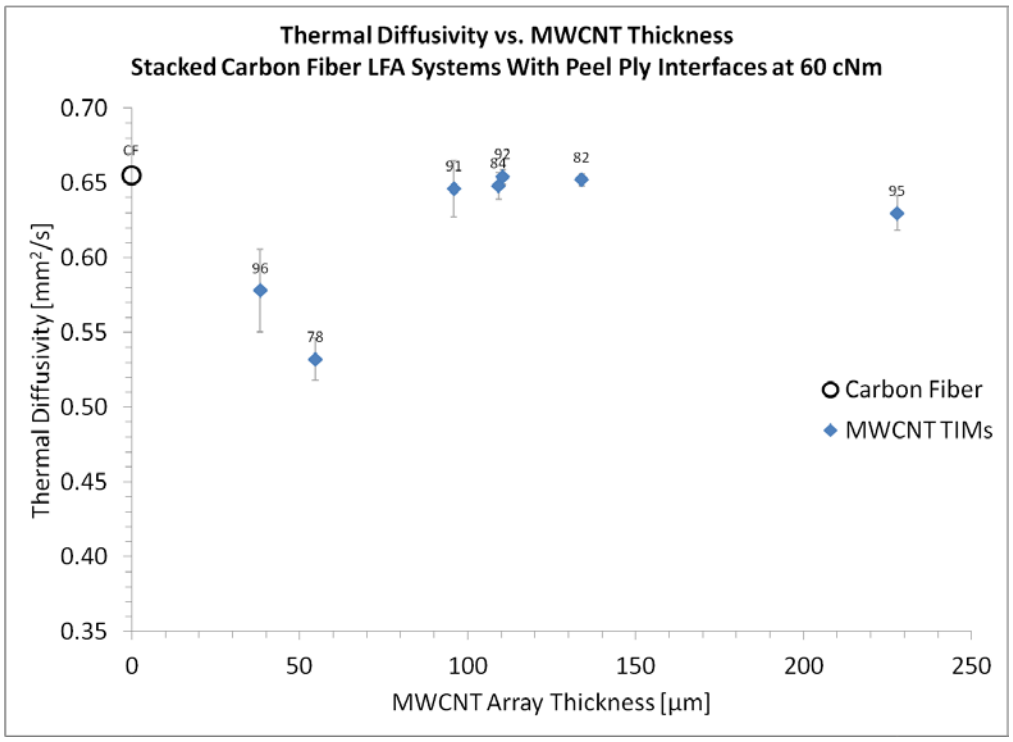

Figure 3-8 - Diffusivity vs. Array Thickness in Peel Ply Systems at 60 cNm

As shown above, arrays which are thicker than 100 micron provide the least hindrance to the overall thermal performance. Array 96 and 78 are two of the thinner arrays which were considered in the carbon fiber systems, as well as the aluminum systems of the previous chapter. In the aluminum systems array 96 returned poor thermal results because of its expansive layer of amorphous carbon, but array 78 was a top performing array. It is possible that array 78 is actually too thin to effectively bridge the large gaps created by the peel ply surface. However, this does not explain the apparent performance similarities between other prior top performers like array 84 and large thickness arrays like array 95. Considering the trends presented in chapter 2, it is counterintuitive that two array TIMs of vastly different thickness should provide essentially equivalent thermal performance. Figure 3-8 indicates that MWCNT array thickness is not the deciding factor in MWCNT array TIM performance. So long as the array is long enough to effectively bridge the gaps produced by joining peel ply surfaces, thermal performance results are nearly identical. This appears to happen at array thicknesses of 100 micron and longer.

3.2.1.2 Effect of Packing Fraction on Thermal Performance

Recalling the conclusions of the previous chapter, it was found that a higher packing fraction tended toward increased thermal performance. Figure 3-9 below investigates the effect of packing fraction on thermal performance in peel ply carbon fiber interfaces.

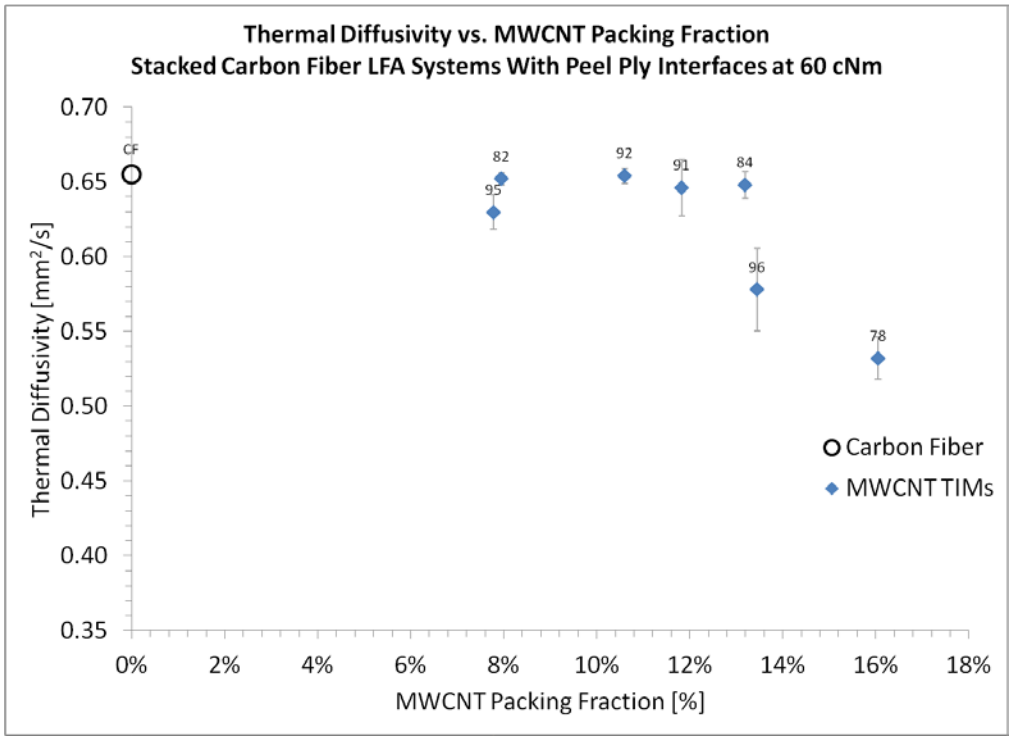

Figure 3-9 - Diffusivity vs. MWCNT Packing Fraction - Peel Ply Systems at 60 cNm

As can be seen above, no real relationship exists between packing fraction and increased thermal performance in peel ply carbon fiber systems at high contact pressures. Array 78 was previously seen as a top performer, but now it returns lower diffusivity values despite having the highest packing fraction of those arrays tested in carbon fiber systems. This seems to refute the trend presented earlier, although with no appreciable differences in thermal performance across various packing fractions, not much is said about a relationship between performance and packing fraction in carbon fiber systems either. It is still possible that array 78 was too thin to effectively bridge the gaps between the substrates. Previously, it was determined that MWCNT array thickness was not an important factor, so long as the arrays could effectively bridge the gap. Here, packing fraction is showing a similar result when recalling that arrays 78 and 96 were likely too thin to effectively bridge the peel ply gap. Based on the longer arrays, packing fraction appears to have no effect on thermal performance in carbon fiber systems.

3.2.1.3 Effect of Areal Density on Thermal Performance

Previously, it was determined that lower areal density (and its readily measured sibling, array mass on the slide) would generally lead to increased thermal performance in aluminum based interface systems. Figure 3-10 below details thermal performance as a function of areal density for carbon fiber based interface systems.

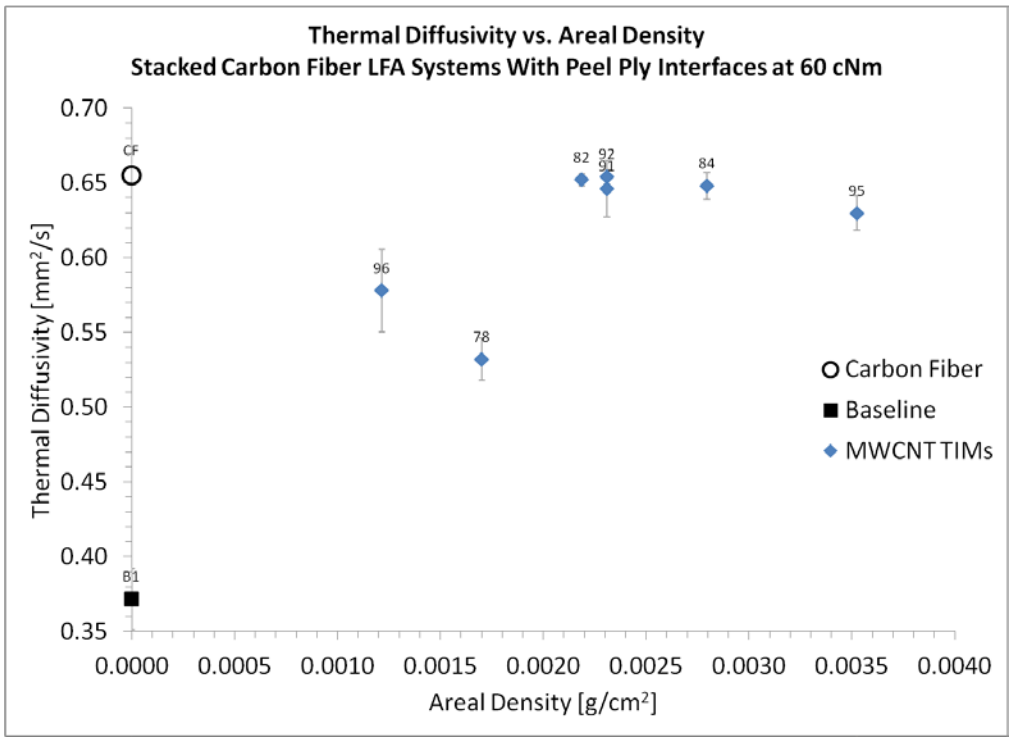

Figure 3-10 - Diffusivity vs. Areal Density of Peel Ply interfaces at 60 cNm

As shown in the figure above, no real trend exists between areal density and array performance in carbon fiber interfaces at high pressures. The chart only suggests that thermal performance is increased through use of an aligned MWCNT array TIM. It does not provide evidence to make distinctions between array performances due to their mass (and thereby implied density or height). Figure 3-11 below shows thermal performance as a function of areal density in sanded interface carbon fiber systems.

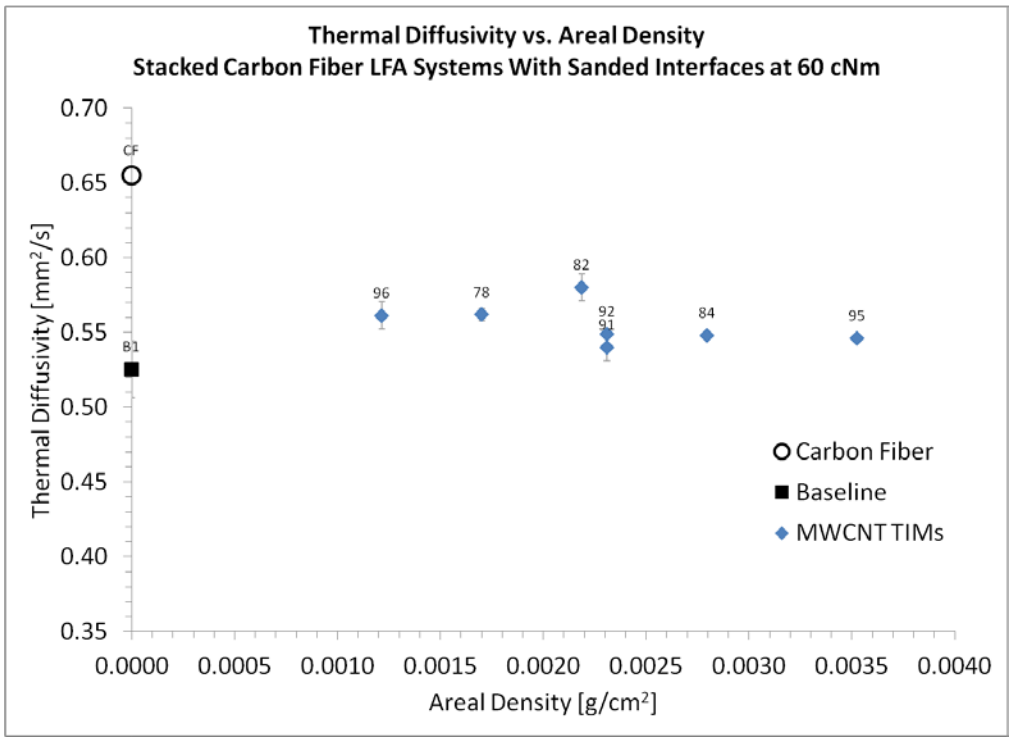

Figure 3-11 - Diffusivity vs. Areal Density of Sanded Carbon Fiber Interfaces at 60 cNm

As shown above, the thermal performance of an array TIM in a sanded interface system is largely independent of areal density. Only modest thermal gains are achieved by most arrays at high contact pressures.

3.2.1.4 Effect of Bulk Density on Thermal Performance

It was previously concluded in Chapter 2 that an array TIM with high bulk density was desirable for improved thermal performance in aluminum based interface systems. Figure 3-12 below examines peel ply carbon fiber interface systems to search for similar trends.

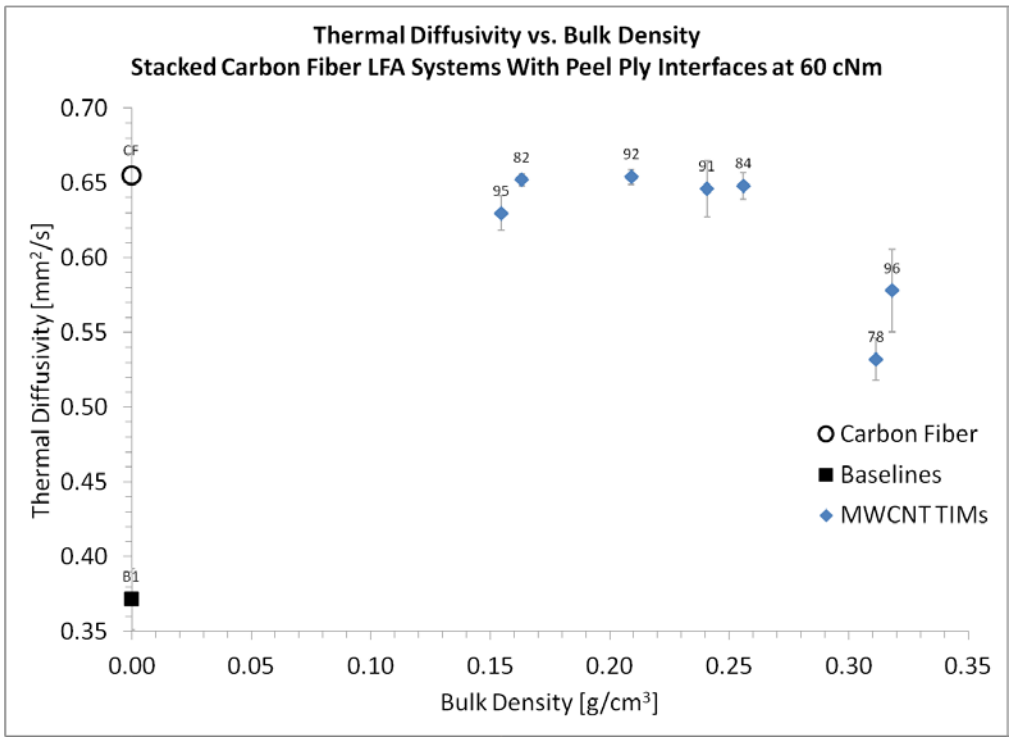

Figure 3-12 - Diffusivity vs. Bulk Density of Peel Ply Systems at 60 cNm

It would seem that the trend established in the previous chapter does not apply to carbon fiber systems. Array 78 was a top performer in those trials, yet it returns the worst performance of all arrays tested here. This chart continues to show array TIM performance yielding an almost constant value regardless of variance in properties. Next, the effect of bulk density on array TIM performance in sanded interface systems is examined in Figure 3-13, below.

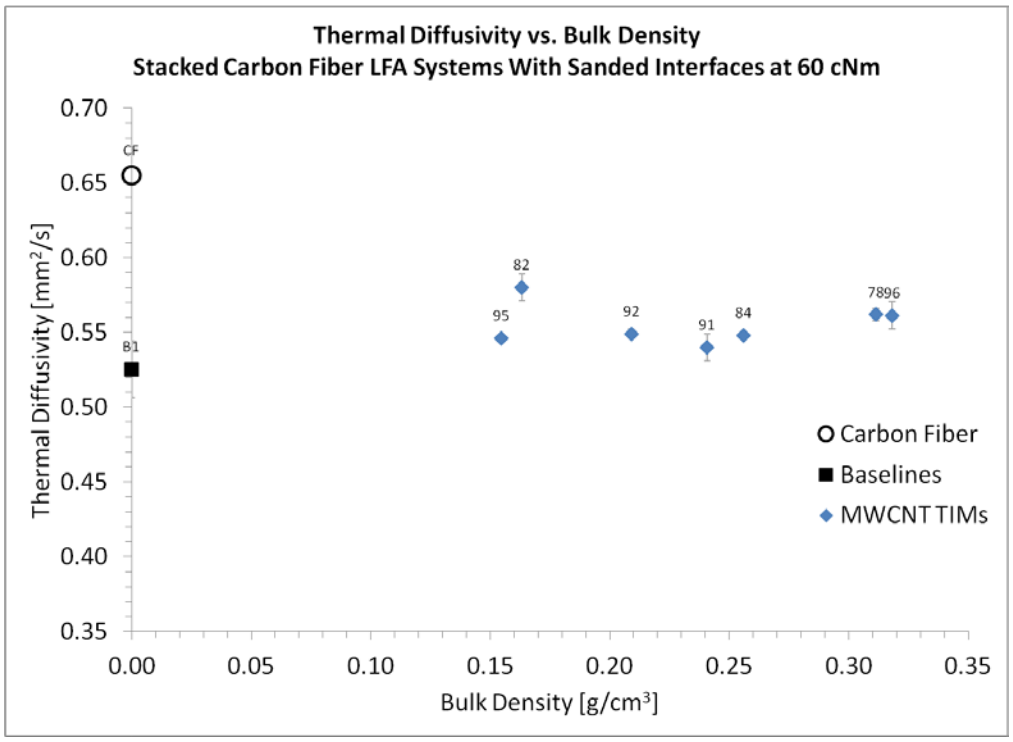

Figure 3-13 - Diffusivity vs. Bulk Density in Sanded Interface Systems at 60 cNm

The effect of bulk density on array TIM thermal performance is even less pronounced in sanded interface carbon fiber systems than it was in peel ply systems. Consistent mild performance increases across the board show no relationship between thermal performance and increasing bulk density in sanded carbon fiber interface systems.

3.2.1.5 Effect of Array Cleanliness on Thermal Performance

Previously, it was determined that array cleanliness is paramount when using aligned MWCNT arrays as TIMs. It was also determined that there was not a well established method of quantifying array cleanliness. Instead, qualitative visual judgment of array cleanliness via SEM imaging was used as the de facto standard for establishing whether one array was cleaner than another. This method continues to be used in carbon fiber interface systems, although the measured mass loss after vacuum cleaning is still investigated for potential results as shown in Figure 3-14 below.

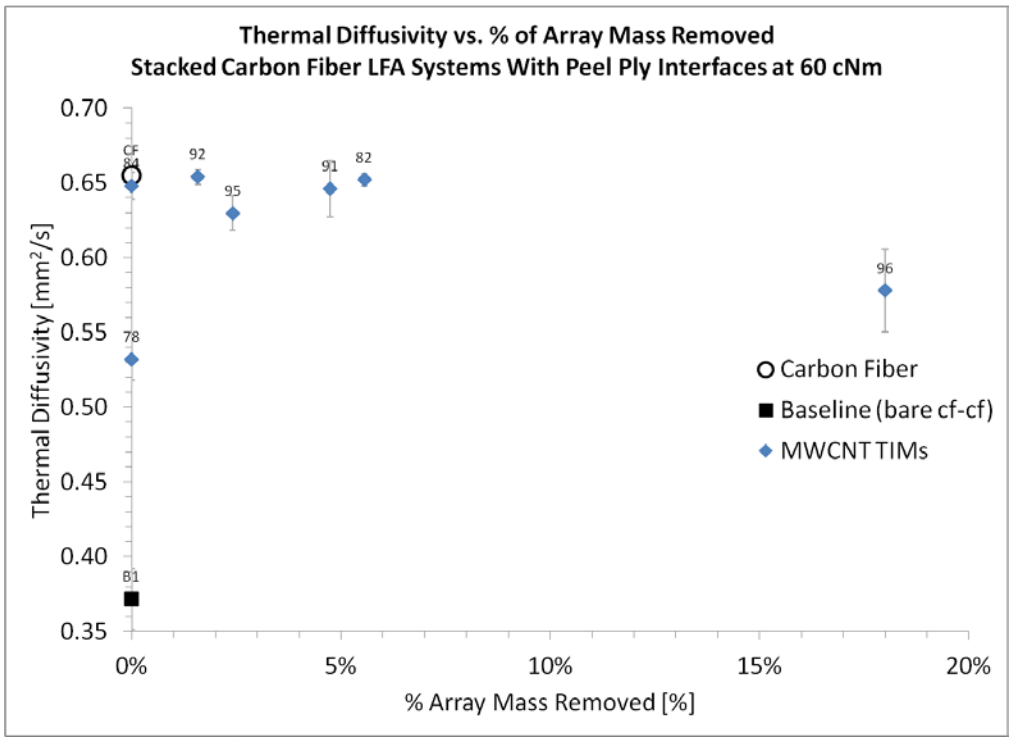

Figure 3-14 - Diffusivity vs. % Array Mass Removed in Peel Ply Systems at 60 cNm

As the chart shows, there is little to suggest measuring the mass loss of an array after vacuum cleaning /prior to harvesting is an effective method for predicting thermal performance of aligned MWCNT array TIMs. Figure 3-15 below shows similar results for the sanded interface systems at high pressures.

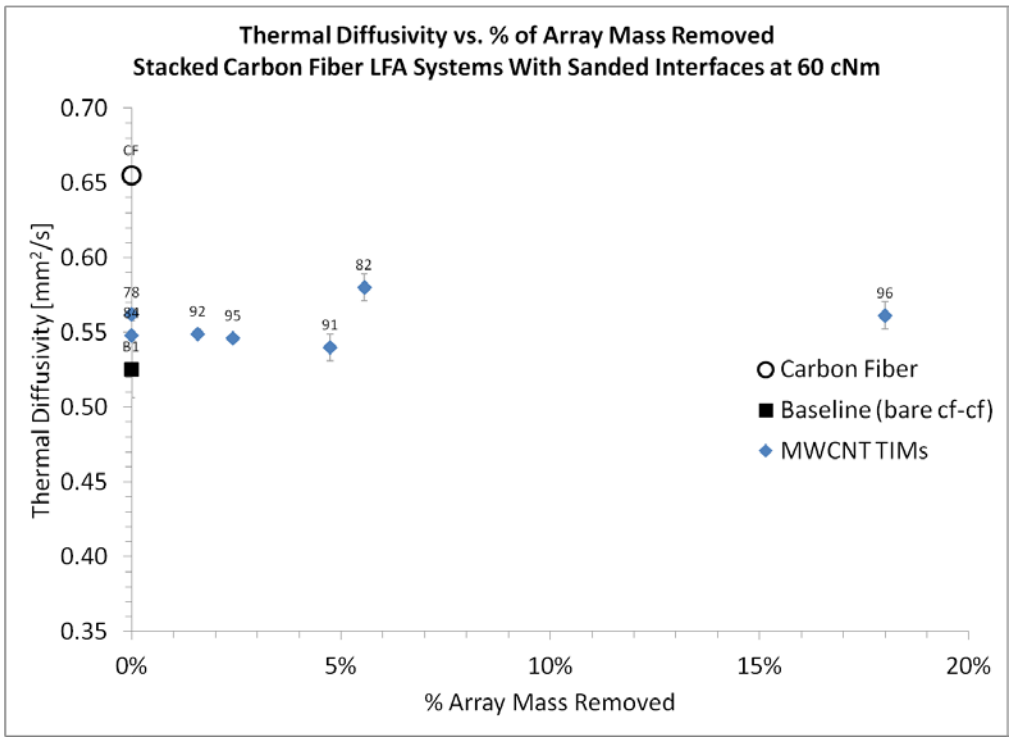

Figure 3-15 - Diffusivity vs. % Array Mass Removed in Sanded Interface Systems at 60 cNm

As can be seen above, the amount of array mass removed by vacuum cleaning prior to harvesting has little effect on the thermal performance of the array in a TIM situation.

3.2.1.6 High Contact Pressure LFA Results Conclusion

Throughout section 3.2.1 the effect of various array properties on their thermal performance in carbon fiber interface systems at high pressure has been presented. A discussion of the material construction and testing assumptions revealed possible ways that carbon fiber composites behave outside the parameters expected in an LFA substrate material. Up to this point, it appears that the properties of the arrays themselves have little effect on the overall thermal performance of a carbon fiber interface system with a TIM. These results suggest that the anisotropic thermal properties of carbon fiber composites need to be addressed before the benefits of a TIM can be leveraged in these systems.

3.2.2 Low Contact Pressure LFA Results

Low contact pressure tests were conducted in the same manner as the low pressure aluminum substrate tests of section 2.3.2. TIM physical properties and a complete listing of data used in the charts from this section can be seen in Appendix D, at the end of this work.

Figure 3-16 and Figure 3-17 detail peel ply and sanded system results at low contact pressures.

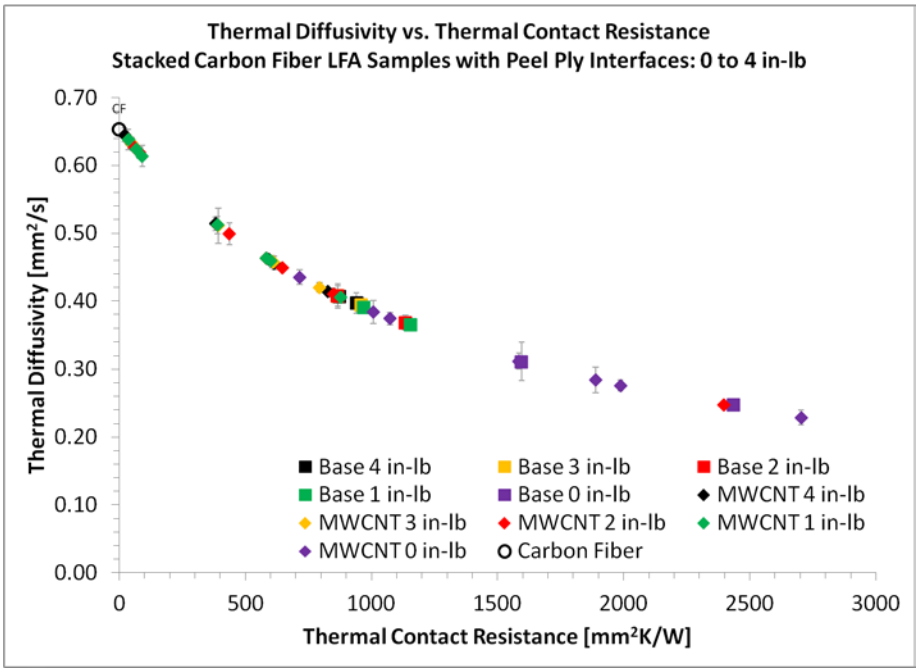

Figure 3-16 – Diffusivity vs. Contact Resistance for Peel Ply Interfaces at Low Pressures

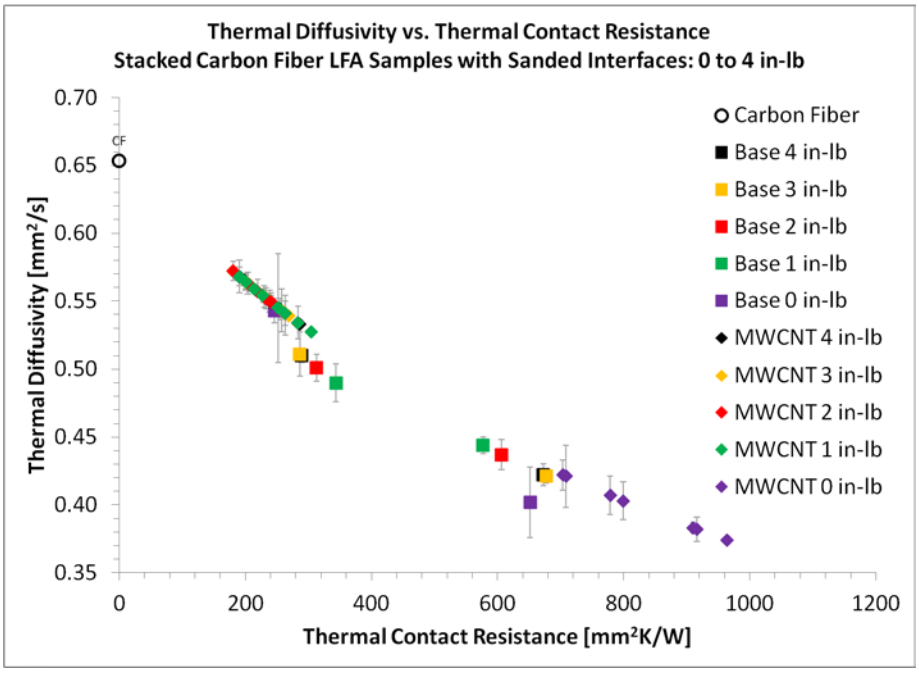

Figure 3-17 - Diffusivity vs. Contact Resistance for Sanded Interfaces at Low Pressures

One of the more interesting things to note from these plots is the exponential behavior of the data. Previously, the data had been seen on a shorter scale, causing it to appear linearly. This exponential behavior is logical, as contact resistance should increase toward infinity as diffusivity approaches zero. Also of interest is the relatively large increase in diffusivity achieved at minimal contact pressures. This gain is evidenced by Figure 3-18 below.

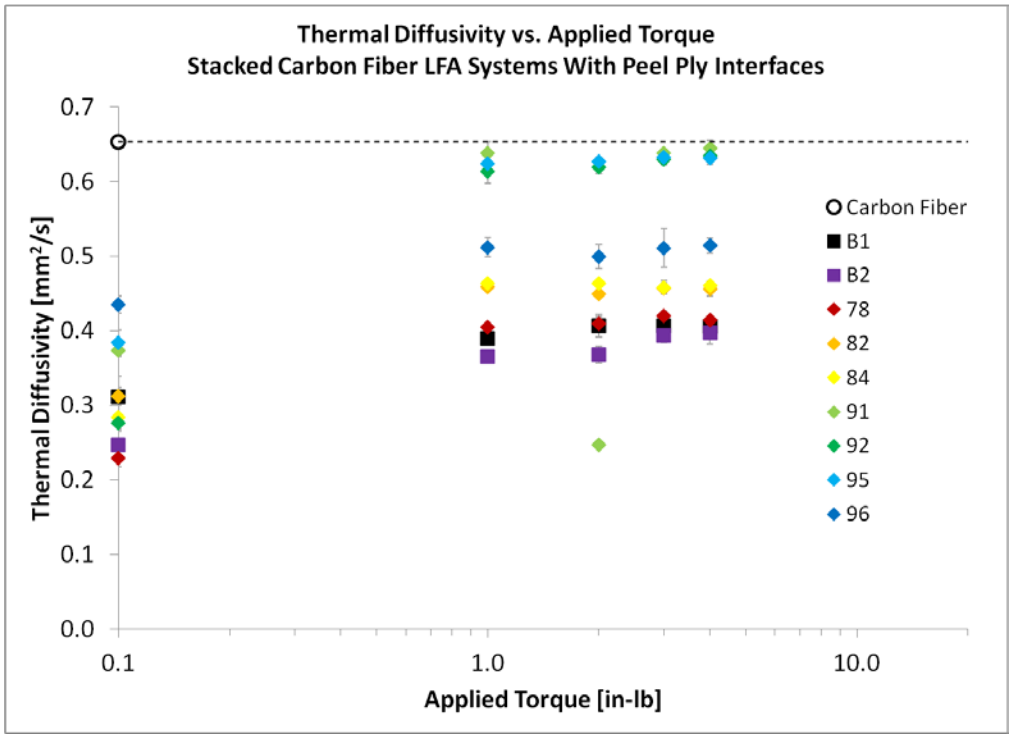

Figure 3-18 - Diffusivity vs. Applied Torque in Peel Ply Systems at Low Pressures

This figure indicates that thermal performance gains are realized as soon as intimate thermal contact is established (between 0 and 1 in-lb of torque). Beyond this initial performance jump, a diminishing returns situation arises, and results in more torque exerted with minimal thermal gains as a result. In terms of overall measured diffusivities, the carbon fiber material still limits any realistic measure of diffusivity to approximately 0.65 mm^2/s and below.

3.2.2.1 Effect of MWCNT Thickness on Thermal Performance

Previously it was determined that arrays with low thicknesses had a significantly better performance as a TIM in aluminum substrate interface systems. Figure 3-19 and Figure 3-20 below explore the effect of thickness on array TIM performance in low pressure carbon fiber substrate systems.

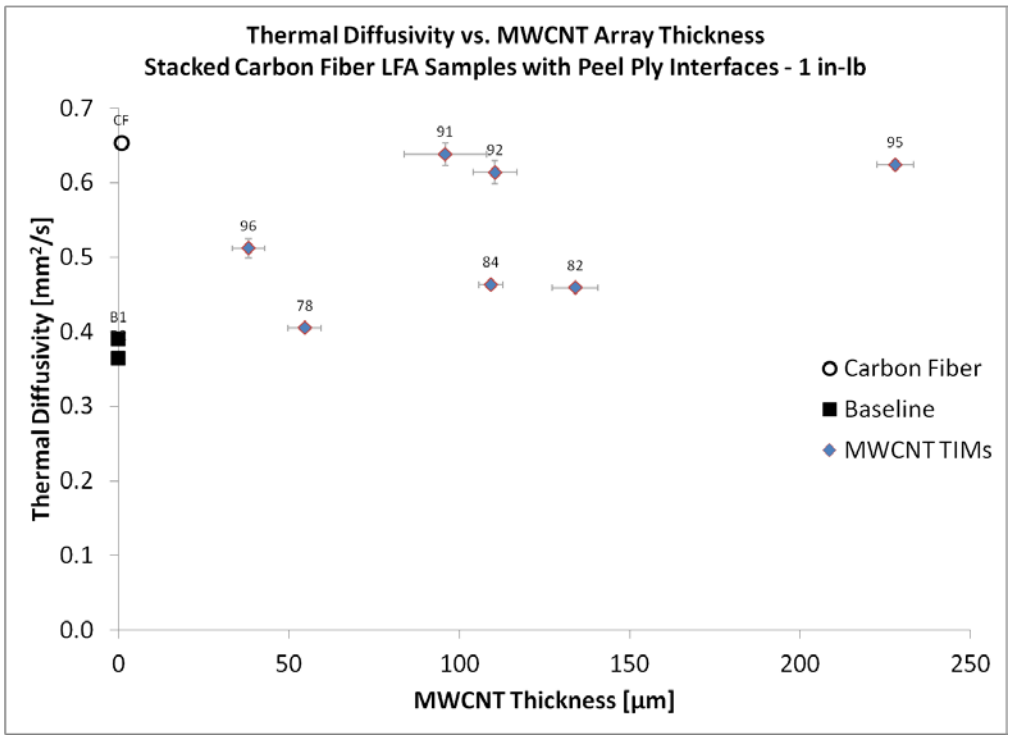

Figure 3-19 - Diffusivity vs. MWCNT Array Thickness in Peel Ply Systems at 1 in-lb

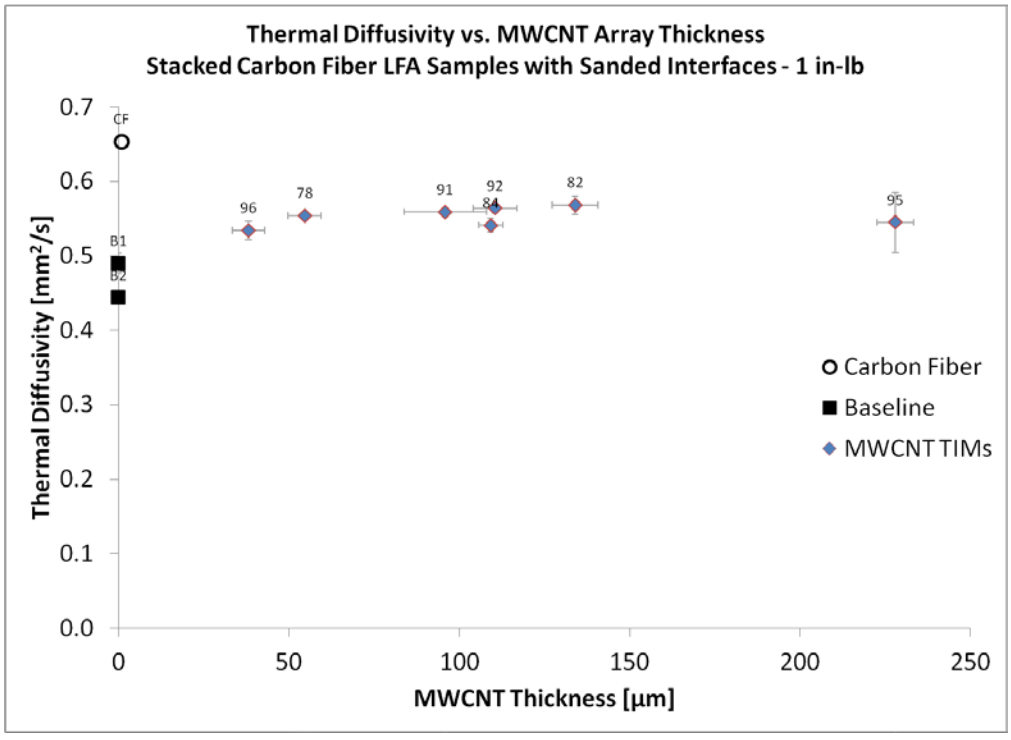

Figure 3-20 - Diffusivity vs. MWCNT Array Thickness in Sanded Systems at 1 in-lb

As can be seen in the figures above, aligned MWCNT array thickness seems to have no real effect on the overall thermal performance of carbon fiber systems with any interface style.

3.2.2.2 Effect of Packing Fraction on Thermal Performance

In the preceding chapter it was found that a high volumetric packing fraction was associated with excellent thermal performance of a TIM system with aluminum substrates. Figure 3-21 and Figure 3-22 below explore the effect of packing fraction on the thermal performance of array TIM systems in carbon fiber substrates under low contact pressures.

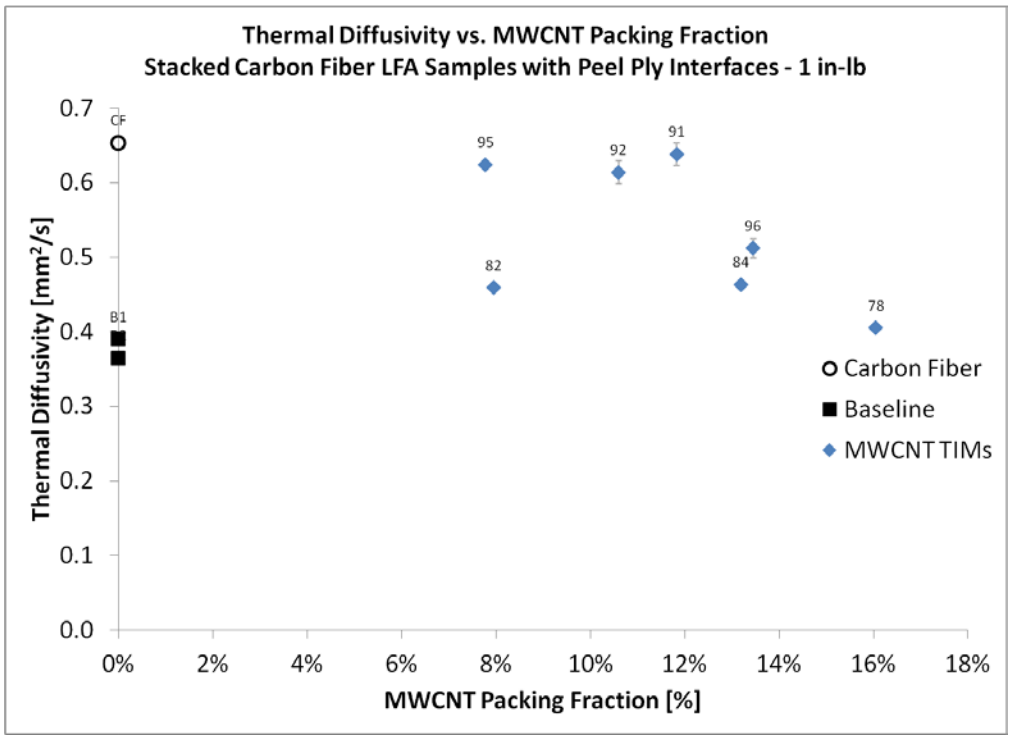

Figure 3-21 - Diffusivity vs. Packing Fraction in Peel Ply Systems at 1 in-lb

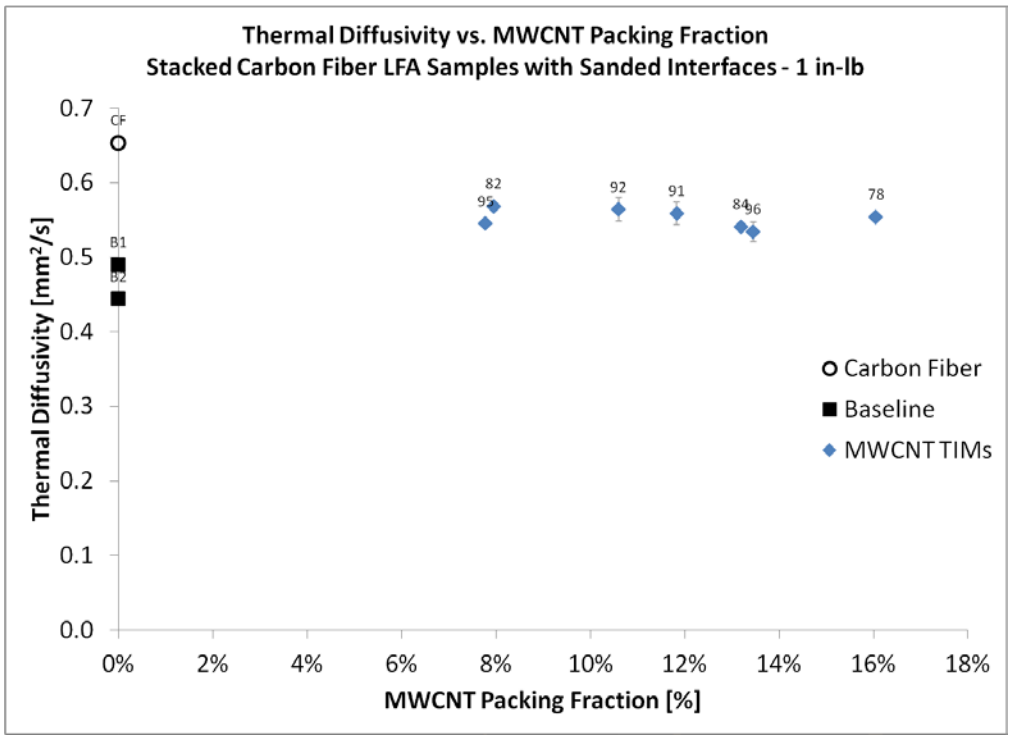

Figure 3-22 - Diffusivity vs. Packing Fraction in Sanded Systems at 1 in-lb

As shown above, the pattern previously found relating increasing packing fraction with increasing thermal performance is not seen in carbon fiber systems.

3.2.2.3 Effect of Areal Density on Thermal Performance

It was previously found that areal density of an aligned MWCNT array TIM had no measureable performance on the thermal performance of interface systems using those arrays as TIMS. This was due to the convolution of areal density with the bulk density, packing fraction, and array thickness. Figure 3-23 and Figure 3-24 below the effect of areal density in carbon fiber interface systems using aligned MWCNT array TIMs.

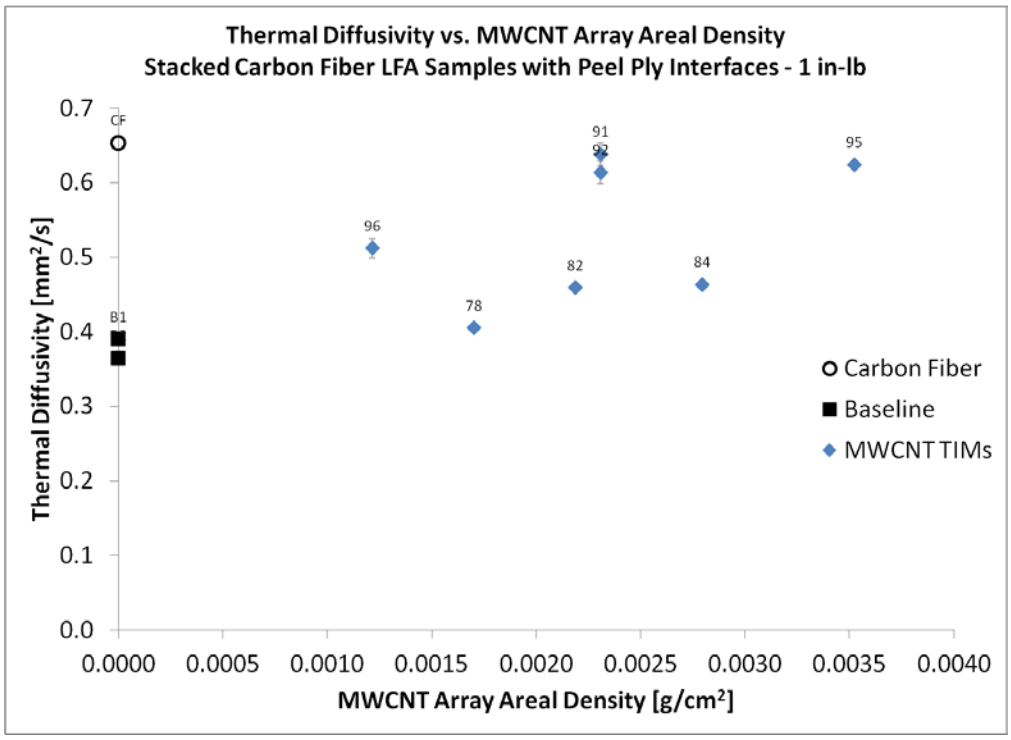

Figure 3-23 - Diffusivity vs. Array Areal Density in Peel Ply Systems at 1 in-lb

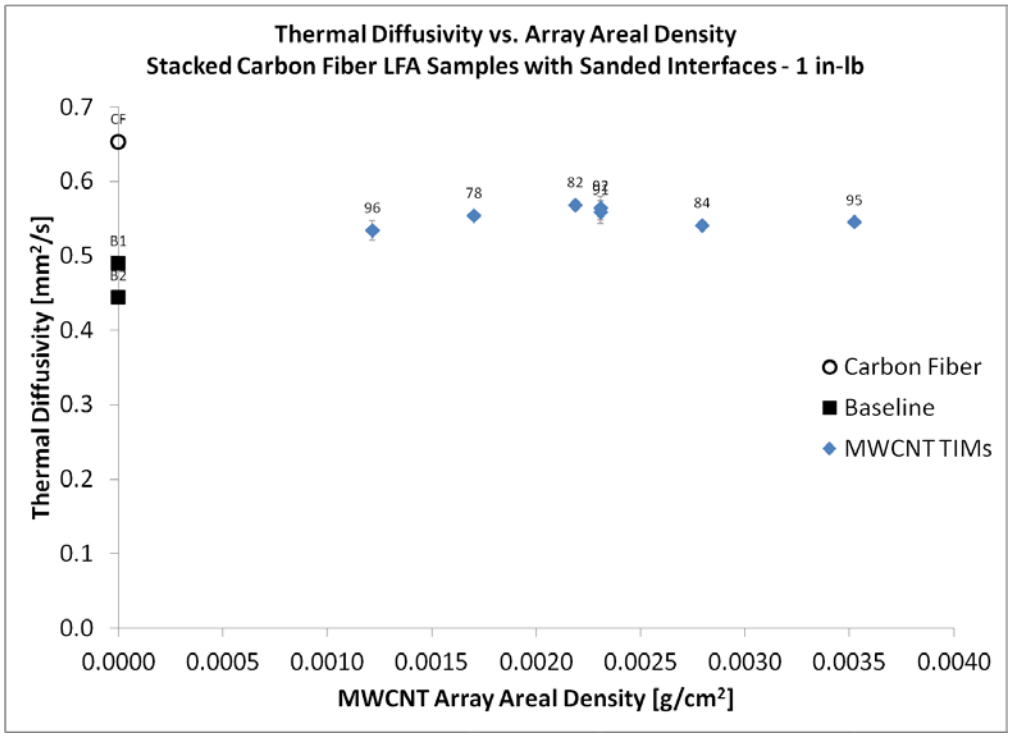

Figure 3-24 - Diffusivity vs. Array Areal Density in Sanded Systems at 1 in-lb

As can be seen above, there is also no discernible effect on the thermal performance attributed to the array TIM areal density in carbon fiber interface systems.

3.2.2.4 Effect of Bulk Density on Thermal Performance

In aluminum systems, high bulk density was found to be a desirable trait in an aligned MWCNT array TIM when excellent thermal performance was required. Figure 3-25 and Figure 3-26 below explore the effect of bulk density on TIM performance in carbon fiber interface systems.

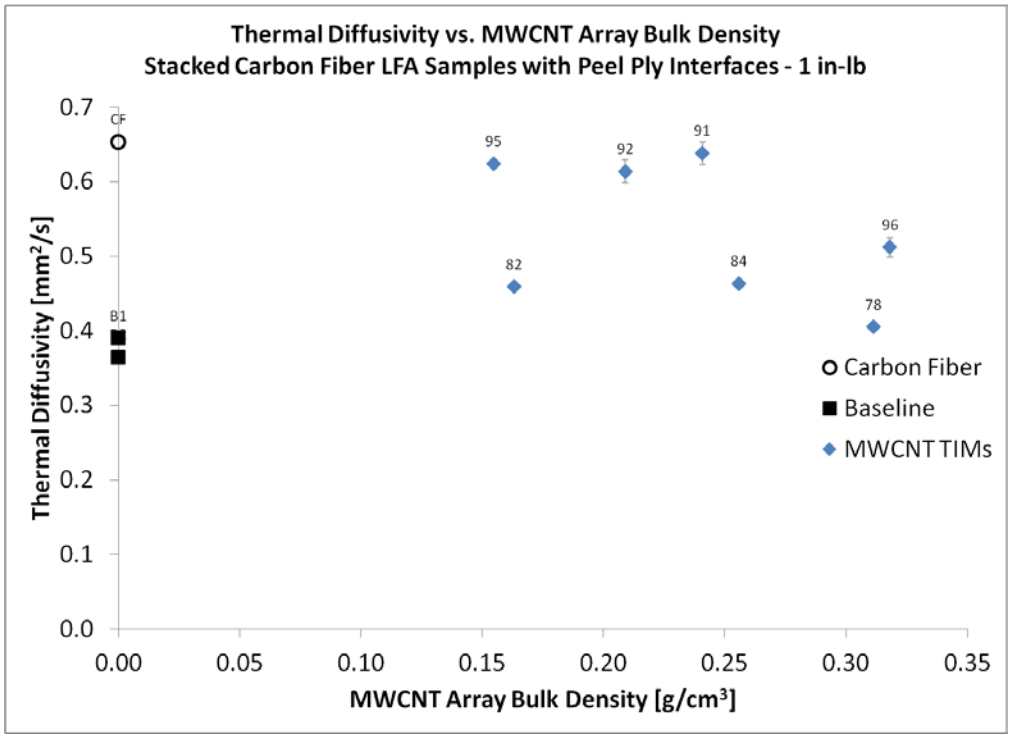

Figure 3-25 - Diffusivity vs. Bulk Density in Peel Ply Systems at 1 in-lb

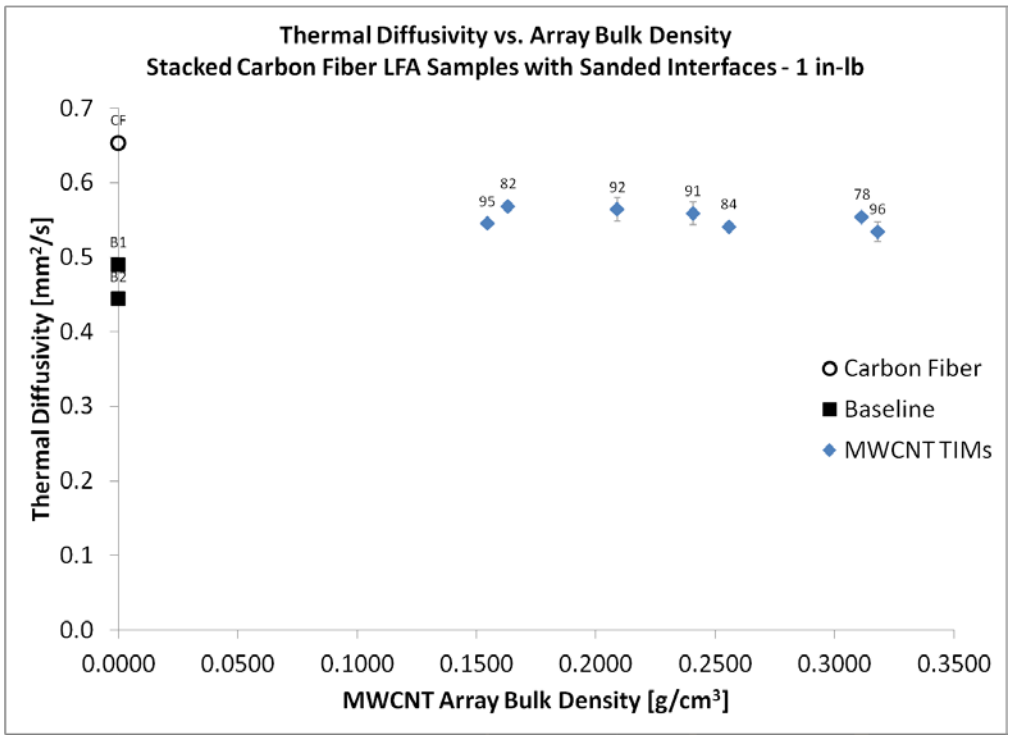

Figure 3-26 - Diffusivity vs. Bulk Density in Sanded Systems at 1 in-lb

As can be seen above, the effect of bulk density on aligned MWCNT array TIM performance does not present itself in carbon fiber systems as well.

3.2.2.5 Effect of Array cleanliness of Thermal Performance

It is well understood at this time that a clean array is of the utmost importance to a successful and effective TIM material. Figure 3-27 and Figure 3-28 below explore the thermal performance of aligned MWCNT array TIMs in carbon fiber systems at low pressures. A relationship between array mass removed by vacuum cleaning and thermal performance is sought.

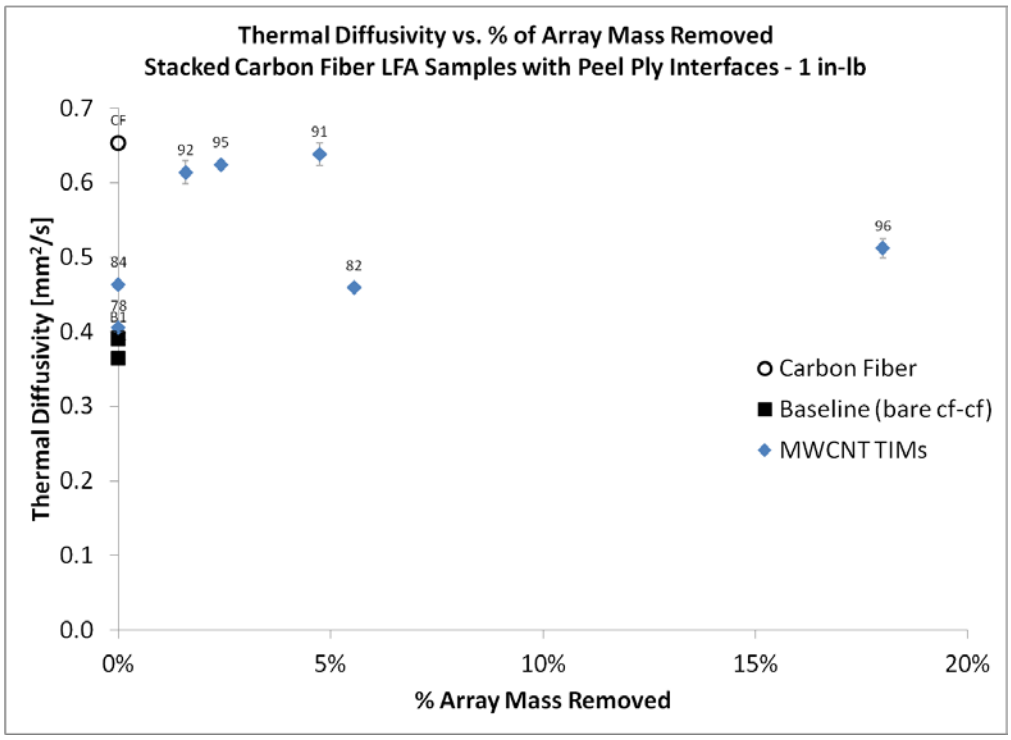

Figure 3-27 - Diffusivity vs. Array Weight Removed in Peel Ply Systems at 1 in-lb

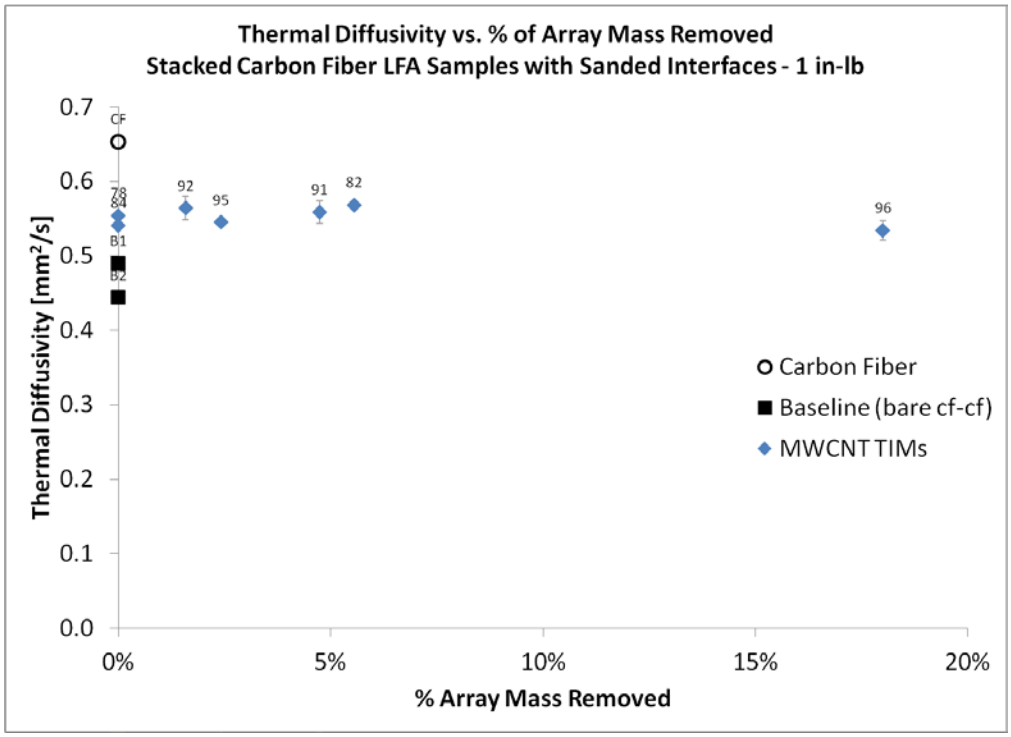

Figure 3-28 - Diffusivity vs. Array Weight Removed in Sanded Systems at 1 in-lb

As expected based on results for aluminum substrates at high and low contact pressures, and carbon fiber substrates at high contact pressures, there is minimal effect seen when comparing thermal performance to mass removed from an array by vacuum cleaning.

3.2.2.6 Low Contact Pressure LFA Results Conclusion

Throughout section 3.2.2 the effect of various array properties on their thermal performance in carbon fiber interface systems at low contact pressures has been presented. It was discovered that performance benefits of TIMs are seen at very low contact pressures (<30 psi). Beyond the initial jump in thermal performance, a diminishing returns situation exists where increasing contact pressure yields little or no further thermal performance benefits. As was found in higher pressure testing, array properties seem to have little effect on the overall thermal performance of carbon fiber array TIM systems.

3.3 Discussion

The results of this chapter indicate that through thickness heat transfer in stacked carbon fiber interface systems is not affected by the choice or suitability of a TIM material. So long as a TIM exists between two pieces of carbon fiber, a small gain in thermal performance will be seen at modest contact pressures (<30 psi). This shows that thermal transport in carbon fiber composites is not dominated by limitations of interfacial thermal contact, but rather by the thermal transport capabilities of the material itself. These findings are not thought to discredit the trends presented in Chapter 2. Rather, they are convoluted by the thermal capabilities of the carbon fiber substrate material itself and reveal the limitations of the Netzsch LFA 427 instrument.

As was discussed prior to presentation of high contact pressure carbon fiber LFA results, the carbon fiber material itself is a nonstandard substrate material. The LFA's thermal models rely on a 1-D heat transfer assumption which is only guaranteed by prudent material choices. These materials should be sufficiently homogenous (i.e. isotropic) and thin. The nominal thickness of the 6-ply carbon fiber composite material used was 1 mm, which is sufficiently thin to assume a one dimensional heat flow. The problems arise when considering the highly anisotropic heat conduction known to exist in carbon fiber composites, as diagrammed in Figure 3-3. In general,

the thermal models used in the LFA are not mathematically equipped to deal with these kinds of preferential heat flows.

In the case of the carbon fiber substrates, measured through thickness diffusivities are exceedingly low (<1 mm^2/s). In light of the preferential heat conduction displayed by carbon fiber composites, these measurements might still be appropriate. The same preferential heat paths will exist anywhere this material is used in a real world application, so assuming that heat will only travel through the thickness of the composite material is an unrealistic expectation. This does complicate the evaluation of materials as TIMs, such as aligned MWCNT arrays. Having only a small portion of the flashed laser energy distribute through the substrate set as intended (and the subsequent "late-arriving" contributions from the heat spreading first along the fiber axes, then up through the thickness) disturbs proper two layer measurements, leading to inconsistent measurements of thermal contact resistance.

3.4 Conclusion

At the beginning of this chapter, it was hypothesized that aligned MWCNT array TIMs with clean surfaces, high bulk density, high packing fraction, and low thickness will provide the best improvements in thermal performance in stacked carbon fiber interfacial systems. Through testing of array TIMs in two easily achievable carbon fiber composite substrate surface finishes and an extensive range of contact pressures, it was found that array properties have little to no effect on the thermal performance of the interfacial systems. Instead, it is concluded that the majority of challenges to thermal transport in these materials lie in the constituent material properties, rather than limitations of thermal transport across the interface. It is also suggested that future composites work should focus on ways to decrease the anisotropy found in carbon fiber composites. Increasing the through thickness thermal transport properties of the substrate materials will allow for more accurate thermal characterization of future aligned MWCNT array interface materials.

Chapter 4 Techniques Developed to Purify and Improve the Use of MWCNTs as TIMs

4.1 Introduction

Throughout Chapters 2 and 3, the use of as-produced, aligned MWCNTs as thermal interface materials has been discussed in aluminum and carbon fiber systems under varying interface conditions. Now methods of improving and/or purifying the MWCNT arrays to help them meet their full potential as TIMS will be discussed. Potential methods to be discussed include surface etching and nanotube height tailoring using radio frequency O_2 plasma oven processing and array annealing in a high temperature graphitization furnace.

4.2 Experimental

When harvesting an aligned MWCNT array from its quartz substrate, amorphous carbon deposits on top of the growth surface always exist. This layer is a byproduct of the CVD synthesis process used to produce the nanotubes, and is a function of several variables including synthesis temperature, catalyst/hydrocarbon ratio and furnace residence time. The synthesis process utilized by the Center for Applied Energy Research is continually optimized for maximum nanotube output, with minimum amorphous carbon deposits.

The layer of amorphous carbon is undesirable because it lacks an ordered, graphitic structure. It possesses an intrinsically low thermal conductivity of 0.2 W/mk [65], and excels at separating conductive MWCNT tips from interface substrates. This ruins any chance of aligned nanotube arrays making good thermal contact between surfaces, and can actually make the interfacial thermal contact resistance between two surfaces worse than if no TIM were used at all. An image of the top and bottom sides of an aligned MWCNT array is shown in Figure 4-1 below. The layer of amorphous carbon is clearly visible on one side of the array, while exposed nanotube tips are unhindered on the other. Figure 4-2 shows an aligned MWCNT in a clamped substrate system under ~130 psi assembly pressure. In this image, amorphous carbon is hindering good thermal contact between the MWCNT array and the substrate below it.

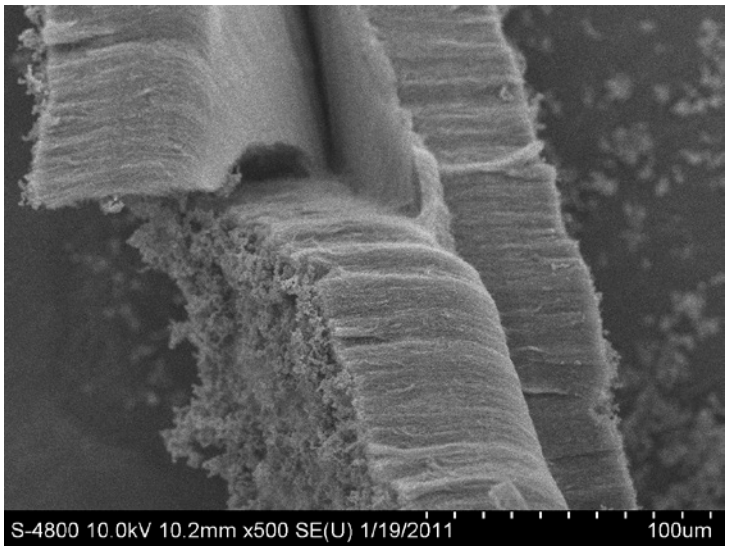

Figure 4-1 - SEM Image showing amorphous carbon deposits on an aligned MWCNT array

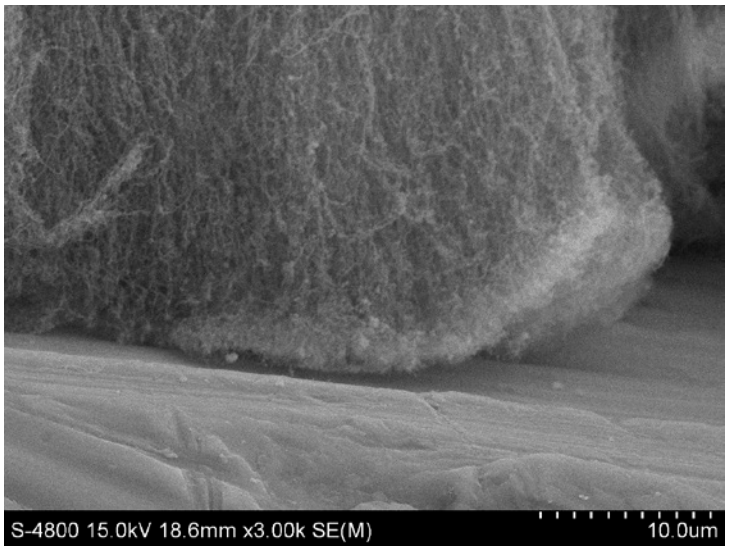

Figure 4-2 - Amorphous carbon blocking MWCNT tips from contacting a substrate

4.2.1 O_2 Plasma-Based Cleaning of MWNCT Arrays

The use of plasma cleaning systems to expose or augment the tips of aligned MWCNT arrays has been documented by others prior to these experiments [66, 67] . During this process, the sample is placed in a sealed chamber and the atmosphere is replaced with pure oxygen under constant venting. A variable power radio frequency generator is engaged, energizing the oxygen

to create plasma. The excited oxygen reacts with the sample surface at the molecular level, etching away oxidized molecules. These molecules are removed through the venting process.

It is hypothesized that O_2 plasma etching can remove the layer of amorphous carbon which covers the aligned MWCNT array tips. This method presents an economical, environmentally friendly[67] approach to purifying MWCNT surfaces, with potential to tailor the thickness of the array, producing a custom TIM for any interface. One of the goals of this experiment is to develop a recipe for cleaning nanotube arrays and tailoring their thicknesses.

The work of Felten, et al. suggests power levels and residence times in excess of 50 Watts for 10 minutes to chemically etch the surface of nanotubes, while Hinds, et al. suggested 2.5 W/cm^2 power settings for 7 minutes under 600 millitorr H_2O plasma to open nanotube tips. For this study, a TePla M4L RF Plasma Oven was used.

Figure 4-3 - TePla M4L RF Plasma Oven

Based on these suggestions and prior experience with the M4L Plasma Oven, an oxygen flow of 500 standard cubic centimeters per minute (sccm) was selected to maintain chamber pressures near 2000 millitorr. Power levels ranging from 50 Watts up to the maximum 600 Watts were tested, at successive residence times of 5, 15, 30, and 60 minutes. An acrylic sample frame was constructed to hold the array in place without providing extra metallic surfaces for the plasma to oxidize.

Array 97 was chosen as the test subject due to its representative thickness of ~100 µm and its extensive coating of amorphous carbon. These characteristics are shown in Figure 4-4 below.

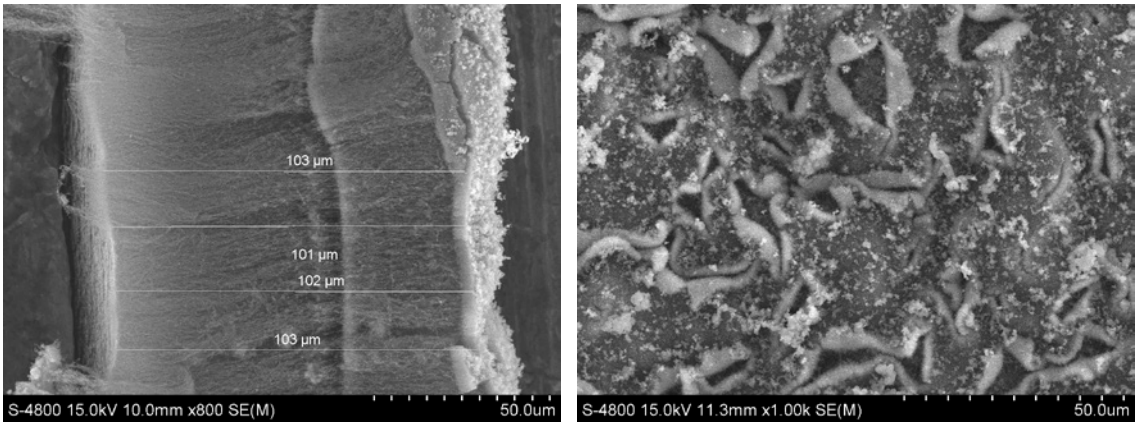

Figure 4-4 - Array 97 Thickness and Surface SEM Images

The images of array 97 show a dense layer of amorphous carbon entrained in the top extent of the array. This layer is blocking a large majority of nanotube tips from making good thermal contact between the interface substrates.

Testing the extremes of the experimental conditions revealed interesting outcomes. On the low end of power at 50 Watts, very little change was detected using SEM after 60 minutes of residence time. SEM images of baseline vs. etched thickness are shown in Figure 4-5 below.

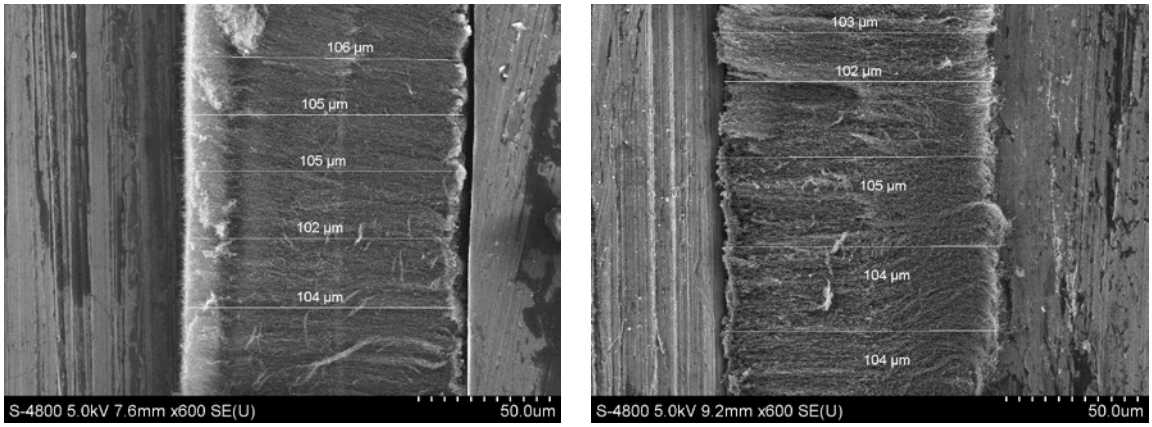

Figure 4-5 - SEM images of Array 97 Baseline (Left) vs. Etched at 50 W for 60 min (Right)

The baseline images for each power setting are of array samples within close proximity to the exposed nanotube surface, to ensure a proper comparative sample. As can be seen in the images above, after 60 minutes of residence time at 50 Watts there is no change in the overall

thickness of the sample. Building on these results, a maximum power test was conducted to see if any array height change was possible. A new sample was exposed to 600 Watts of RF power for 60 minutes. Digital camera images in Figure 4-6 below begin to describe the results.

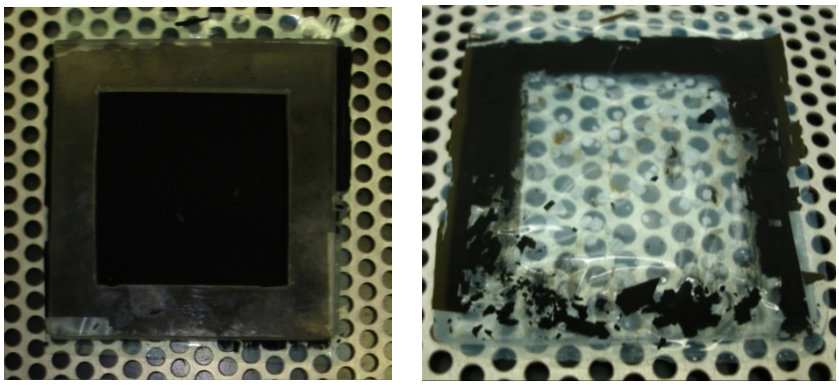

Figure 4-6 - Before and After Images of Array 97 Exposed to 600 W O_2 Plasma for 60 Min

As the images show, the array sample is completely obliterated after one hour at full power. Small sample pieces of array were found on the sample tray after the test and were collected for SEM imaging. Thickness and surface images are shown in Figure 4-7 below. Image A shows the average thickness of baseline array 97 from the sample set to be around 130 micron. Image B shows the average thickness of array 97 after etching at 600 Watts for 60 minutes to still be around 130 micron. Image C shows the surface of array 97 post-etching at 1000x magnification. Image D shows the surface of array 97 post-etching at 5000x magnification.

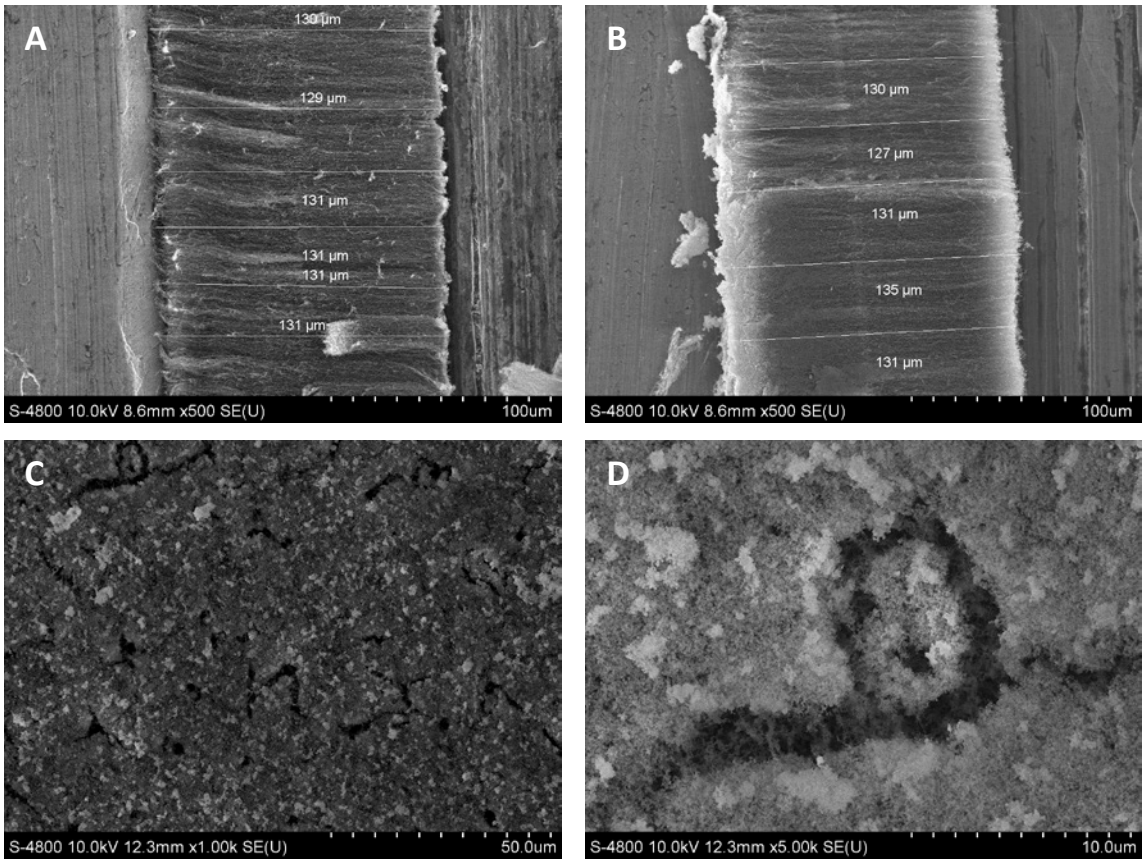

Figure 4-7 - Thickness/surface comparisons of Array 97 after 600W O2 plasma for 60 minutes

As images A and B show, even after 60 minutes of full power plasma etching there is no difference in thickness. Images C and D prove that amorphous carbon still persists on the surface of the array, even after violent plasma processing. After the sample was removed from the oven, it was noticed that a slight bronze coloration was present on the surface of the array which had been exposed to plasma. An image of this change can be seen in Figure 4-8 below.

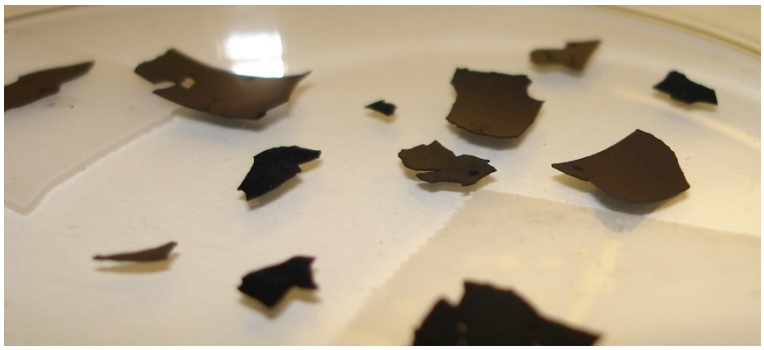

Figure 4-8 - Bronze coloration seen on MWCNT arrays after extreme O_2 plasma etching

Once it was determined that 600 Watts was simply too extreme to yield a processed sample for thermal testing, one final series of samples was produced at 300 watts. This power setting was much less violent toward the array, and provided SEM and LFA samples to thermally characterize the etched array. As previously mentioned, baseline thickness samples were taken prior to successive etching. At residence times of 5, 15, 30, and 60 minutes one quarter of the array was removed for SEM imaging and LFA testing. Since the fact that nanotube thickness does not change at higher RF power levels has already established, thickness images will be skipped in favor of monitoring surface changes to the array. These images are shown in figure below.

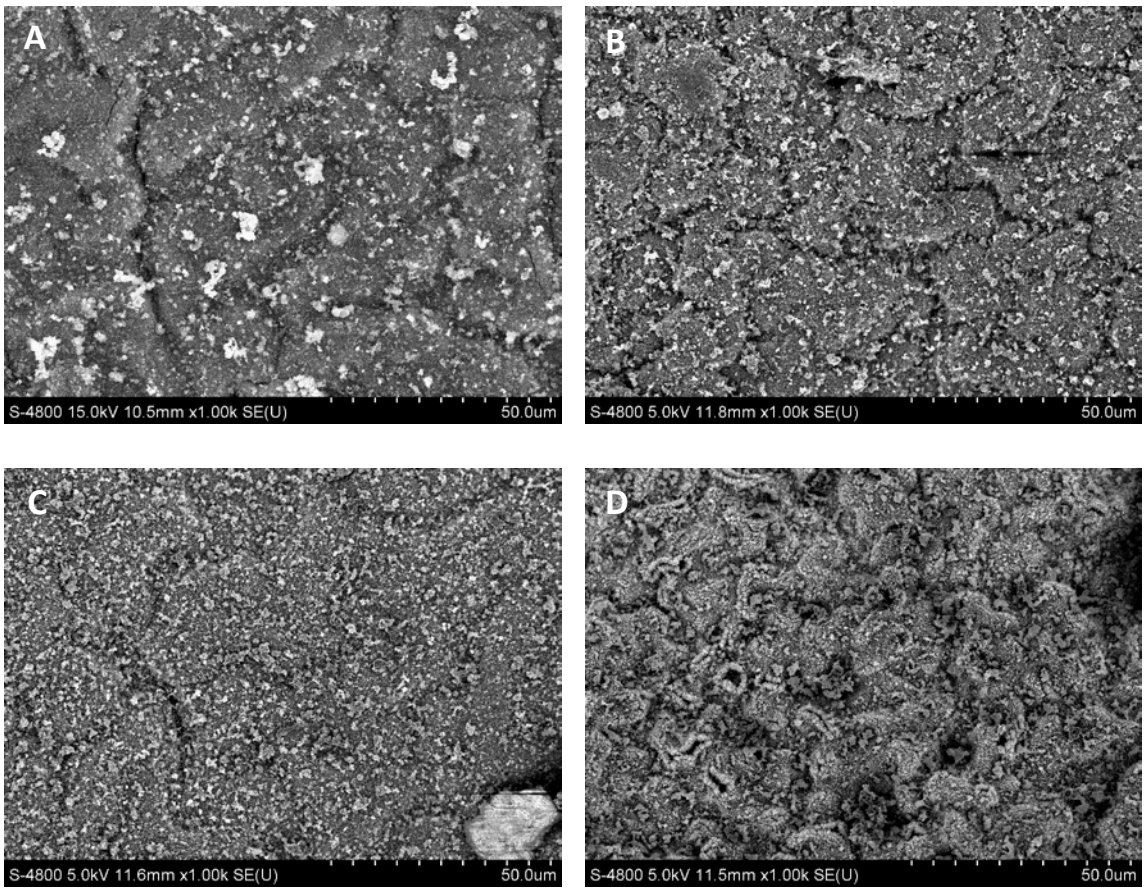

Figure 4-9 - Surface Changes in Array 97 at Increasing Residence Times - 300 Watts

Images A through D show the surface of Array 97 at 5, 15, 30, and 60 minutes of residence time (respectively) at 300 Watts of RF Power. It is clear that the surface layer does not etch away as predicted. Rather, it appears to change and become worse, with more surface features appearing between the detector and the nanotube tips encased beneath them. The same

bronze coloration that appeared in the 600 Watt tests was seen in the 60 minute sample under 300 Watt power. As shown in figure below, the bronze coloration makes it clear which portion of the array was covered by the acrylic testing frame.

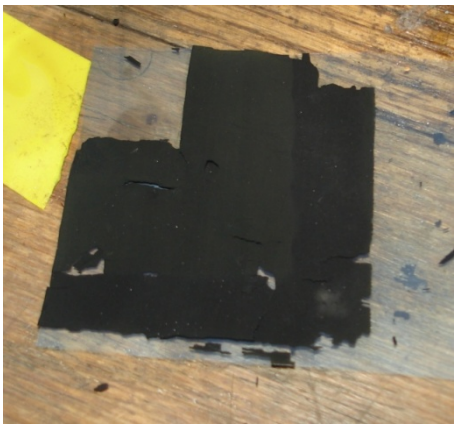

Figure 4-10 - Bronze Coloration Seen in 300 W – 60 min Sample

LFA testing was conducted at 3 in-lb torque on samples from all residence times as described in section 2.2 for aluminum substrates under low contact pressures. This helped characterize the effect of this bronzed layer on the overall thermal diffusivity of these etched arrays when used as a TIM. The results of these tests are shown in Figure 4-11 below.

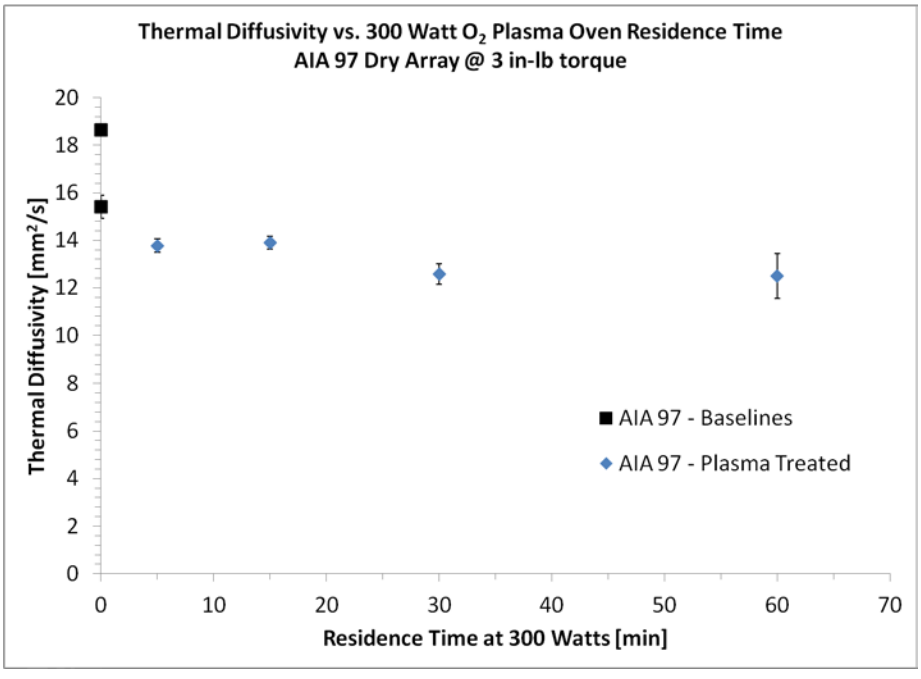

Figure 4-11 - Thermal Performance of Array 97 after 300 W – 60 min O_2 Plasma Etching

Clearly, this bronze-colored layer is not aiding the thermal performance of array 97. After finding decreased thermal performance from plasma etching, it is believed that the bronze layer on the surface of the array is iron oxide. It is possible that the amorphous carbon and carbon nanotube tips are being etched to a small degree, until trapped iron catalyst particles are exposed. Once oxygen reaches these particles, the iron will oxidize resulting in rust. This leaves a resistive coating with thermal conductivity from 0.5 – 4.5 W/mK [68] on the surface, which explains the decreased thermal performance.

4.2.2 Graphitization-Based Cleaning of MWCNT Arrays

High temperature annealing to purify carbon nanotubes has been used since the mid 1990s [69]. The basic principle is to subject samples to extreme temperatures in excess of 2400 °C in an inert atmosphere to force the evaporation of metal catalyst particles and initiate the reorganization and repair of the nanotubes' carbon structure into a more ordered, graphitic arrangement. Andrews et al. studied the effect of graphitization temperature on the structural perfection of multiwall carbon nanotubes and found that heat treatment above 1800 °C was sufficient to remove residual metal catalyst particles, with further treatment up to 3000 °C resulted in increasing graphitic perfection of nanotube wall structures [62]. Lastly, Weisenberger et al. studied the effect of graphitization temperature on the structure of helical ribbon carbon nanofibers. They found temperatures of 2400 °C and above were sufficient to remove all metal catalyst particles from the nanofibers, as well as change the surface morphologies from circular to a faceted polygonal structure indicative of planar graphene layers [70].

The hypothesis for this experiment is that graphitized arrays perform better than their predecessors as aligned MWCNT array TIMs. It has been documented that the annealing process provides the necessary energy for carbon atoms to rearrange their structure, thus repairing any Stone-Wales defects or minor kinks, as well as slightly decreasing the distance between concentric layers in a MWCNT. These improvements all result in a longer phonon mean free path through the array TIM which increases the effective TIM conductivity.

Thermal testing of graphitized vs. as-produced arrays was conducted in a similar style to the low contact pressure LFA testing of aluminum substrates as described in section 2.3.2. Annealing of array samples was conducted in a graphite furnace produced by Thermal Technology, Inc., pictured in Figure 4-12 below.

Figure 4-12 - Thermal Technology, Inc. Graphite Furnace

When annealing MWCNT samples, sheets of MWCNT array are placed in between 2" diameter pucks of pure graphite referred to as "biscuits," and the excess MWCNT array is trimmed away. These biscuits provide sufficient weight to hold the nanotube array samples in place while atmospheric purging is conducted, as well as provide additional localized heat to the array samples during annealing at extreme temperatures. An example of this biscuit stacking method, and loading a biscuit tower into the graphite furnace, is shown in Figure 4-13 below.

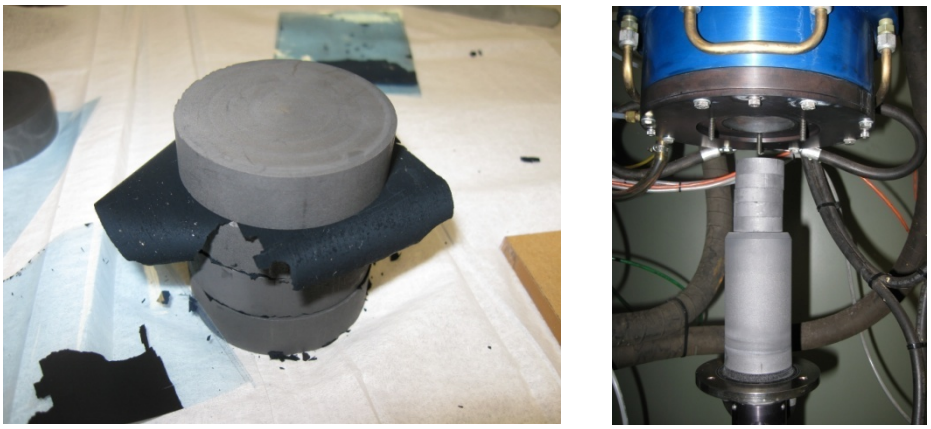

Figure 4-13 - Loading MWCNT Arrays into Graphite Biscuits and Loading the Furnace

Array samples that were annealed for these tests were all prepared at 2700 °C. Samples were exposed to an inert helium atmosphere and taken up to temperature with a 50 °C/min ramp.

Once at temperature, samples were held at 2700 °C for one hour before ramping back to room temperature at 50 °C/min. After annealing, samples were removed from the graphite furnace and carefully removed from the biscuit surfaces. An image of an annealed array is shown in Figure 4-14 below. In this image, the array has taken on a pattern from the biscuit.

Figure 4-14 - Aligned MWCNT Array - Post Graphitization

Thermal testing in aluminum substrate systems at low pressures yielded the following results, shown in Figure 4-15 below.

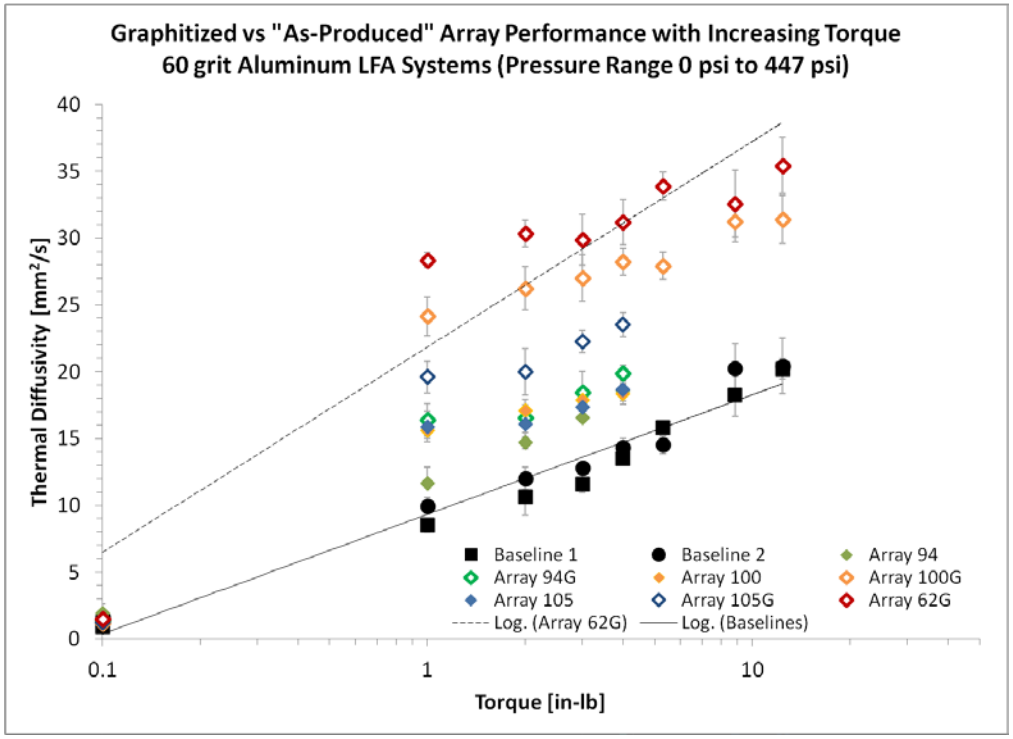

Figure 4-15 - Thermal Performance of Graphitized Arrays vs. “As-Produced” Arrays

As seen above, annealing arrays provided clear thermal performance benefits over their "as-produced" precursors. Array 62G is the only array tested which was not able to be paired with its as-produced predecessor. It was an older array, and no more original material remained for testing. Some arrays exhibited great improvements over their original form. Others like array 94 showed only moderate improvement. This can be explained with SEM images, recalling Figure 2-22 which showed inconsistent contact made by array 94. Graphitization can repair array defects, but it cannot grow more nanotubes to fill out patchy growth. Observant readers may notice that some arrays (as well as the baselines) were tested through the entire pressure range considered in this work. This was to ascertain whether a thermal performance "saturation point" existed, after which no further benefit would be seen, regardless of pressure. This chart shows that if such a point exists, it has not been reached yet. However, the maximum pressure in this chart is 447 psi, which is much higher than common contact pressures used in electronic components to date (usually less than 100 psi) [63].

4.3 Concluding Remarks

In this chapter, radio frequency oxygen plasma etching and high temperature annealing of aligned MWCNT array TIMs were utilized as processing methods to improve the thermal performance of array TIMs. Oxygen plasma was suggested based on the publications of previous groups indicating existing potential to etch arrays, as well as the idea of an economical and environmentally friendly method to tailor array TIM thickness. The reported findings of this work indicate that using oxygen plasma to chemically etch arrays does not produce cleaner or thinner arrays at the tested power and residence times. Further study may find the proper conditions for etching arrays, and would benefit the study of aligned MWCNT array TIMs.

High temperature annealing, or "graphitization" of aligned MWCNT array TIMs has proven itself a viable method of improving the thermal performance of these materials. Although successful, this method has economical drawbacks such as the large amount of time and energy necessary to anneal the arrays and expensive specialty furnace materials. Graphitizing an aligned MWCNT array TIM can have varying results, ranging from slight improvements in a poor array TIM to large improvements in a mediocre array. Based on the results of this Chapter, and the results of Chapter 2, the best possible TIM under current synthesis methods would be an annealed array with low thickness and high bulk density/packing fraction with exceptionally clean surfaces.

Chapter 5 Discussion of Results and Conclusion

5.1 Introduction

Throughout this work, various applications and treatments of aligned multiwall carbon nanotube arrays have been discussed with the ultimate goal of improving the through thickness thermal performance of interfacial systems. Thermal applications of nanotubes have been compared by measurement of thermal diffusivity and contact resistance in a Netzsch Instruments LFA 427 Laser Flash Analyzer. Mechanical applications have been compared by appropriate methods on mechanical testing frames at the Center for Applied Energy Research and at a third party.

5.2 MWCNT Arrays as TIMs in All-Aluminum Systems

In Chapter 2 of this work physical properties of aligned MWCNT arrays, as well as surface properties of stacked substrates and applied contact pressure, were investigated to determine the optimal properties of a TIM/Interface thermal system. Empirical trends emerged from these tests revealing which properties were most desirable in an aligned MWCNT array TIM.

5.2.1 Relationships between Array Properties and Thermal Performance

Properties considered important to the thermal performance enhancements seen when aligned MWCNT array TIMs are used are MWCNT array thickness, volumetric packing fraction, areal and bulk densities, and array surface cleanliness. Empirical trends revealed that the three most important properties of an effective array TIM were array thickness, packing fraction, and bulk density. Moreover, these trends revealed a convoluted interplay between these three, such that decreasing array thickness actually tended toward increasing bulk density and packing fraction. This idea is at odds with the traditional concept of bulk density, where changing thickness is accompanied by a proportional change in mass, and hence, does not affect the calculated density. It was concluded that the only way for decreasing thickness to actually increase density was by reducing the overall volume within the array that was occupied by air, which does not contribute to the measured array mass.

Additionally, a loose relationship between the measured mass of an array on its substrate (or areal density) prior to harvesting and its thermal performance after harvesting was established. Based on the current CVD nanotube synthesis methods employed for this study, arrays with less mass on the slide tend toward higher thermal performance. If one assumes the arrays to all be reasonably clean and free of amorphous carbon deposits, this line of thinking equates to the empirical trends of array thickness, packing fraction, and bulk density discussed previously. The measurement of array mass on the slide is the only method currently available to characterize array performance before committing personnel and resources to harvesting and processing the array. As such, knowing that lower mass generally tends toward higher performance is the single result allowing an educated guess to be made when picking arrays for TIM duty.

In addition to the physical properties of the arrays themselves, the surface roughness of stacked substrates and the applied contact pressure were considered in the overall thermal evaluation of the aligned MWCNT array TIMs. In aluminum systems, stacked substrates with roughness values ranging from R_A = 1.25 µm to R_A = 0.01 µm were used to test the sensitivity of array performance to interface surface preparation. In general, the highest reported diffusivities from an "as-produced" array TIM came from stacked mirror finish aluminum substrates with R_A = 0.01 µm. This is logical as there are fewer surface asperities for the nanotubes to work around; allowing even more nanotubes to remain axially aligned and providing a larger mean free path for phonon heat transport. However, this does not discount the results of TIM studies with a 60-grit surface finish (R_A = 1.25 µm) which indicated the superior conformability of the aligned MWCNT array TIMs. Reported baseline (bare interface) values for these systems were consistently lower than results from their TIM-assisted siblings. This indicates surface roughness is not as critical to successful heat transfer when an appropriate TIM is involved. Although, if one were concerned about thermal performance at designed material interfaces, it makes sense to specify reasonably smooth surface finishes wherever economically feasible.

Lastly, the applied contact pressure makes a great deal of difference to TIM performance. Under no applied pressure, aligned MWCNT array TIMs were ineffective at best. This is somewhat expected, as nothing is ensuring good thermal contact between the stacked substrates and the TIM. Fortunately, increases in pressure from 0 psi to values less than 30 psi are enough to create good thermal contact. Above the pressure where good thermal contact is initiated, further gains in thermal performances are experienced, but are less dramatic, even into the 400 psi regime.

Many technical applications of TIMs in electronics rely on assembly pressures less than 100 psi, which indicates that aligned MWCNT array TIMs are excellent choices for these applications.

5.2.2 Applications

Based on the performances of aligned MWCNT array TIMs noted in the aluminum systems of Chapter 2, there are several suggested applications for these materials. On a mass production scale, all consumer electronics currently relying on thermal greases, pastes, or pads could benefit from the robust heat transport and mechanical stability of carbon nanotube array TIMs. Additionally, satellites and other space-based thermal design challenges can be met with array TIMs because they have no greases to outgas and breakdown under vacuum.

5.3 MWCNT Arrays as TIMs in Carbon Fiber Composite Systems

In Chapter 3 of this work physical properties of aligned MWCNT arrays were investigated in stacked carbon fiber composite material systems. Several problems arose quickly, indicating the clear differences in testing this highly anisotropic material vs. an isotropic material such as the aluminum substrates previously discussed. In general, it is unclear whether or not the mathematical thermal models programmed into the LFA can accurately handle the challenges posed by these materials. Reported values of thermal diffusivity appear to be reasonable, when compared to the results of Zalameda, who reported diffusivity values between 0.0035 and 0.0062 cm^2/s (0.35 – 0.68 mm^2/s) for through thickness diffusivity of carbon fiber composites [71]. At this time, it is abundantly clear that no thermal contact resistances can be acceptably calculated by the thermal models of the LFA. As a remedy to this situation an excel-based iterative calculation was employed to approximate the interfacial contact resistance instead.

5.3.1 Relationships between MWCNT Array Properties and Thermal Performance

In general, none of the empirical trends that appeared when testing stacked aluminum interface systems were found in stacked carbon fiber interface systems. This should not suggest that the previously found trends relating array properties to thermal performance are incorrect. Instead, this is more a commentary on the extremely low through thickness diffusivity values reported by the LFA for carbon fiber composite materials. It is possible that the trends still exist, but it is difficult to see them based on the small range of diffusivity values reported. The only new trend which did arise was a relationship between contact pressure and thermal performance. Once

thermal contact is made, very little benefit is seen from additional contact pressure. All reported diffusivity values beyond the point of initial thermal contact were within standard deviation of each other, so nothing can be said about potential increases or decreases in thermal performance induced by higher contact pressures.

5.3.2 Applications

There is still some significant development work to be done before carbon fiber thermal interfaces can be recommended as a good thermal design practice. The widespread use of peel ply fabric in the composites industry means that nearly all carbon fiber composite material surfaces will have a highly dynamic surface finish, as illustrated previously in Figure 3-2. Materials like this will always benefit from the use of a TIM to decrease the thermal contact resistance across the interface. However, in the case of carbon fiber composite materials the material itself is the largest thermal bottleneck, not the interface. Future development work should be focused on improving the through thickness conductivity of carbon fiber composite materials themselves. Once this has been accomplished, aligned MWCNT array TIMs will be ready to bridge carbon fiber composite material interfaces.

5.4 Techniques to Purify and Improve the use of MWCNT Arrays as TIMs

In Chapter 4 of this work two methods for post processing of aligned MWCNT array TIMs were presented as ways to clean or otherwise improve their performance. Radio frequency oxygen plasma etching was attempted to selectively remove amorphous carbon deposits from the surface of the arrays. High temperature annealing, or "graphitization," was conducted to repair defects in the arrays inherent to the CVD synthesis process.

5.4.1 Effectiveness of Oxygen Plasma Cleaning Procedures

Oxygen plasma etching was considered because it presented the possibility of a relatively quick and economical improvement method, in addition to being environmentally friendly. Despite several groups reporting success using O_2 plasma etching methods to functionalize array tips (along with settings which should damage the array surface) difficulties were encountered trying to achieve a clearly reduced array thickness or reduced amorphous carbon layer.

Various settings from 50 Watts to 600 Watts were tried, at residence times ranging from 5 minutes to 60 minutes. SEM imaging revealed that even at the highest power level and residence times, no change in the overall thickness occurred. The array sample that was used in this test was utterly destroyed except for a few small pieces recovered for SEM imaging, which indicates that *something* happened to the array. Clearly, such high power settings would never be used for etching arrays longer than a few minutes in order to preserve the structural integrity of the sample.

A stable etching power was established at 300 Watts in order to create a testable range of samples at increasing residence times. It was found that time spent under O_2 plasma was actually hindering thermal performance of the arrays post processing. A bronze coating can faintly be seen on the surface of the array after extended time under plasma, which is believed to be oxidized iron catalyst particles that remain in all arrays produced by the CVD synthesis process. This layer of rust is much less conductive than the nanotubes it covers, which would explain the reduced thermal diffusivity values measured from O_2 plasma treated samples of array 97. Based on these results, O_2 plasma etching of nanotube arrays is not recommended at this time as a means of amorphous carbon removal.

5.4.2 Effectiveness of Graphitization-Based Cleaning Procedures

Exposing arrays to extreme high temperature under inert helium atmosphere provides enough energy to correct defects in the graphitic structure of the MWCNTs comprising the aligned array TIM. At temperatures above 1800 °C, the metal catalyst particles which are trapped in the center of the nanotubes during synthesis are evaporated out. This allows the nanotubes to constrict their diameter slightly and make the corrections to the arrangement of carbon atoms, returning to a proper hexagonal arrangement and more graphitic state. Figure 4-15 in Chapter 4 showed the thermal performance gains produced by graphitizing aligned MWCNT array TIMs. This method has established a track record of consistent improvements in array thermal performance, although the degree of improvement does depend on the array physical properties.

5.5 Conclusion

The results presented in this work provide a path forward for concentrated research in the field of aligned MWCNT array TIMs. These materials are highly desirable since they can be used in extreme environments like high temperature and/or high vacuum without penalty. The engineering and scientific communities maintain fervent interest in finding the best ways to leverage the excellent thermal and mechanical properties of these materials, while making them more user-friendly and economical. For MWCNT array based TIMs, the best performers tend to be those with clean surfaces, high bulk densities and packing fractions, and low thicknesses. Currently, these factors are not controllable in an industrial scale CVD synthesis process. Further research into the synthesis process with goals of enhanced product control will produce arrays with consistently excellent thermal performance for use as aligned MWCNT TIM materials.

Appendix A Data from High Pressure Aluminum LFA Testing

Table A-1: MWCNT Array TIMs used in Aluminum High Contact Pressure LFA Testing

MWCNT Array TIMs Tested - HIGH CONTACT PRESSURE ALUMINUM LFA TESTING								
Sample ID	Label	Average Thickness [µm]	Std. Dev Thickness [µm]	Mass on Slide [g]	Areal Density [g/cm^2]	Bulk Density [g/cm^3]	% Mass Removed	Packing Fraction
Array 62 Graphitized	62G	114.862	3.603	2.1	0.0026	0.222	0.00%	11.45%
Array 75	75	131.731	5.923	1.7	0.0021	0.157	0.00%	8.08%
Array 78	78	54.630	4.866	1.4	0.0017	0.311	0.00%	16.05%
Array 82	82	133.994	6.776	1.8	0.0022	0.163	5.56%	7.95%
Array 84	84	109.228	3.551	2.3	0.0028	0.256	0.00%	13.19%
Array 91	91	95.881	12.081	1.9	0.0023	0.241	4.74%	11.83%
Array 92	92	110.467	6.444	1.9	0.0023	0.209	1.58%	10.60%
Array 93	93	124.709	10.436	1.7	0.0021	0.166	2.35%	8.37%
Array 94	94	48.318	2.657	0.9	0.0011	0.226	11.11%	10.37%
Array 95	95	227.906	5.354	2.9	0.0035	0.155	2.41%	7.78%
Array 96	96	38.195	4.741	1.0	0.0012	0.318	18.00%	13.45%
Array 97	97	108.080	4.242	1.3	0.0016	0.146	2.31%	7.36%
Array 98	98	118.946	10.706	2.2	0.0027	0.225	2.27%	11.32%
Array 99	99	190.375	20.910	2.4	0.0029	0.153	2.50%	7.70%
Array 100	100	195.467	7.642	2.1	0.0026	0.131	2.38%	6.57%
Array 101	101	152.719	7.437	1.5	0.0018	0.119	2.67%	5.99%

Table A-2: Mill Finish Aluminum Thermal Results - High Contact Pressure Testing

MILL FINISH RESULTS - HIGH CONTACT PRESSURE ALUMINUM LFA TESTING													
Sample ID	Label	Thermal Diffusivity [mm^2/s]			Contact Res. [mm^2K/W]			St. Dev - Diffusivity [mm^2/s]			St. Dev - Contact Res. [mm^2K/W]		
		60 cNm	100 cNm	140 cNm	60 cNm	100 cNm	140 cNm	60 cNm	100 cNm	140 cNm	60 cNm	100 cNm	140 cNm
Array 62 Graphitized	62G	32.21	34.41	39.98	46.00	45.13	36.19	2.20	2.17	2.70	3.51	3.23	5.39
Array 75	75	30.93	32.19	34.53	74.64	65.75	51.94	1.11	0.50	0.75	7.32	5.93	4.93
Array 78	78	36.94	37.60	37.65	56.00	51.98	40.38	0.98	0.74	0.70	12.46	1.14	2.14
Array 82	82	30.20	29.69	31.95	74.20	68.85	65.74	0.65	0.37	0.98	3.66	0.45	10.72
Array 84	84	23.87	23.68	25.88	128.53	116.70	103.73	2.20	1.19	0.69	7.56	1.31	8.27
Array 91	91	26.04	29.88	31.87	94.81	69.79	82.20	0.22	2.58	1.64	10.62	2.18	11.58
Array 92	92	26.16	28.37	28.46	101.17	94.65	86.11	0.78	1.96	0.25	17.33	8.57	12.28
Array 93	93	25.11	28.60	29.94	107.80	80.75	68.73	0.21	1.04	0.54	3.91	7.94	3.63
Array 94	94	22.87	24.06	26.69	131.60	98.25	78.00	0.64	1.30	1.62	16.13	6.21	8.85
Array 95	95	19.03	23.39	25.04	149.70	110.13	105.44	1.21	0.99	1.77	21.22	0.47	4.98
Array 96	96	25.15	27.98	33.15	93.83	63.06	75.03	1.01	2.27	1.79	15.11	9.00	21.88
Array 97	97	21.98	27.00	26.90	123.10	97.71	96.76	0.50	0.81	0.61	7.27	10.26	5.81
Array 98	98	26.18	27.12	31.25	84.97	71.99	62.93	1.79	2.21	0.66	15.53	7.82	2.19
Array 99	99	20.05	23.70	20.18	146.83	135.00	131.50	1.75	1.59	0.82	39.60	9.23	15.42
Array 100	100	22.74	25.12	25.51	120.28	88.92	86.86	3.09	3.18	3.04	8.00	3.39	28.86
Array 101	101	17.99	22.88	22.85	166.37	130.53	104.82	0.41	2.27	1.45	24.90	26.01	6.60
Baseline 1	B1	23.21	27.13	28.12	124.63	102.63	95.11	0.65	0.55	0.63	10.15	6.72	6.89
Baseline 2	B2	19.63	26.46	28.01	145.37	99.18	95.35	0.74	0.31	0.80	9.56	4.42	6.81
Baseline 3	B3	19.97	23.80	24.47	152.03	120.27	112.17	0.69	0.94	0.78	13.98	8.56	7.90

Table A-3: Mirror Finish Aluminum Thermal Results - High Contact Pressure LFA Testing

MIRROR FINISH RESULTS - HIGH CONTACT PRESSURE ALUMINUM LFA TESTING													
Sample ID	Label	Thermal Diffusivity [mm^2/s]			Contact Res. [mm^2K/W]			St. Dev - Diffusivity [mm^2/s]			St. Dev - Contact Res. [mm^2K/W]		
		60 cNm	100 cNm	140 cNm	60 cNm	100 cNm	140 cNm	60 cNm	100 cNm	140 cNm	60 cNm	100 cNm	140 cNm
Array 78	78	36.38	36.54	38.94	52.63	40.29	41.70	0.90	1.56	1.24	1.68	6.18	4.74
Array 82	82	22.43	27.37	29.81	94.68	77.61	72.98	6.71	1.14	0.99	3.93	11.08	0.96
Array 84	84	22.18	23.44	23.41	142.20	119.03	109.67	1.34	0.46	3.20	0.87	5.18	13.03
Array 91	91	27.96	30.36	32.18	76.99	70.52	59.97	0.33	1.11	0.68	2.74	6.57	1.48
Array 92	92	26.23	26.73	29.56	105.03	77.93	71.37	0.81	0.70	1.64	12.14	6.35	3.61
Array 93	93	24.42	27.41	28.09	110.70	98.42	200.77	0.30	0.88	1.08	4.54	4.84	8.08
Array 94	94	25.44	27.77	29.90	119.67	87.48	74.45	0.91	0.17	0.38	1.80	7.75	6.03
Array 95	95	21.49	24.80	26.75	125.17	102.53	103.03	1.77	2.36	1.32	4.92	8.20	8.56
Array 96	96	22.45	27.66	30.38	100.76	92.06	66.89	1.11	2.04	1.87	3.54	11.48	7.99
Array 97	97	22.73	27.32	31.02	114.43	80.15	68.26	1.15	0.96	0.32	10.15	10.10	4.87
Array 98	98	26.10	27.99	28.95	99.26	91.72	79.47	1.99	1.30	2.42	6.51	24.58	17.80
Array 99	99	20.00	27.11	29.23	95.02	84.14	81.25	2.73	1.98	1.30	17.55	3.87	18.02
Array 100	100	19.23	22.25	26.21	138.20	146.53	98.67	3.20	2.45	1.43	12.41	48.99	5.28
Array 101	101	22.37	23.72	23.77	122.03	92.62	79.35	2.10	1.81	1.40	14.53	5.29	11.85
Baseline 1	B1	28.00	30.68	34.27	82.50	63.86	80.59	0.31	0.35	1.10	2.68	11.44	5.49
Baseline 2	B2	30.02	30.95	30.40	78.31	71.17	70.75	0.68	0.72	0.34	3.46	4.09	6.76
Baseline 3	B3	22.66	25.19	28.37	120.30	106.60	85.43	0.37	0.76	0.93	2.25	10.39	7.08

Appendix B Data from Low Contact Pressure Aluminum LFA Testing

Table B-1: MWCNT Array TIMs used in Aluminum Low Contact Pressure LFA Testing

MWCNT Array TIMs Tested - LOW CONTACT PRESSURE ALUMINUM LFA TESTING						
Sample	Average Thickness [μm]	Std. Dev Thickness [μm]	Areal Density [g/cm^2]	Bulk Density [g/cm^3]	% Mass Removed	Packing Fraction
Array 62 Graphitized	114.86	3.603	0.0026	0.2222	-	11.45%
Array 75	131.73	5.923	0.0021	0.1568	0.00%	8.08%
Array 78	54.63	4.866	0.0017	0.3114	0.00%	16.05%
Array 82	133.99	6.776	0.0022	0.1632	5.56%	7.95%
Array 84	109.23	3.551	0.0028	0.2559	0.00%	13.19%
Array 91	95.88	12.081	0.0023	0.2408	4.74%	11.83%
Array 92	110.47	6.444	0.0023	0.2090	1.58%	10.60%
Array 93	124.71	10.436	0.0021	0.1656	2.35%	8.37%
Array 94	48.32	2.657	0.0011	0.2263	11.11%	10.37%
Array 94 Graphitized	48.32	2.657	0.0011	0.2263	-	10.37%
Array 95	227.91	5.354	0.0035	0.1546	2.41%	7.78%
Array 96	38.20	4.741	0.0012	0.3181	18.00%	13.45%
Array 97	108.08	4.242	0.0016	0.1462	2.31%	7.36%
Array 98	118.95	10.706	0.0027	0.2247	2.27%	11.32%
Array 99	190.38	20.910	0.0029	0.1532	2.50%	7.70%
Array 100	195.47	7.642	0.0026	0.1305	2.38%	6.57%
Array 100 Graphtitized	195.47	7.642	0.0026	0.1305	-	6.57%
Array 101	152.72	7.437	0.0018	0.1193	2.67%	5.99%
Array 105	92.27	5.427	0.0018	0.1975	3.33%	9.84%
Array 105 Graphitized	92.27	5.427	0.0018	0.1975	-	9.84%

Table B-2: Al Thermal Diffusivity Results - Low Contact Pressure LFA Testing

Sample	Label	Thermal Diffusivity, α, [mm²/s]								Standard Deviation, σ, [mm²/s]							
		0 in-lb	1 in-lb	2 in-lb	3 in-lb	4 in-lb	5.31 in-lb	8.85 in-lb	12.39 in-lb	0 in-lb	1 in-lb	2 in-lb	3 in-lb	4 in-lb	5.31 in-lb	8.85 in-lb	12.39 in-lb
Baseline 1	B1	0.94	8.50	10.66	11.61	13.49	15.82	18.26	20.22	0.044	0.497	1.392	0.652	0.391	0.389	1.586	0.765
Baseline 2	B2	1.65	9.97	11.99	12.79	14.34	14.53	20.27	20.42	0.947	0.602	0.843	0.188	0.664	0.671	1.844	2.086
Array 62 Graphitized	62G	1.52	28.34	30.34	29.89	31.18	33.89	32.57	35.43	0.226	0.554	1.015	1.899	1.689	1.058	2.509	2.066
Array 75	75	1.62	19.52	20.81	23.05	22.94	23.42	25.07	27.58	0.168	0.551	1.560	2.488	1.625	1.983	0.448	0.249
Array 78	78	1.39	18.49	21.25	20.53	24.56	25.93	27.89	28.61	0.079	0.302	0.860	0.778	0.127	2.862	2.531	2.080
Array 82	82	1.96	23.56	24.75	24.66	26.21	-	-	-	0.200	1.783	0.845	1.732	1.824	-	-	-
Array 84	84	1.30	17.01	18.36	19.48	20.18	-	-	-	0.099	0.306	0.171	0.191	0.234	-	-	-
Array 91	91	1.31	16.44	16.89	18.90	19.27	-	-	-	0.100	1.044	0.797	1.370	0.497	-	-	-
Array 92	92	1.49	17.29	18.91	19.23	19.97	-	-	-	0.215	0.143	0.030	1.125	0.540	-	-	-
Array 93	93	1.32	18.73	19.05	20.66	20.63	-	-	-	0.198	0.527	0.583	0.357	0.555	-	-	-
Array 94	94	1.93	11.65	14.68	16.55	18.55	-	-	-	0.277	0.159	0.432	0.317	0.965	-	-	-
Array 94 Graphitized	94G	1.40	16.40	16.53	18.43	19.90	-	-	-	0.137	1.212	1.386	1.597	0.586	-	-	-
Array 95	95	1.42	16.19	17.18	18.01	19.33	-	-	-	0.163	0.371	0.269	0.590	0.820	-	-	-
Array 96	96	1.21	10.03	11.44	12.85	14.14	14.71	19.24	20.42	0.201	1.149	0.498	0.499	0.212	0.506	1.529	1.616
Array 96, Test 2	96-2	0.40	10.28	11.26	12.68	14.44	-	-	-	0.104	0.582	0.736	0.523	0.953	-	-	-
Array 92	97	2.40	13.03	14.30	15.41	16.45	-	-	-	0.180	0.384	0.176	0.495	0.577	-	-	-
Array 97, Test 2	97-2	1.21	16.01	16.79	18.64	18.29	-	-	-	0.096	0.368	0.885	0.176	1.380	-	-	-
Array 98	98	1.38	16.83	19.31	19.44	20.71	-	-	-	0.197	0.819	1.083	0.122	0.724	-	-	-
Array 99	99	1.16	1.39	15.51	17.73	18.04	-	-	-	0.236	0.101	0.818	0.362	0.992	-	-	-
Array 99, Test 2	99-2	1.74	14.98	16.71	17.69	17.73	-	-	-	0.291	0.648	0.637	0.369	0.316	-	-	-
Array 100	100	1.35	15.60	17.06	17.87	18.35	-	-	-	0.082	0.554	0.424	0.332	0.543	-	-	-
Array 100 Graphitized	100G	1.16	24.14	26.23	27.02	28.23	27.91	31.24	31.40	0.108	1.460	1.613	1.752	1.004	1.031	1.528	1.796
Array 101	101	1.66	13.70	15.88	15.90	17.00	-	-	-	0.371	0.686	0.590	0.682	0.710	-	-	-
Array 105	105	1.54	15.88	16.08	17.35	18.65	-	-	-	0.136	1.137	0.622	0.338	0.456	-	-	-
Array 105 Graphitized	105G	1.21	19.61	19.98	22.27	23.53	-	-	-	0.179	1.183	1.735	0.843	0.899	-	-	-

Table B-3: Al Thermal Contact Resistance Results - Low Contact Pressure LFA Testing

Sample	Label	Thermal Contact Resistance, R_c, [mm^2K/W]							Standard Deviation, σ, [mm^2K/W]						
		0 in-lb	1 in-lb	2 in-lb	3 in-lb	4 in-lb	5.31 in-lb	8.85 in-lb	12.39 in-lb	0 in-lb	1 in-lb	2 in-lb	3 in-lb	4 in-lb	5.31 in-lb	8.85 in-lb	12.39 in-lb
Baseline 1	B1	6774.00	352.30	335.50	261.50	240.70	201.70	142.90	124.00	2795.00	33.27	28.09	12.69	19.99	9.23	10.21	13.94
Baseline 2	B2	11690.00	372.90	272.70	270.80	239.50	191.20	127.60	102.80	8975.00	40.34	16.12	14.85	22.01	17.93	5.45	10.63
Array 62 Graphitized	62G	4856.00	74.15	63.92	60.90	55.30	50.92	46.03	42.64	2149.00	4.64	2.53	5.24	2.15	3.03	4.95	1.83
Array 75	75	3357.00	137.40	116.30	104.30	95.20	95.22	82.14	82.56	416.60	1.64	3.73	2.97	9.18	11.87	5.44	6.63
Array 78	78	4685.00	138.40	118.50	98.29	91.83	84.23	65.78	61.21	882.40	2.56	4.42	13.95	2.29	6.20	3.85	3.65
Array 82	82	2461.00	106.00	97.26	89.02	88.94	-	-	-	383.60	10.82	6.96	5.13	2.27	-	-	-
Array 84	84	3927.00	191.20	170.10	163.90	145.60	-	-	-	947.40	7.90	7.97	5.31	7.75	-	-	-
Array 91	91	7357.00	168.00	153.10	136.80	136.00	-	-	-	5723.00	6.81	10.62	2.51	8.05	-	-	-
Array 92	92	3134.00	179.70	154.10	144.30	139.80	-	-	-	446.70	15.70	6.69	6.56	3.81	-	-	-
Array 93	93	3459.00	153.20	141.80	142.50	138.90	-	-	-	581.20	2.39	3.79	4.85	5.27	-	-	-
Array 94	94	2839.00	331.50	236.40	202.00	155.50	-	-	-	339.80	24.43	12.51	18.43	1.14	-	-	-
Array 94 Graphitized	94G	4947.00	183.70	141.60	131.10	122.80	-	-	-	562.50	15.60	3.10	3.28	1.04	-	-	-
Array 95	95	4108.00	201.40	174.90	157.00	132.80	-	-	-	689.80	6.10	16.01	9.47	13.42	-	-	-
Array 96	96	4045.00	338.80	317.20	261.40	235.40	194.10	148.80	107.30	801.60	14.40	29.38	11.11	8.96	17.25	16.18	8.72
Array 96, Test 2	96-2	159200.00	353.30	281.50	262.70	216.40	-	-	-	0.00	23.34	23.22	16.66	13.94	-	-	-
Array 92	97	-	257.50	224.40	189.60	181.80	-	-	-	-	9.06	13.52	21.22	2.55	-	-	-
Array 97, Test 2	97-2	3645.00	184.70	166.50	153.20	152.20	-	-	-	679.50	10.29	3.53	10.62	16.76			
Array 98	98	4243.00	191.10	158.00	132.70	137.70	-	-	-	1432.00	6.05	7.53	1.43	10.90	-	-	-
Array 99	99	3265.00	3765.00	198.70	174.60	144.80	-	-	-	207.20	334.40	5.44	12.52	6.45	-	-	-
Array 99, Test 2	99-2	14260.00	253.90	202.00	188.60	174.10	-	-	-	19790.00	29.92	16.46	10.72	4.82	-	-	-
Array 100	100	38450.00	222.40	182.30	175.10	158.20	-	-	-	59620.00	22.11	8.31	2.40	7.31	-	-	-
Array 100 Graphitized	100G	4031.00	92.20	77.80	78.17	71.92	70.93	61.54	56.03	1493.00	5.36	4.18	1.75	9.05	4.99	2.72	2.27
Array 101	101	3086.00	271.10	229.70	190.20	183.20	-	-	-	744.20	8.69	12.00	21.35	8.14	-	-	-
Array 105	105	8635	204.8	198	179.9	154.5	-	-	-	6925	18.61	6.03	9.639	2.177	-	-	-
Array 105 Graphitized	105G	9622	-	117.7	111.3	102.3	-	-	-	7150	-	3.376	10.26	5.696	-	-	-

Appendix C Data from High Contact Pressure Carbon Fiber LFA Testing

Table C-1: MWCNT Array TIMs used in Carbon Fiber LFA Testing

MWCNT Array TIMs Tested - ALL CONTACT PRESSURES CARBON FIBER LFA TESTING								
Sample	Label	Average Thickness [µm]	Std. Dev Thickness [µm]	Mass on Slide [g]	Areal Density [g/cm2]	Bulk Density [g/cm3]	% Mass Removed	Packing Fraction
Array 78	78	54.63	4.866	1.4	0.0017	0.3114	0.00%	16.05%
Array 82	82	133.99	6.776	1.8	0.0022	0.1632	5.56%	7.95%
Array 84	84	109.23	3.551	2.3	0.0028	0.2559	0.00%	13.19%
Array 91	91	95.88	12.081	1.9	0.0023	0.2408	4.74%	11.83%
Array 92	92	110.47	6.444	1.9	0.0023	0.2090	1.58%	10.60%
Array 95	95	227.91	5.354	2.9	0.0035	0.1546	2.41%	7.78%
Array 96	96	38.20	4.741	1.0	0.0012	0.3181	18.00%	13.45%
Baseline 1	B1	0.00	0.00	0.00	0.0000	0.0000	0.00%	0.00%
Carbon Fiber	CF	-	-	-	-	-	-	-

Table C-2: Thermal Testing Results – Carbon Fiber Systems at High Contact Pressure

Carbon Fiber - Peel Ply Surface Results

Sample	Label	Diffusivity 60 cNm [mm²/s]	Diffusivity 100 cNm [mm²/s]	Diffusivity 140 cNm [mm²/s]	Contact Res 60 cNm [mm²K/W]	Contact Res 100 cNm [mm²K/W]	Contact Res 140 cNm [mm²K/W]	Diffusivity St. Dev @ 60 cNm	Diffusivity St. Dev @ 100 cNm	Diffusivity St. Dev @ 140 cNm	Contact Res St. Dev 60 cNm	Contact Res St. Dev 100 cNm	Contact Res St. Dev 140 cNm
Array 78	78	0.532	0.544	0.547	320.75	282.20	273.00	0.014	0.015	0.015	-	-	-
Array 82	82	0.652	0.641	0.647	6.40	29.75	16.75	0.004	0.004	0.009	-	-	-
Array 84	84	0.648	0.650	0.649	14.75	10.50	12.55	0.009	0.007	0.002	-	-	-
Array 91	91	0.646	0.643	0.650	19.00	25.30	10.50	0.019	0.008	0.002	-	-	-
Array 92	92	0.654	0.645	0.647	2.30	21.00	16.75	0.005	0.007	0.007	-	-	-
Array 95	95	0.630	0.617	0.624	54.40	83.33	67.17	0.012	0.005	0.007	-	-	-
Array 96	96	0.578	0.582	0.578	184.50	173.27	183.03	0.028	0.007	0.008	-	-	-
Baseline 1	B1	0.37	0.36	0.35	1965.33	1605.33	2693.67	0.020	0.010	0.043	320.740	223.191	1087.260
Carbon Fiber	CF	0.65	-	-	0.00	-	-	0.004	-	-	-	-	-

Carbon Fiber - Sanded Surface Results

Sample	Label	Diffusivity 60 cNm [mm²/s]	Diffusivity 100 cNm [mm²/s]	Diffusivity 140 cNm [mm²/s]	Contact Res 60 cNm [mm²K/W]	Contact Res 100 cNm [mm²K/W]	Contact Res 140 cNm [mm²K/W]	Diffusivity St. Dev @ 60 cNm	Diffusivity St. Dev @ 100 cNm	Diffusivity St. Dev @ 140 cNm	Contact Res St. Dev 60 cNm	Contact Res St. Dev 100 cNm	Contact Res St. Dev 140 cNm
Array 78	78	0.562	0.562	0.695	207.50	207.50	-67.50	0.004	0.003	0.008	-	-	-
Array 82	82	0.580	0.560	0.558	162.00	212.75	218.00	0.009	0.004	0.003	-	-	-
Array 84	84	0.548	0.553	0.550	245.25	231.50	239.75	0.002	0.014	0.006	-	-	-
Array 91	91	0.540	0.554	0.553	267.75	256.50	231.50	0.009	0.008	0.004	-	-	-
Array 92	92	0.549	0.548	0.546	242.50	245.25	250.75	0.003	0.006	0.003	-	-	-
Array 95	95	0.546	0.546	0.544	250.75	250.75	256.50	0.001	0.004	0.003	-	-	-
Array 96	96	0.561	0.553	0.549	210.00	231.50	242.50	0.009	0.009	0.006	-	-	-
Baseline 1	B1	0.525	0.528	0.520	0.25	0.01	1.09	0.019	0.006	0.016	0.401	0.010	1.861
Carbon Fiber	CF	0.65	-	-	0.00	-	-	0.004	-	-	-	-	-

Appendix D Data from Low Contact Pressure Carbon Fiber LFA Testing

Table D-1: Thermal Testing Results – Peel Ply Carbon Fiber Systems at Low Contact Pressure

Thermal Diffusivity, α, at Increasing Pressure - PEEL PLY INTERFACE

		Thermal Diffusivity, α, [mm^2/s]					Standard Deviation, σ, [mm^2/s]				
Sample	Label	0 in-lb	1 in-lb	2 in-lb	3 in-lb	4 in-lb	0 in-lb	1 in-lb	2 in-lb	3 in-lb	4 in-lb
Carbon Fiber	CF	0.653	-	-	-	-	-	-	-	-	-
Baseline 1	B1	0.311	0.390	0.407	0.407	0.406	0.028	0.005	0.015	0.018	0.009
Baseline 2	B2	0.247	0.365	0.368	0.394	0.397	0.006	0.003	0.011	0.010	0.015
Array 75	75	0.224	0.465	0.467	0.472	0.474	0.030	0.002	0.002	0.002	0.005
Array 78	78	0.229	0.405	0.410	0.420	0.414	0.011	0.001	0.009	0.007	0.005
Array 82	82	0.312	0.459	0.449	0.457	0.456	0.012	0.002	0.004	0.007	0.010
Array 84	84	0.284	0.463	0.463	0.458	0.461	0.019	0.002	0.003	0.009	0.004
Array 91	91	0.374	0.638	0.247	0.638	0.645	0.009	0.015	0.002	0.003	0.010
Array 92	92	0.276	0.614	0.619	0.630	0.634	0.008	0.016	0.008	0.008	0.008
Array 95	95	0.384	0.624	0.627	0.633	0.632	0.017	0.004	0.006	0.005	0.009
Array 96	96	0.435	0.512	0.499	0.511	0.514	0.011	0.013	0.016	0.026	0.010

Thermal Contact Resistance, R_c, at Increasing Pressure

		Thermal Contact Resistance, R_c, [mm^2K/W]				
Sample	Label	0 in-lb	1 in-lb	2 in-lb	3 in-lb	4 in-lb
Carbon Fiber	CF	0.653	-	-	-	-
Baseline 1	B1	1595.00	969.00	866.50	866.50	872.50
Baseline 2	B2	2436.00	1156.00	1134.50	959.50	941.00
Array 75	75	2797.00	575.00	566.00	544.80	536.40
Array 78	78	2703.50	878.00	849.50	794.00	827.00
Array 82	82	1585.00	601.50	647.50	610.50	615.00
Array 84	84	1889.00	583.80	583.80	606.00	592.50
Array 91	91	1074.00	36.25	2397.00	36.25	21.00
Array 92	92	1987.50	91.00	79.25	54.00	45.00
Array 95	95	1007.50	67.50	60.70	47.20	49.50
Array 96	96	715.50	389.00	436.75	392.75	382.00

Table D-2: Thermal Testing Results – Sanded Carbon Fiber Systems at Low Contact Pressure

Thermal Diffusivity, α, at Increasing Pressure - SANDED INTERFACE											
		Thermal Diffusivity, α, [mm^2/s]					Standard Deviation, σ, [mm^2/s]				
Sample	Label	0 in-lb	1 in-lb	2 in-lb	3 in-lb	4 in-lb	0 in-lb	1 in-lb	2 in-lb	3 in-lb	4 in-lb
Carbon Fiber	CF	0.6533	-	-	-	-	-	-	-	-	-
Base	B1	0.402	0.490	0.501	0.511	0.510	0.026	0.014	0.010	0.016	0.005
Base	B2	0.543	0.444	0.437	0.421	0.422	0.009	0.006	0.011	0.005	0.008
AIA	75	0.356	0.527	0.534	0.539	0.533	0.005	0.001	0.002	0.000	0.003
AIA	78	0.374	0.554	0.552	0.563	0.568	0.003	0.005	0.008	0.008	0.003
AIA	82	0.407	0.568	0.572	0.572	0.568	0.014	0.012	0.003	0.007	0.007
AIA	84	0.421	0.541	0.541	0.543	0.544	0.023	0.009	0.013	0.016	0.008
AIA	91	0.422	0.559	0.557	0.564	0.565	0.011	0.003	0.009	0.001	0.003
AIA	92	0.403	0.564	0.562	0.564	0.565	0.014	0.006	0.002	0.005	0.003
AIA	95	0.383	0.545	0.549	0.542	0.553	0.004	0.040	0.007	0.002	0.008
AIA	96	0.382	0.534	0.549	0.553	0.550	0.009	0.012	0.005	0.002	0.008

Thermal Contact Resistance, R_c, at Increasing Pressure						
		Thermal Contact Resistance, R_c, [mm^2K/W]				
Sample		0 in-lb	1 in-lb	2 in-lb	3 in-lb	4 in-lb
Baseline 1	B1	651.50	343.70	313.00	286.50	289.25
Baseline 2	B2	246.20	577.00	606.30	677.10	672.50
Array 75	75	1080.50	304.00	283.50	269.00	286.40
Array 78	78	964.25	227.50	232.75	203.70	190.75
Array 82	82	778.50	190.75	180.75	180.75	190.75
Array 84	84	708.50	263.20	263.20	257.75	254.90
Array 91	91	703.50	214.00	219.50	201.00	198.50
Array 92	92	799.10	201.00	206.25	201.00	198.50
Array 95	95	910.50	252.00	241.00	260.50	230.00
Array 96	96	916.00	283.50	241.00	230.00	238.25

REFERENCES

1. Akinaga, H., T. Asai, and et al., *Emerging Research Devices*, in *International Technology Roadmap for Semiconductors*. 2009.
2. Evans, L.E. *General Physics I - Thermal Physics 1*. [Online PDF] 2012 [cited 2012 3/12/2012]; Notes from Physics 053L online at Duke University]. Available from: http://www.phy.duke.edu/~lee/P53/therm1.pdf.
3. Sarvar, F.W., D.; Conway, P., *Thermal Interface Materials - A Review of the State of the Art*, in *2006 Electronics Systemintegration Technology Conference*. 2006: Dresden, Germany. p. 1292 - 1302.
4. deSorgo, M. *Thermal Interface Materials*. 1996 [cited 2012; Available from: http://www.electronics-cooling.com/1996/09/thermal-interface-materials-2/.
5. Prasher, R., *Thermal Interface Materials: Historical Perspective, Status, and Future Directions.* Proceedings of the IEEE, 2006. **94**(8): p. 1571-1586.
6. Shaikh, S., et al., *Thermal conductivity of an aligned carbon nanotube array.* Carbon, 2007. **45**(13): p. 2608-2613.
7. Cola, B.A., J. Xu, and T.S. Fisher, *Contact mechanics and thermal conductance of carbon nanotube array interfaces.* International Journal of Heat and Mass Transfer, 2009. **52**(15-16): p. 3490-3503.
8. Iijima, S., *Helical microtubules of graphitic carbon.* Nature, 1991. **354**(7): p. 56-58.
9. Iijima, S. and T. Ichihashi, *Single-shell carbon nanotubes of 1-nm diamter.* Nature, 1993. **363**: p. 603-605.
10. Bethune, D.S., et al., *Cobalt-catalysed growth of carbon nanotubes with single-atomic-layer walls.* Nature, 1993. **363**: p. 605 - 607.
11. Endo, M., et al., *Applications of carbon nanotubes in the twenty-first century.* Philosophical Transactions of the Royal Society of London A, 2004: p. 2223 - 2238.
12. Ruoff, R., D. Qian, and W.K. Liu, *Mechanical Properties of carbon nanotubes: theoretical predictions and experimental measurements.* C.R. Physique, 2003. **4**: p. 993-1008.
13. Berber, S., Y.-K. Kwon, and D. Tomanek, *Unusually High Thermal Conductivity of Carbon Nanotubes.* Physical Review Letters, 2000. **84**(20): p. 4613 - 4616.
14. Hone, J., et al., *Electrical and thermal transport properties of magnetically aligned single wall carbon nanotube films.* Applied Physics Letters, 2000. **77**(5): p. 666 - 668.
15. Thostenson, E.T. and T. Chou, *On the elastic properties of carbon nanotube-based composites: modelling and characterization.* Journal of Physics D: Applied Physics, 2003. **36**: p. 573-582.
16. Bagchi, A., *On the Effective Thermal Conductivity of Carbon Nanotube Reinforced Polymer Composites*, in *College of Engineering*. 2005, University of Texas at Arlington: Arlington, TX. p. 87.
17. Terrones, H. and M. Terrones, *Curved nanostructured materials.* New Journal of Physics, 2003. **5**: p. 126.1 - 126.37.
18. Stone, A.J. and D.J. Wales, *Theoretical studies of icosahedral C_{60} and some related structures.* Chemical Physics Letters, 1986. **128**: p. 510-503.
19. Wei, C., K. Cho, and D. Srivastava, *Tensile yielding of multiwall carbon nanotubes.* Applied Physics Letters, 2003. **82**(15): p. 2512-2514.
20. Srivastava, D., C. Wei, and K. Cho, *Nanomechanics of carbon nanotubes and composites.* Applied Mechanics Review, 2003. **56**(2): p. 215 - 230.

21. Nardelli, M.B., B.I. Yakobson, and J. Bernholc, *Mechanism of strain release in carbon nanotubes.* Physical Review B, 1998. **57**(8): p. R4277 - R4280.
22. Wei, C., K. Cho, and D. Srivastava, *Tensile strength of carbon nanotubes under realistic temperature and strain rate.* Physical Review B, 2003. **67**(115407): p. 115407-1 - 115407-5.
23. Collins, P.G., et al., *Current Saturation and Electrical Breakdown in Multiwalled Carbon Nanotubes.* Physical Review Letters, 2001. **86**(14): p. 3128-3131.
24. Suhr, J., et al., *Fatigue resistance of aligned carbon nanotube arrays under cyclic compression.* Nature Nanotechnology, 2007: p. 1-5.
25. Chang, C.W., et al., *Nanotube Phonon Waveguide.* Physical Review Letters, 2007. **99**(045901): p. 4.
26. Natleson, D., *What is a phonon?*, in *nanoscale views*. 2009. p. A layman's description of phonons.
27. Cahill, D.G., et al., *Nanoscale thermal transport.* Journal of Applied Physics, 2003. **93**(2): p. 793 - 818.
28. Incropera, F.P., et al., *Introduction to Heat Transfer*. 5th ed. 2007: John Wiley & Sons.
29. Kim, P., et al., *Mesoscopic thermal transport and energy dissipation in carbon nanotubes.* Physica B, 2002. **323**(1): p. 67 - 70.
30. Ivanov, I., et al., *Fast and highly anisotropic thermal transport through vertically aligned carbon nanotube arrays.* Applied Physics Letters, 2006. **89**(223110): p. 1-3.
31. Yi, W., et al., *Linear specific heat of carbon nanotubes.* Physical Review B, 1999. **59**(14): p. 9015 - 9018.
32. Sihn, S., et al., *Enhancement of through-thickness thermal conductivity in adhesively bonded joints using aligned carbon nanotubes.* Composites Science and Technology, 2008. **68**: p. 658-665.
33. Ganguli, S., et al., *Metalized Nanotube Tips Improve Through Thickness Thermal Conductivity in Adhesive Joints.* Journal of Nanoscience and Nanotechnology, 2009. **9**(3): p. 1727-1733.
34. Treacy, M.M.J., T.W. Ebbesen, and J.M. Gibson, *Exceptionally high Young's modulus observed for individual carbon nanotubes.* Nature, 1996. **381**: p. 678 - 680.
35. Wong, E.W., P.E. Sheehan, and C.M. Lieber, *Nanobeam Mechanics: Elasticity, Strength, and Toughness of Nanorods and Nanotubes.* Science, 1997. **277**: p. 1971 - 1974.
36. Lourie, O. and H.D. Wagner, *Evaluation of Young's modulus of carbon nanotubes by micro-Raman spectroscopy.* Journal of Materials Research, 1998. **13**(9): p. 2418 - 2422.
37. Yu, M.F., et al., *Strength and Breaking Mechanism of Multiwalled Carbon Nanotubes Under Tensile Load.* Science, 2000. **287**: p. 637 - 640.
38. Pan, Z.W., et al., *Tensile tests of ropes of very long aligned multiwall carbon nanotubes.* Applied Physics Letters, 1999. **74**(21): p. 3152 - 3154
39. Marques, M.A.L., et al., *On the Breaking of Carbon Nanotubes under Tension.* Nano Letters, 2004. **4**(5): p. 811 - 815.
40. Andrews, R. and M.C. Weisenberger, *Carbon nanotube polymer composites.* Current Opinion in Solid State & Materials Science, 2003. **8**: p. 31-37.
41. Ruoff, R.S., et al., *Radial deformation of carbon nanotubes by van der Waals forces.* Nature, 1993. **364**.
42. Garcia, E., B. Wardle, and J.A. Hart, *Joining prepreg composite interfaces with aligned carbon nanotubes.* Composites Part A: Applied Science and Manufacturing, 2008. **39**(6): p. 1065 -1070.
43. Ajayan, P.M. and J.M. Tour, *Nanotube Composites.* Nature, 2007. **447**: p. 1066 - 1068.

44. Veedu, V.P., et al., *Multifunctional composites using reinforced laminae with carbon-nanotube forests.* Nature Materials, 2006. **5**: p. 457 - 462.
45. Schmidt, W.J., *Studien am integument der reptilien IV. Uroplatus fimbriatus (Schneid) und die geckoniden.* Zoologische Jahrbucher, 1913. **36**: p. 377 - 464.
46. Autumn, K., et al., *Adhesive force of a single gecko foot-hair.* Nature, 2000. **405**: p. 681 - 685.
47. Qu, L., et al., *Carbon Nanotube Arrays with Strong Shear Binding-On and Easy Normal Lifting-off.* Science, 2008. **322**: p. 238 - 242.
48. Zhao, Y., et al., *Interfacial energy and strength of multiwalled-carbon-nanotube-based dry adhesive.* Journal of Vacuum Science and Technology B, 2006. **24**(1): p. 331 - 335
49. Sitti, M. and R.S. Fearing, *Synthetic gecko foot-hair micro/nano-structures as dry adhesives.* Journal of Adhesion Science and Technology, 2003. **17**(8): p. 1055 - 1073.
50. Parker, W.J., et al., *Flash Method of Determining Thermal Diffusivity, Heat Capacity, and Thermal Conductivity.* Journal of Applied Physics, 1963. **32**(9): p. 1679 - 1684.
51. Cape, J.A. and G.W. Lehman, *Temperature and Finite Pulse-Time Effects in the Flash Method for Measuring Thermal Diffusivity.* Journal of Applied Physics, 1963. **34**(7): p. 1909 - 1913.
52. Cowan, R.D., *Pulse Method of Measuring Thermal Diffusivity at High Temperatures.* Journal of Applied Physics, 1962. **34**(4): p. 926 - 927.
53. Josell, D., J. Warren, and A. Cezairliyan, *Comment on "Analysis for determining thermal diffusivity from thermal pulse experiments".* Journal of Applied Physics, 1995. **78**(11): p. 6867 - 6869.
54. Taylor, R.E., J. Jortner, and H. Groot, *Thermal Diffusivity of Fiber-Reinforced Composites using the Laser Flash Technique.* Carbon, 1984. **23**(2): p. 215-222.
55. Campbell, R.C., *Approximations in the Use of Two and Three Layer Analysis Models in Flash Diffusivity Measurements*, in *International Thermal Conductivity Conference*. 1998. p. 13.
56. Sweet, J.N., *Data Analysis Methods for Flash Thermal Diffusivity Experiments*, P.T. Division, Editor. 1989, Sandia National Laboratories: Albuquerque, NM. p. 1 - 86.
57. Lee, R.T., *Thermal Diffusivity of Dispersed and Layered Composites*, in *Graduate School*. 1977, Purdue University: West, Lafayette, IN. p. 142.
58. Jacques, D. and R. Andrews, *Process For The Continuous Production of Aligned Carbon Nanotubes*, U.S.P. Office, Editor. 2007: United States of America. p. 11.
59. Andrews, R., et al., *Continuous production of aligned carbon nanotubes: a step closer to commercial realization.* Chemical Physics Letters, 1999. **303**: p. 467 - 474.
60. Sciencelab.com, I. *MSDS - Xylene*. [PDF] 2010 11/01/2010 [cited 2012 1/26/2012]; MSDS for Xylene].
61. Netzsch, *NETZSCH-LFA WINDOWS software: Help system*. 2012, Netzsch Instruments: Instrument documentation.
62. Andrews, R., et al., *Purification and structural annealing of multiwalled carbon nanotubes at graphitization temperatures.* Carbon, 2001. **39**: p. 1681-1687.
63. Intel Corporation, *2nd Generation Intel Core Processor Family Desktop and Intel Pentium Processor Family Desktop, and LGA1155 Socket Thermal Mechanical Specifications and Design Guidelines (TMSDG)*. 2011. p. 38, 87.
64. ASM International, *ASM Handbookm Volume 21: Composites*. ASM Handbook, ed. S.L. Donaldson and D.B. Miracle. Vol. 21. 2001: ASM International.
65. Bullen, A.J., et al., *Thermal Conductivity of amorphous carbon thin films.* Journal of Applied Physics, 2000. **88**(11): p. 3.

66. Hinds, B., et al., *Aligned Multiwalled Carbon Nanotubes Membranes.* Science, 2004. **303**(62): p. 62 - 67.
67. Felten, A., et al., *Radio-frequency plasma functionalization of carbon nanotubes surface O_2, NH_3, and CF_4 treatments.* Journal of Applied Physics, 2005. **98**(074308): p. 1-9.
68. Takegoshi, E., et al., *Measurement of Thermal Properties of Iron Oxide Pellets.* International Journal of Thermophysics, 1984. **5**(2): p. 10.
69. Hamwi, A., et al., *Fluorination of Carbon Nanotubes.* Carbon, 1997. **35**(6): p. 723 - 728.
70. Weisenberger, M.C., et al., *The effect of graphitization temperature on the structure of helical-ribbon carbon nanofibers.* Carbon, 2009. **47**: p. 2211 - 2218.
71. Zalameda, J.N., *Measured Through-the-Thickness Thermal Diffusivity of Carbon Fiber Reinforced Composite Materials.* Journal of Composites Technology and Research, 1999. **21**(2).

VITA

Darrell Keith Etheredge

Born June 18, 1987, Louisville, Kentucky

Education

Bachelor of Science, Mechanical Engineering, University of Kentucky, Lexington, Kentucky, USA, August 2005-May 2010.

Graduate studies, University of Kentucky, Center for Applied Energy Research, Lexington, Kentucky, USA, May 2010-May 2012. Advisor: Dr. Rodney Andrews.

Professional positions

2012	Mechanical Engineer, Cummins, Inc., Columbus, Indiana
2009-2010	Graduate Research Assistant, Center for Applied Energy Research, University of Kentucky, Lexington, Kentucky
2008-2010	Academic Year Part Time student employee, Lexmark International, Lexington, KY
2006-2008	Mechanical Engineering Co-op, General Electric Appliance Park, Louisville, Kentucky

Awards and scholarships

2010-2012	University of Kentucky, Center for Applied Energy Research, Research Assistantship
2009	Lexmark Student Symposium Scholarship
2005-2010	University of Kentucky, Provost Scholarship

Conference proceedings

Keith Etheredge, Matthew C. Weisenberger, John D. Craddock, Carissa D. Russell, A. T. Owens, Rich Foedinger, *Effect of MWCNT Properties on their use as TIMs in Aluminum and Carbon Fiber Systems.* American Carbon Society Symposium; 2012; Atlanta, Georgia, USA; 2012

Keith Etheredge, Matthew C. Weisenberger, Carissa D. Russell, John D. Craddock, A. T. Owens, Rich Foedinger, *LFA Characterization of Re-workable Multiwall Carbon Nanotube Array Thermal Interface Materials.* Society for the Advancement of Materials and Process Engineering; 2011; Long Beach, California, USA; 2011